The Arctic Coastal Erosion Model: Overview, Developments, and Calibration at Drew Point, Alaska

Elyce Bayat[1], Diana L Bull[1], Jennifer M Frederick[1], Alejandro Mota[2], Benjamin M. Jones[3], Irina Kalashnikova Tezaur[1], Christopher Flanary[4], Emily Mae Bristol[5], Melissa Ward Jones[3], Robert Charles Choens[1], and Craig Jones[6]

[1]Sandia National Laboratories
[2]Sandia National Laboratories California
[3]University of Alaska Fairbanks
[4]Integral Consulting Inc
[5]The University of Texas at Austin, Marine Science Institute
[6]Integral Consulting Inc.

March 01, 2025

Abstract

Permafrost coastlines are experiencing significant erosion as polar amplification has enhanced the effects of climate change in the Arctic. Warmer temperatures are increasing thermo-denudation and more energetic oceans are increasing thermo-abrasion in unlithified, ice-bonded permafrost coastlines. However, models capable of simultaneously capturing these erosional processes whilst being sensitive to terrestrial variability and responsive to transient environmental drivers did not previously exist. Here we present the Arctic Coastal Erosion (ACE) model developed to couple evolving oceanographic and atmospheric conditions at storm-resolving time steps with a finite element multi-physics terrestrial permafrost model. This permafrost model unites thermal and mechanical governing equations by allowing 3D heat conduction with solid-liquid phase change to drive the ice saturation, which governs how the 3D mechanical stress-strain fields develop. The ACE terrestrial model removes failed elements to simulate both slowly advancing thermo-denudation with permafrost sloughing from the face, and highly episodic thermo-abrasion, with niche formation and rapidly advancing block failure. A 2018 summer field campaign at Drew Point, Alaska with sub-daily observations of thermo-denudation and thermo-abrasion, including knowledge of niche geometry before block failure, enable calibration of the terrestrial model. Detailed compositional and geomechanical characterization of the ice-bonded sediments underlay advances in the material model representation and calibrated erosion criteria. We demonstrate a daily RMSE of 0.16 m for thermo-denudation over the summer and achieve block failure within 2.5 days of the observed. The calibrated ACE model can be used to inform: adaptive actions at the community scale and, through parameterization, inform circum-Arctic geochemical flux volumes.

The Arctic Coastal Erosion Model: Overview, Developments, and Calibration at Drew Point, Alaska

Elyce Bayat[1], Diana L. Bull[1], Jennifer M. Frederick[1], Alejandro Mota[2], Benjamin M. Jones[3], Irina Tezaur[2], Christopher Flanary[5], Emily M. Bristol[4], Melissa Ward Jones[3], Robert C. Choens[1], , Craig A. Jones[5]

[1]Sandia National Laboratories, Albuquerque, NM, USA
[2]Sandia National Laboratories, Livermore, CA, USA
[3]University of Alaska, Fairbanks, AK, USA
[4]University of Texas at Austin, Port Aransas, TX, USA
[5]Integral Consulting Inc., Santa Cruz, CA, USA

Key Points:

- The ACE model simulates thermo-mechanical permafrost erosion in a finite-element form responsive to dynamic atmospheric and oceanic drivers.
- 2018 field observations of slow slough and rapid block failure enable unequaled calibration of erosion progression, degree, and mechanisms.
- Calibration of this novel multi-physics approach enables future predictions sensitive to terrestrial and environmental variability.

Corresponding author: =name=, `=email address=`

Abstract

Permafrost coastlines are experiencing significant erosion as polar amplification has enhanced the effects of climate change in the Arctic. Warmer temperatures are increasing thermo-denudation and more energetic oceans are increasing thermo-abrasion in unlithified, ice-bonded permafrost coastlines. However, models capable of simultaneously capturing these erosional processes whilst being sensitive to terrestrial variability and responsive to transient environmental drivers did not previously exist. Here we present the Arctic Coastal Erosion (ACE) model developed to couple evolving oceanographic and atmospheric conditions at storm-resolving time steps with a finite element multi-physics terrestrial permafrost model. This permafrost model unites thermal and mechanical governing equations by allowing 3D heat conduction with solid-liquid phase change to drive the ice saturation, which governs how the 3D mechanical stress-strain fields develop. The ACE terrestrial model removes failed elements to simulate both slowly advancing thermo-denudation with permafrost sloughing from the face, and highly episodic thermo-abrasion, with niche formation and rapidly advancing block failure. A 2018 summer field campaign at Drew Point, Alaska with sub-daily observations of thermo-denudation and thermo-abrasion, including knowledge of niche geometry before block failure, enable calibration of the terrestrial model. Detailed compositional and geomechanical characterization of the ice-bonded sediments underlay advances in the material model representation and calibrated erosion criteria. We demonstrate a daily RMSE of 0.16 m for thermo-denudation over the summer and achieve block failure within 2.5 days of the observed. The calibrated ACE model can be used to inform: adaptive actions at the community scale and, through parameterization, inform circum-Arctic geochemical flux volumes.

Plain Language Summary

Enhanced Arctic warming is causing permafrost coastlines to recede at increasing rates. The ice in sediment-rich permafrost bonds the material together. Erosion is achieved by increased temperatures thawing the permafrost and by the ocean producing a niche with resultant overhanging frozen permafrost that eventual fails, in block failure, due to gravitational forces. The Arctic Coastal Erosion (ACE) model accounts for atmospheric, oceanographic, and permafrost dynamics to predict these erosional processes. It is the only model, to date, in which sub-daily environmental conditions produce differential erosional amounts according to the two mechanisms in a way that is sensitive to permafrost composition and coastline geometry. Model calibration from a summer-long 2018 field campaign at Drew Point, Alaska demonstrates accurate daily simulation of the thawing and slow-sloughing of permafrost off of the face of the coastline. It also captures rapidly advancing block failure, within 2.5 days of the observed, due to an observationally accurate niche-depth inducing failure forces near the back of the simulated coastline. The newly calibrated ACE model could be used to inform adaptations for coastal communities in the Arctic as well as inform impact analyses from large-scale fluxes of geochemical permafrost materials.

1 Introduction

Arctic coastlines are unique in that they are composed of permafrost, ground with below freezing temperatures for two or more years. Although these coastlines have always been subject to erosion, historically it has been minimal due to the stabilizing presence of land and sea ice, which created calm nearshore ocean environments, and cooler atmospheric temperatures that limited the interaction between the ocean and the base of coastal bluffs. Thus, even though Arctic coastlines constitute over one third of global coastlines (Lantuit et al., 2012), erosion models have typically been developed for lower latitudes, as they historically possessed larger erosion rates (Mentaschi et al., 2018). These lower-latitude models are not well-suited for Arctic permafrost undergoing erosion as it

is the melting of ground-ice and thawing of permafrost that results in an erodible unconsolidated material, which must be captured by combined thermal-chemical-mechanical processes.

Climate change has disproportionately influenced the Arctic (Rantanen et al., 2022): sea ice has declined and increased the duration of the open water season (Thomson & Rogers, 2014; Barnhart, Overeem, & Anderson, 2014) resulting in more energetic wave environments (Thomson & Rogers, 2014; Wang & Overland, 2015; Liu et al., 2016; Casas-Prat & Wang, 2020; Nederhoff et al., 2022) in concert with warming air (Rantanen et al., 2022), ocean (Moon et al., 2023), and permafrost (Smith et al., 2022) temperatures. With these changes, rates of erosion have been increasing across circum-Arctic permafrost coastlines throughout the 21st century (B. M. Jones et al., 2018; Irrgang et al., 2022). The variability in both the magnitude and the trend in rates of erosion is quite astounding; some sections of the Alaska Beaufort Sea coast have retreated more than 34 m in a single year, making them some of the fastest eroding coasts in the world, whilst others experience only meters of erosion (A. Gibbs et al., 2015; B. M. Jones et al., 2009, 2018; Ward Jones et al., To be Submitted). Variability in constituent properties of the terrestrial material (e.g., sediment and pore ice composition in ice-bonded sediments, ice wedge morphology of the permafrost, and seasonally frozen peat layer characteristics) as well as coastal orientation, near-shore oceanographic conditions responding to local bathymetry, and the presence of barrier islands all contribute to high variability in erosion rates (Jorgenson & Brown, 2005; Kanevskiy et al., 2013). As shown in Figure 1(a), the permafrost stratigraphy at a single location can be quite complex and the ability to account for variations in terrestrial material in addition to variable atmospheric and near-shore oceanographic conditions are all needed to capture circum-Arctic erosional variability.

Thermo-denudation and thermo-abrasion processes dominate Arctic coastal erosion (Aré, 1988a, 1988b; Walker, 1988; Günther et al., 2013; Irrgang et al., 2022). In thermo-denudation, permafrost warms in response to atmospheric drivers resulting in the melting of ice and the resulting loss of structural cohesion in the permafrost, causing a sinking movement, i.e. subsidence or slumping, under gravitational forces. Along a coastline, this denuded material can separate, or slough, from surrounding material by dripping or oozing as a material slurry into the nearshore environment as shown in Figure 1(c). With a thermo-abrasive process, ocean water warms the permafrost into a similar material slurry and then removes the unconsolidated material, resulting in a recess or niche like the one shown in Figure 1(b). The resulting over-hanging bluff creates tensile stress behind the niche in frozen permafrost which eventually causes failure of a large block of material (e.g., a "block failure" event) shown in Figure 1(d). The role of undercutting and the presence of ice wedges are cited as factors affecting block failure (Walker, 1988; Hoque & Pollard, 2009; Thomas et al., 2020).

Research has attempted to correlate erosion rates with environmental drivers like temperature, open water days, wind speeds, and even wave power (Overeem et al., 2011; Lantuit et al., 2011; Günther et al., 2015; B. M. Jones et al., 2018; A. E. Gibbs et al., 2021; Ward Jones et al., To be Submitted). Most of these studies found a lack of significant correlation for mean erosion as analysis often spans decadal scales without sufficient sub-decadal observations (Overeem et al., 2011; Lantuit et al., 2011; Günther et al., 2015). Studies with annual, or higher, frequency observations (B. M. Jones et al., 2018), have also struggled to find correlation with environmental drivers. However, recent work to explore new measures of storm intensity through wave energy (A. E. Gibbs et al., 2021) or integrated wind speeds (Ward Jones et al., To be Submitted) have found better correlations. In particular, (A. E. Gibbs et al., 2021) found normalized anomalies of cumulative wave energy to correlate significantly with erosion at Barter Island. These two significant correlations reinforce the need for model development in which the environmental drivers are of a fidelity sufficiently resolved to drive mechanistic failure.

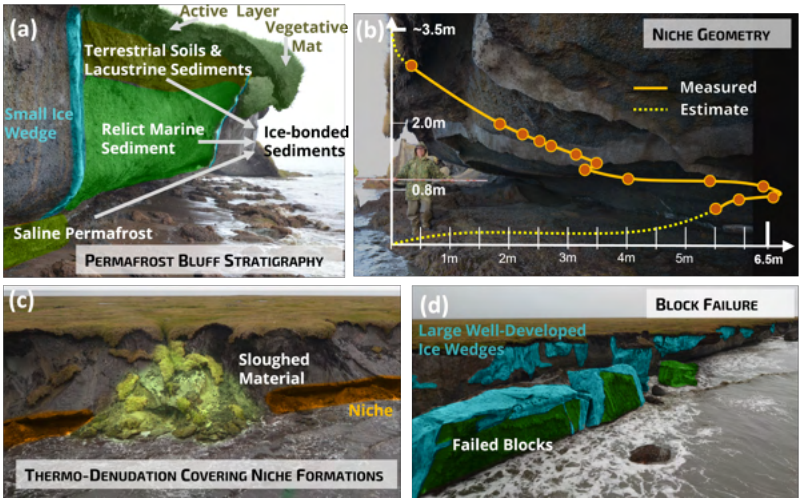

Figure 1. Field photographs documenting aspects of the permafrost bluff and erosion mechanisms at Drew Point, AK. Photos from the coast show: aspects of the permafrost bluff stratigraphy in panel (a), a well-developed niche geometry with measured dimensions overlaid in panel (b), and the lower two photos document thermo-denudation (panel (c)) and block failure (panel (d)).

However, a literature review reveals that no existing state-of-the-art Arctic coastal erosion model is able to quantify permafrost erosion from both thermo-denudation and thermo-abrasion simultaneously, capture episodic storm-driven events, and account for the variability in the terrestrial environment. These models generally have at least one of the following limitations: (1) they do not account for dynamic atmospheric and oceanic drivers and/or only include simplified dynamic boundary conditions (Barnhart, Anderson, et al., 2014; Ravens et al., 2012; Wobus et al., 2011; Nielsen et al., 2022); (2) they employ empirical formulations often developed from limited observations (Barnhart, Anderson, et al., 2014; Hoque & Pollard, 2009; Aré, 1988a; Wobus et al., 2011); (3) they assume a particular type of erosion (Hoque & Pollard, 2009, 2016; Ravens et al., 2012; Guégan & Christiansen, 2017); (4) they are thermal models calibrated for niche formation which neglect the development of mechanical strains and stresses (Kobayashi, 1985; Kobayashi et al., 1999; Wobus et al., 2011; Ravens et al., 2012); and/or (5) they do not account for compositional or morpholoigcal variations of the permafrost (Barnhart, Anderson, et al., 2014; Ravens et al., 2012; Nielsen et al., 2022; Kobayashi, 1985; Kobayashi et al., 1999; Wobus et al., 2011). In (Islam & Lubbad, 2022), the authors worked to overcome many of the limitations above by treating dynamic boundary conditions and including multiple erosion types in a modeling framework that couples morphological change into the oceanic component. However, they still fundamentally rely on analytic simplifications of niche formation, block collapse, and denudation without directly addressing the governing differential equations.

This work presents calibration of the Arctic Coastal Erosion (ACE) model, a first-of-its-kind multi-physics numerical tool developed under a large-scale, multi-institutional effort and described in the earlier works (Frederick et al., 2021; D. L. Bull et al., 2020; Thomas et al., 2020). As shown in Figure 2, the ACE model couples dynamic oceanographic and atmospheric conditions with a terrestrial permafrost domain to capture the thermal-chemical-mechanical dynamics of erosion along permafrost coastlines. This effort has allowed the opportunity for additional, extensive experimental work that has underpinned the ACE model development, including specifically-designed field campaigns

to measure *in situ* ocean and erosion processes, mechanical material properties derived from thermally driven geomechanical experiments, as well as extensive physical composition and geochemical analyses (D. L. Bull et al., 2020; Bristol et al., 2021).

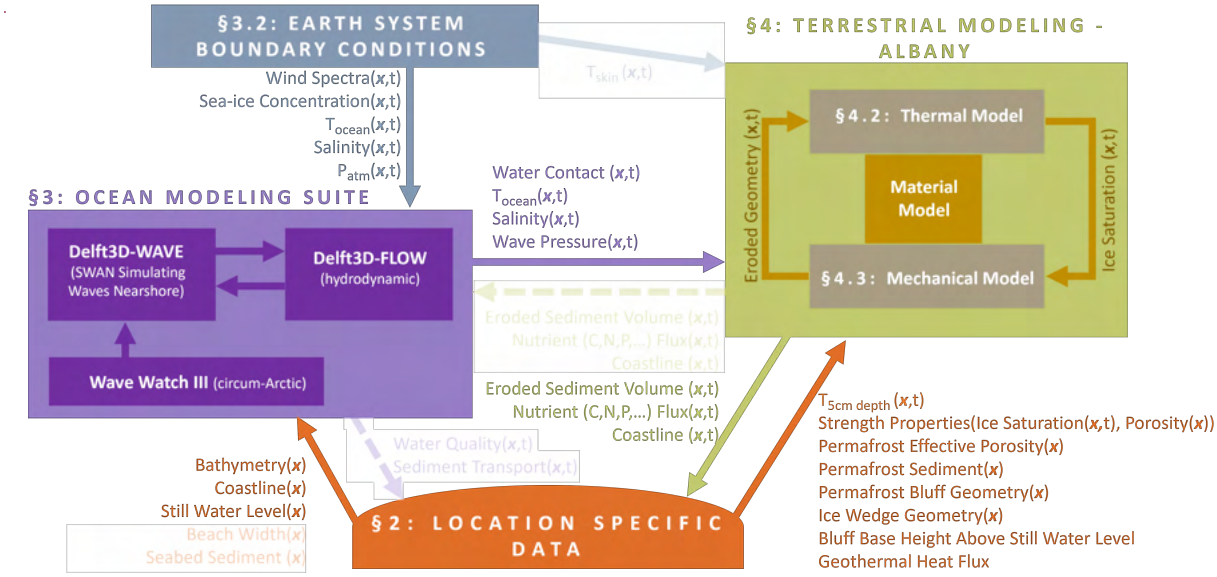

Figure 2. Schematic outlining the inputs and outputs to each component of the Arctic Coastal Erosion (ACE) Model as implemented in this calibration study. The section is identified in which each component is described. Dashed and ghosted connections are not yet implemented in the model whilst ghosted yet solid connections indicate alternate input options. Inputs and outputs that are location and time dependent are identified by $(\boldsymbol{x}, t)$.

The ACE model houses a finite element, terrestrial permafrost model (Frederick et al., 2021) representing the coastline combined with dynamically evolving oceanographic and atmospheric boundary conditions. An oceanographic modeling suite (consisting of WAVEWATCH III ((WW3DG), 2019), Delft3D-FLOW (Deltares, 2018a), and Delft3D-WAVE (Deltares, 2018b)) produces time-dependent water level based temperature and pressure boundary conditions, while atmospheric data can be provided from an Earth System Model, reanalysis, or local measurements. In the terrestrial model a coupling framework unites the mechanical and thermal aspects of erosion across a range of geomorphologies and geophysics. Three-dimensional (3-D) stress/strain fields develop in response to a plasticity model of the permafrost that is controlled by the frozen water content determined by modeling 3-D heat conduction and solid-liquid phase change. This modeling approach enables failure from any allowable deformation (niche development, block failure, and denudation) and thus can be configured to be applied at any coastline. Although possible, the ACE model does not currently two-way couple the terrestrial morphological changes into the oceanographic estimates (as represented by dashed lines in Figure 2). Further details of the model are offered in the following sections.

The main objectives of this paper are to discuss the results from a rigorous calibration of the ACE model using observational data collected at Drew Point, Alaska, and to present several key improvements to the terrestrial component of ACE. We have chosen Drew Point as our model calibration site because of the wealth of available data at this location. The calibration study focuses on the erosional evolution of a single permafrost polygon that is a part of a larger 1.5 km stretch monitored with high spatiotemporal res-

olution over the 2018 and 2019 open water seasons (D. L. Bull et al., 2020; Ward Jones et al., To be Submitted). This data set consists of daily thermo-denudation and hourly niche development measurements while also capturing a block failure event in response to the observed niche geometry. Our goal herein is to pair this carefully-designed field study with our multi-physics (i.e., oceanographic, atmospheric, thermal, and mechanical) model development, to yield a predictive permafrost erosion model that can capture complex interactions between components at high fidelity. This is one of the first demonstrations of erosion calibration at such high temporal fidelity (the other is a week long study in (Barnhart, Anderson, et al., 2014)) to achieve accurate open-water season erosion in one permafrost polygon.

Toward this effect, the remainder of this paper is organized as follows. Section 2 provides some background on the Drew Point, Alaska site targeted in the present study, and overviews the location specific data used as inputs for and drivers of other components in the model (see connecting arrows with orange text in Figure 2). In Section 3, we describe the oceanographic modeling suite and the boundary conditions used to simulate the nearshore conditions which produce hindcasts of water contact, temperature, salinity and wave pressure boundary conditions for the terrestrial model (see purple text in Figure 2). Section 4 details the terrestrial model with Section 4.1 first outlining the simulation domain. In Sections 4.2 and 4.3, we detail the thermal and mechanical components of the terrestrial model while Section 4.4 overviews the thermo-mechanical coupling that occurs between the components. We highlight in these sections several recent improvements to the ACE terrestrial model relative to (Frederick et al., 2021), which include: changes to the erosion criteria used within the model, the addition of time-varying wave pressure boundary condition, and improvements to the material model representations. Details of the components' implementation are introduced generally followed by the specific Drew Point application. We outline the calibration observations and provide results of our Drew Point calibration study in Section 5. This is followed by a discussion of these results with conclusions regarding the contributions in Section 6.

Combined, this work offers the most mechanistically grounded treatment of Arctic coastal erosion available in the literature at this time. As such, the ACE model can be used to simulate erosion for a variety of applications. For example, erosion is threatening 29 native coastal villages in Alaska, at huge economic and cultural expense (University of Alaska Fairbanks Institute of Northern Engineering & Laboratory, 2019), and this model is uniquely positioned to enable communities to plan adaptive actions, like seawalls, or to assess relocation. At the same time, parameterizing regional results and scaling them to large coastline extents expands applicability to Earth System Models and facilitates estimates of geochemical and sediment land-to-ocean fluxes at circum-Arctic scales. The ACE model and experimental results can thus be used to inform scientific understanding of thermo-mechanical coastal erosion while also providing sound simulations to address an array of purposes.

2 Calibration Study Area and Observations

The ACE model is calibrated using observational data from Drew Point, Alaska. Drew Point is located along the western Alaskan Beaufort Sea coast approximately 100 km east of Utqiagvik (formerly known as Barrow) and 200 km west of Prudhoe Bay. The 9 km stretch of coastline at Drew Point has among the highest coastal erosion rates across the circum-Arctic, and erosion rates appear to be increasing non-linearly since the mid-20th century (B. M. Jones et al., 2018). Modern (2002-2019) annual rates average 18.7 m yr^{-1} (Figure 3), and can reach 34.5 m yr^{-1} (Ward Jones et al., To be Submitted). This dramatic coastal retreat occurs over the ∼90 day open water season (Overeem et al., 2011). The dominant erosional process at Drew Point is thermo-abrasion that leads to block failure, which is common for ice-rich, unlithified permafrost bluffs (B. Jones et al., 2009; Irrgang et al., 2022) (Figure 1).

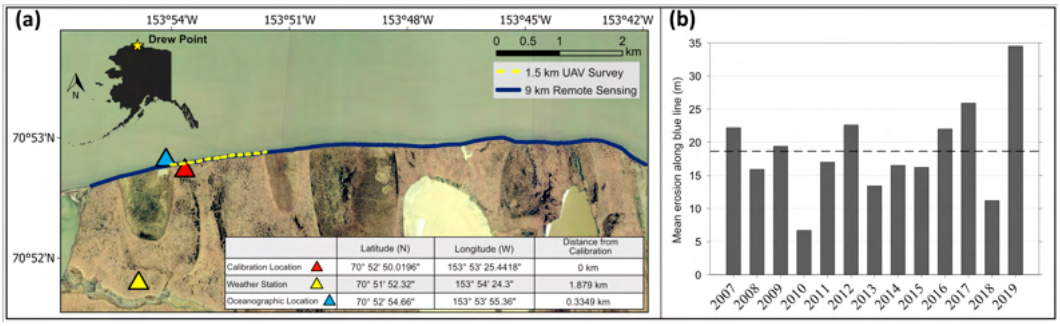

Figure 3. The Drew Point study area along the Alaskan Beaufort Sea. (a) The footprint of the 1.5 km stretch of repeated Aerial Unpersoned Vehicle (AUV) surveys is highlighted with a dashed yellow line and the 9 km stretch of repeated satellite retrievals is highlighted with a blue line. The locations of the calibration site (red triangle), meteorological station (yellow triangle), and modeled ocean environment (cyan triangle) are identified graphically, coordinates are given in the inset table. (b) Mean annual erosion rates along the 9 km (blue) stretch of Drew Point between 2007 and 2019 provided by (B. M. Jones et al., 2018; Ward Jones et al., To be Submitted).

Drew Point is located along the low-lying tundra landscape of the Alaska Coastal Plain and the coastline consists of relatively tall (∼2-7 m) permafrost bluffs and narrow beach. Permafrost here consists of both ice-bonded sediments and ice wedges (Figure 1(a)). Ice-bonded sediments are sections of permafrost in which there is a mixture of pore ice and sediments/soils whereas ice wedges are vertical veins of mostly ice. Ice wedge polygons are geometries in which ice wedges define polygonal shapes composed of ice-bonded sediments. Ground-ice content at Drew Point is very high, with segregated and pore ice volumes of 50-80% and ice wedge volumes of up to 30% (Kanevskiy et al., 2013; Wobus et al., 2011). We collected permafrost cores from three surface geomorphic classifications that are characteristic of the region: primary material that has not been reworked by thermokarst lake formation and drainage ("PM"), an ancient drained thermokarst lake basin (DTLB) which drained ∼5 kyr BP ("DP1") (Hinkel et al., 2003; M. Jones et al., 2012), and a young DTLB where most recent drainage occurred ∼0.5 kyr BP (DP2) (M. Jones et al., 2012). Below tundra vegetation and peat, near-surface sediments consist of Holocene-age soils and/or lacustrine silts. Deeper sediments (< ∼3 m elevation) consist of marine silts and clays deposited during a late Pleistocene marine transgression (Bristol et al., 2021).

The ACE model primarily has input properties and calibration data defined within the ancient DTLB (DP1) site identified with a red triangle in Figure 3. This site is both part of the traditionally monitored 9 km stretch, as well as repeated Aerial Unpersoned Vehicle (AUV) surveys along a smaller 1.5 km stretch in 2018 and 2019 (Ward Jones et al., To be Submitted) included in the ACE model observational campaign.

2.1 Study Area Properties

Site specific data needed to define ACE model input properties were collected at the polygon with a red triangle in Figure 3. These data define the geometry of the simulation, as well as the mechanical and thermal model properties. These are time-invariant quantities expected to be broadly applicable to other ancient DTLBs along Drew Point, which possess large, well-developed ice wedges that form hexagonal high-centered polygons.

As established through field observations, the polygon of interest is approximately 10.8 m wide by 6 m into the land (between 5.95 and 6.22 m), and is 5.2 m high on July 1, 2018. There is little to no beach before the toe of the bluff. A thick ice wedge of up to 4 m thickness surrounds the polygon but does not extend all the way to the toe of the bluff, likely only to 4.9 m.

The natural and heterogeneously shaped polygons shown in Figure 1 and in Figure 4(a) must be translated into finite element representations to model erosion within ACE. An archetypal representation of this polygon in the ACE model is shown in Figure 4(b). Although not required, repeating patterns of homogeneous shapes are most easily fabricated and meshed, and hence are the default archetypal representation. The calibration study presented in this work is conducted on a one-element thick slice from the center of the archetypal representation as shown in Figure 4(c). This quasi-2D geometry is discussed more fully in Section 4.1, but it is noted here that a current lack of parallelization has required domains of this scale. The material blocks in Figure 4(c) are necessary for the mechanical component (Section 4.3), however peat and ice-bonded sediments are treated continuously in the thermal component (Section 4.2).

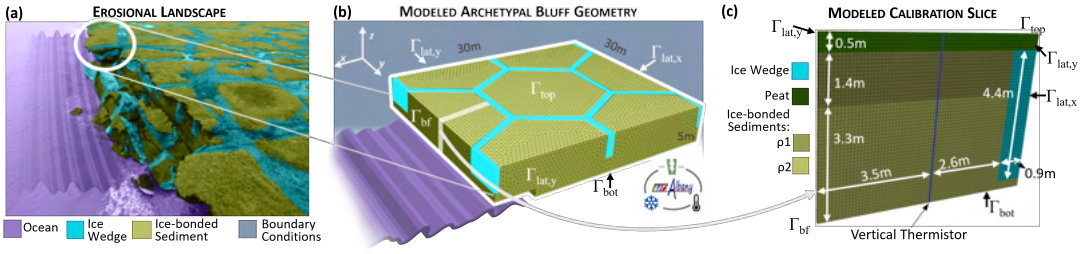

Figure 4. The terrestrial computational domain is designed to mimic the natural polygons measured and observed in the field as shown in panel (a). The location is regularized into an archetypal bluff geometry as shown in panel (b) with multiple repeating polygons. Identified here are the four relevant boundaries on which appropriate boundary conditions are prescribed: the bluff face boundary (Γ_{bf}), the bottom boundary (Γ_{bot}), the top boundary (Γ_{top}) and the lateral boundary ($\Gamma_{\text{lat,x}} \cup \Gamma_{\text{lat,y}}$). Calibration is performed on a one-element thick slice from this archetypal representation, shown in panel (c). Colors identify the four separate material blocks (with $\rho_{1,2}$ identifying distinct densities of ice-bonded sediments) and initial dimensions are identified on the slice. These material blocks are used within the mechanical component (Section 4.3), however the thermal component (Section 4.2) treats the peat and ice-bonded sediments continuously.

2.1.1 Constituent Material Characterization of Ice-bonded Sediments

The thermal model input properties were assigned from permafrost characterization enabled through permafrost core retrieval field work in April 2018. Ancient DTLB sections along a retrieved 7.5 m core length were used to establish: salinity, organic carbon content, water mass for effective porosity, and soil/sediment masses, grain sizes, and bulk densities in ice-bonded sediments as detailed in (D. L. Bull et al., 2020; Bristol et al., 2021, 2020). PM and young DTLB cores were also used in aiding salinity characterization. Best high-order polynomial and logistic regression of these data were then used as the components in the thermal mixture models first detailed in (Frederick et al., 2021) and described more fully in Section 4.2.3.

Organic carbon content was measured using an elemental analyzer (Bristol et al., 2021), and peat content was estimated by assuming that organic carbon composes 50% of peat biomass (Pribyl, 2010). Following the the work of (Pribyl, 2010), peat mass percent is recovered from measured carbon content through multiplication by 2. Since sand, silt, and clay fractions were obtained in the absence of peat, these values had to be scaled post-fractional assignment to accommodate the volume that peat occupies. Figure 5 panel (a) shows the mass fractional assignments of the constituent materials (sand, silt, clay with scaled measured fractions and peat) as a function of elevation. As shown, peat is dominant near the surface, due to the organic layer, but decreases rapidly with depth. The majority of the ice-bonded sediment consists of unconsolidated clay and silt.

Figure 5 also shows the ice-bonded sediment effective porosity in panel (b), and panel (c) shows salinity. Effective porosity is equal to the percentage of volumetric ice content from the total volume and is calculated using water mass and core section volume measurements, assuming all pore space was filled with ice. The measured effective porosity generally decreases with depth. High porewater salinity at elevations near sea level (saline permafrost in Figure 1(a)) lead to the formation of a "cryopeg", which is permafrost that is unfrozen at temperatures < 273.15 K due to dissolved solids that reduce the freezing point (Bristol et al., 2021; Iwahana et al., 2021).

In all cases, measured core values (symbols) are fit (solid line) with a third order polynomial or logistic curve detailed in Table 1. The current study focuses on the retrieved ancient DTLB core in which a thermistor probe was placed, however the observational campaign was larger (D. L. Bull et al., 2020; Thomas et al., 2020; Bristol et al., 2020, 2021; Ward Jones et al., To be Submitted) In Figure 5, data that was measured but not used in developing the fits is shown with a muted color; reported R^2 values in Table 1 are evaluated on solid-colored data points. Additionally, if the core represents a distinct geomorphic classification (i.e., drained thermokarst lake basin or primary material that has not been reworked by thaw lake processes), a distinct symbol is employed.

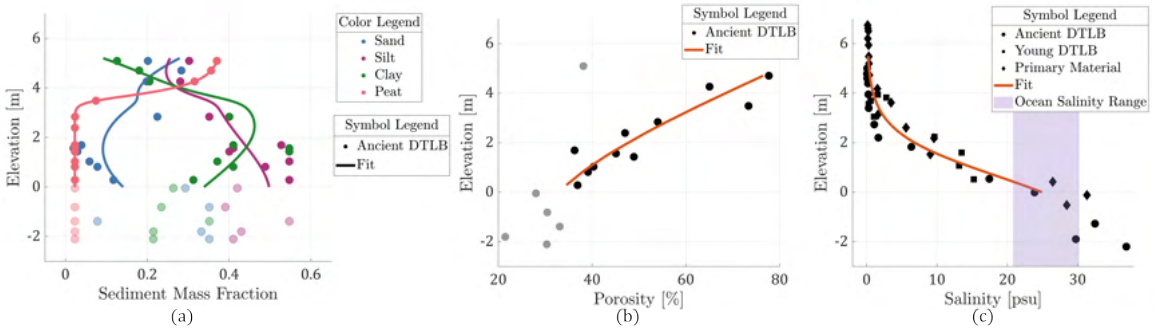

Figure 5. In all cases, measured core values (markers) are fit (solid line) with a third order polynomial or logistic curve detailed in Table 1. (a) Ice-bonded sediment fractions for each component as a function of elevation for an ancient DTLB geomorphology. (b) Ice-bonded sediment porosity as a function of elevation for an ancient DTLB geomorphology. (c) Porewater salinity as a function of elevation.

Table 1. Summary of parameter values for the fits to the experimentally derived ice-bonded sediment constituents. For the first four variables, the best fit is of the form of $v(z) = a + bz + cz^2 + dz^3$ where z is the elevation (m) and $v(z)$ is variable being modeled. Peat fraction and porewater salinity were represented by a logistic curve of the form $P(z, z_c) = a + \frac{b-a}{\left(c+d\exp^{f(z-z_c)}\right)^{\frac{1}{\nu}}}$.

Variable, units	a	b	c	d	f	z_c	ν	R^2
Porosity, %	32.91	5.25	1.23	-0.08	–	–	–	0.86
Sand fraction, F_{sand}	$14.41e^{-2}$	$-6.37e^{-2}$	$1.87e^{-2}$	$9.00e^{-4}$	–	–	–	0.62
Silt fraction, F_{silt}	$50.95e^{-2}$	$-1.23e^{-2}$	$-1.96e^{-2}$	$3.50e^{-3}$	–	–	–	0.79
Clay fraction, F_{clay}	$34.65e^{-2}$	$7.59e^{-2}$	$9.00e^{-4}$	$-4.40e^{-3}$	–	–	–	0.82
Peat fraction, F_{peat}	$38.00e^{-2}$	$2.30e^{-2}$	$1.00e^{-2}$	$1.00e^{-2}$	9.0	3.5	4	1.0
Salinity, psu	0.058	36.91	1.0	1.0	1.11	0.657	1	0.96

2.1.2 Mechanical Characterization of Ice-bonded Sediments

Experimentation on retrieved permafrost was also used to establish three mechanical material properties utilized by the terrestrial model: elastic modulus, compressive yield strength, and tensile yield strength. Mechanical stress strain properties as a function of ice saturation (f) and porosity (θ) were obtained through direct tensile, Brazilian tensile strength, and unconfined compressive strength testing as detailed in (D. L. Bull et al., 2020). Distinct compositions of ice saturation and porosity were achieved by controlling the testing chamber temperature and selecting distinct sections of the core respectively. These experimental values are denoted with the black diamond (PM material) and circle (ancient DTLB material) markers in Figure 6(a)-(c). These experiments were unique in that they used natural cores, not remodeled cores, affecting experimental reliability as sample preparation and testing were subject to many uncontrollable degrees of freedom.

For the elastic modulus and compressive yield strength, bilinear fits were employed to develop continuous expressions for the variation of these properties with ice saturation and porosity. The main challenge with limited data is to produce physically realistic behavior (i.e. positive and nonzero elastic modulus) across the entire space of ice saturation and porosity regimes considered (in this study, $f \in [0, 1]$ X $\theta \in [0, 1]$). To address this, two strategies were employed: bounding "theoretical" values to guide the fits, and minimum allowable values for each property.

First, bounding values (shown with triangular data markers in Figure 6(a)–(b)) were used in developing the fits for material property values at the points (f, θ) = $(0, 0)$, $(0, 1)$ (a material approaching pure water), $(1, 0)$, and $(1, 1)$ (a material approaching pure ice). For the first three points, a bounding value of 0 MPa was used for both elastic modulus and compressive yield strength. For the last bound point, a material approaching pure ice, values of 5 MPa for compressive yield stress (Petrovic, 2003) and 1000 MPa for elastic modulus were employed; the elastic modulus bound was selected by extending the elastic modulus linear fit presented in (Li et al., 2022) to 100% ice content. Table 2 details the bi-linear regressions employing the experimentally derived mechanical properties. Similar frozen rock ballast studies varying porosity and temperature show equivalent trends with slightly larger yield and elastic modulus values (Li et al., 2022).

Despite employing these bounding values, the best fit curves exhibit nonphysical behaviors in areas where f, $\theta \to 0$. These are regions for which material definition is difficult, and thus a constant but higher than 0 MPa minimum value is applied. These minimum allowable values for elastic modulus and compressive yield strength are referred

to as E_{m} and Y_{m} respectively, and are indicated by the lilac-shaded planes in Figure 6. A predominant focus of the ACE model calibration is in determining appropriate values for these two parameters, with an emphasis on the minimum allowable elastic modulus, as this largely controls the rate of denudation (described more fully in Sections 4.3.3 and 5.2).

Table 2. Summary of parameter values for the best bi-linear regressions shown in Figure 6 for the experimentally derived elastic modulus and compressive yield stress with bounding theoretical points. A bi-linear fit of the form $M(f,\theta) = a + bf + c\theta + df\theta$ was used to establish variation of ice-bonded sediment material elastic modulus and compressive yield stress as a function of ice saturation f and porosity θ. It is of note that the R^2 values reported are evaluated based on experimental data and theoretical bounds utilized in generating the surface fits. Section 5 details the selection of the minimum allowable values which will truncate these regressions and are shown as lilac planes in Figure 6.

Variable	a	b	c	d	R^2
Elastic modulus [MPa]	-24.69	-167.7	-25.95	819.1	0.587
Compressive Yield stress [MPa]	-0.042	-0.297	-0.042	4.701	0.918

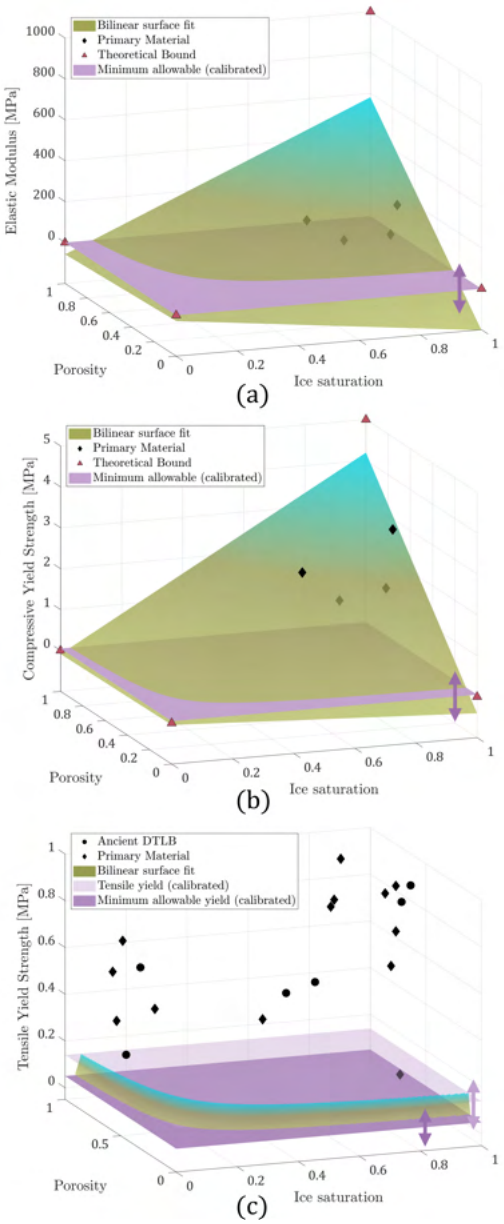

Figure 6. Measured core values for elastic modulus (a), compressive yield strength (b), and tensile yield strength (c) are shown with symbols. Black diamonds indicate experimental data obtained from Primary Surface cores, circles from Ancient Drained Lake Basin cores, and red triangles indicate theoretical values used to guide and bound the surface fit. For panels (a)–(b), the displayed bi-linear surface is detailed in Table 2. The lilac planes represent parameters which are calibrated in the model; in panels a-b the minimum allowable values will be imposed on each of the curves, and on panel (c) in addition to the minimum allowable value, a constant tensile yield will be calibrated.

Establishing the continuous representation of tensile yield strength with ice saturation and porosity followed a different approach. For pure ice, tensile and compressive yield behaviors are known to be sufficiently distinct with tensile yield strengths exhibiting little dependence on temperature (albeit in a much colder 253.15 K to 263.15 K range)

(Petrovic, 2003). Figure 6(c) displays experimentally derived tensile yield strengths from direct tensile and Brazilian tensile tests (described in more detail in (D. L. Bull et al., 2020)) over a range of f and a smaller range of θ. These magnitudes vary between -0.11 MPa and -1.00 MPa and do not seem to exhibit a strong relationship with f and θ. These are lower than those found by (Petrovic, 2003) for tensile strength of pure ice at much higher f (between -0.7 and -3.1 MPa). Given the spread of tensile yield behavior, we opted to use a single value independent of f and θ for tensile yield strength. Appropriate selection of this value is another significant component of the calibration study. As shown in Figure 6(c), the bilinear fit developed for compressive yield strength will still be used for material in tension (along with the corresponding minimum allowable compressive yield strength), but this surface will be upper-bounded by the single calibrated tensile yield value. The effect of this is that material in regimes of low ice saturation/porosity will still exhibit tensile yield stress behavior governed by the bilinear fit developed for compressive strength, but elsewhere its tensile yield behavior will be dictated by the single calibrated value for tensile yield strength.

2.2 Environmental Drivers and Observations

Time evolving data that define the environmental drivers and capture the specific response of the polygon identified with a red triangle in Figure 3 were also observed. Most of these observations are described in detail in Section 5.1 as they are the basis of the erosion calibration. Erosion measurements were collected through four repeat AUV surveys as well as from daily-resolved time-lapse calibrated images. Niche measurements are inferred from vertically resolved temperature changes, as measured hourly by a thermistor string placed within the void left by the 7.5 m long core. This is the first dataset, to our knowledge, that captures hourly-resolved niche formation and ensuing block collapse offering an unparalleled calibration opportunity for the ACE Model. These calibration observations will be referred to throughout the paper before they are formally introduced in Section 5.

In addition to the calibration observations, environmental conditions were measured by a permanent USGS weather station (see yellow triangle in Figure 3) (Urban & Clow, 2018; Urban, 2021). Observational measurements of air and subsurface temperatures from 5 cm to 120 cm depth at 5 cm increments were collected hourly. The 5 cm temperature was used as the atmospheric boundary condition in the thermal component of the terrestrial model, see Section 4.2. The subsurface temperature profiles were used in defining the initial temperature boundary condition and are used to increase confidence in the thermistor string measurements (see overlapping regions in Figure 14) as well as increase knowledge of near surface behavior.

3 Ocean Model

3.1 Model Description

Capturing storm-resolved interactions of the ocean with a spatially resolved permafrost coastline requires a high resolution oceanographic modeling suite. In this case, we utilize the natively coupled nearshore circulation and wave models provided by the Delft3D suite (Delft3D-FLOW (Deltares, 2018a) and Delft3D-WAVE (Deltares, 2018b; Holthuijsen et al., 1993), respectively) forced by a larger Arctic Ocean scale wave model (WAVEWATCH III® (WW3) ((WW3DG), 2019)) to resolve the dynamic interaction of swell, wind waves, wave induced setup, and water levels. This provides time-varying water levels inundating the bluff face, with associated temperatures and salinity's, as a series of boundary conditions for the terrestrial erosion model (see purple text in Figure 2).

The first of the three-model system is the application of a spectral wave model, WW3, to provide wave field information at an Arctic Ocean scale. A polar stereographic, curvilinear WW3 grid covering the Arctic Ocean developed in (Rogers & Zieger, 2014) is used; it is polar centric and extends south to 65°N, with horizontal resolution is 18 km at 70°N. Bathymetric data for the model domain was obtained from the ETOPO1 1 arc-minute global relief model (Amante & Eakins, 2009).

To provide higher resolution oceanographic predictions in ice-free conditions around Drew Point, Delft3D-FLOW and WAVE models were developed to provide nearshore circulation and wave predictions, respectively. Delft3D-WAVE uses SWAN, a proven nearshore and shallow water spectral wave modeling system, as the wave model and is natively coupled to Delft3D-FLOW, providing an efficient computational environment. The water level set-up due to waves in shallow waters as well as the net momentum flux (radiation shear stress) captured by Delft3D-WAVE can be resolved and incorporated directly into Delft3D-FLOW simulations through a two-way coupling. Bottom elevations for the Delft3D-FLOW and Delft3D-WAVE grid were defined from the Alaska Regional Digital Elevation Model (ARDEM) version 2.0 (S. L. Danielson et al., 2015; S. Danielson et al., 2011, 2008). The ARDEM data were interpolated onto the Delft3D grid so that each cell has a single depth value. The Delft3D-FLOW structured curvilinear grid consists of 31,072 elements in a single vertical layer with 2 km resolution at the northernomost extent. The grid becomes more refined closer to the coast and in the region surrounding Drew Point, where the resolution increases to 100 m. The Delft3D-WAVE structured curvilinear grid has 3 km resolution at the northernmost extent with increased refinement down to 400 m along the coastline.

Variables from Delft3D-FLOW (i.e., water level ($s(t)$), salinity ($S_o(t)$), water temperature ($T_o(t)$)) were output at 15-minute intervals and variables from Delft3D-WAVE (i.e., mean wave parameters, 1D wave spectra) were output at 1 hour increments for the entire simulation period. A 2 Hz water surface elevation, $\eta(t)$, was computed from the 1D wave spectra variance density according to:

$$\eta\left(t\right) = \sum_{S} a_S \cos\left(2\pi f_S t + \theta_S\right), \text{ where } a_S = \sqrt{2 S_f \Delta f} \text{ and } \theta_S = \text{random}\left(0, 2\pi\right). \quad (1)$$

In Equation (1), $\eta(t)$ is the time varying water elevation, a_S is the amplitude of the surface displacement calculated using the variance density at each frequency S_f, Δf is the difference in each frequency, f_S is the frequency, t is the time, θ_S is the wave phase represented by a random number between 0 and 2π, computed at each frequency S.

To compute a water contact history with the bluff face, the water level, $s(t)$, from Delft3D-FLOW was linearly interpolated onto a 2 Hz time series and added to the $\eta(t)$ signal, i.e. $w(t) = s(t) + \eta(t)$. Additionally, the salinity and water temperature from Delft3D-FLOW were also linearly interpolated to the same 2 Hz time step. As detailed throughout this paper, the water contact history, pressure from wave contact, salinity, and temperature are all employed by the terrestrial model as various boundary conditions specified to evolve the state of the permafrost.

3.2 Boundary Conditions

Generating the wave environment from these models requires a series of time dependent boundary conditions comprised of environmental parameters like wind speeds and temperatures. Wind forcing and sea ice boundary conditions are required for the circum-Arctic WW3 domain are linearly interpolated from hourly ERA5 reanalysis data ((C3S), 2017) from July through November 2018. This wind reanalysis was also used to provide forcing for the Delft3D-FLOW model.

In addition to requiring wind forcing, Delft3D-FLOW requires hydrodynamic boundary conditions including water levels and scalar quantities such as temperature and salinity. Water level data, from the NOAA Prudhoe Bay, AK station (Service, 2019), was applied uniformly across the Delft3D-FLOW model domain. The GOFS 3.1 (developed by the US Naval Research Laboratory, 2017) water temperature and salinity data were linearly interpolated to locations corresponding to the outer boundaries of the Delft3D-FLOW grid. Data were pulled from the surface layer of the GOFS 3.1 model, representing the top 2 m of the water column. It is important to note that although ocean water temperatures below 273.15 K were present in GOFS 3.1, these were are not allowed as the Delft3D modeling suite does not allow for temperatures below freezing (Cummings & Smedstad, 2013; Cummings, 2005). Further, sea ice is not treated within in the Delft3D modeling suite (Cummings & Smedstad, 2013; Cummings, 2005).

Delft3D-WAVE obtained wave boundary conditions from WW3; the wind, water level, and current information are passed from the natively coupled FLOW model.

3.3 Oceanographic Conditions at Calibration Location

Output from the suite of oceanographic models was obtained ∼300 m from the calibration location as identified by a cyan triangle in Figure 3. The raw 2 Hz time history of water contact ($w(t)$) is shown in light blue in Figure 7 (note, all modeling completed using GMT). This time history has been shifted by 0.24 m to establish the same zero-elevation between the oceanographic and terrestrial models as detailed in (D. L. Bull et al., 2020). For the purposes of this analysis, we consider an oceanographic storm to be periods of 12 or more consecutive hours consisting of 2 Hz water contact levels, $w(t)$, at or above 0.4 m; in Figure 7, such storms are identified with grey shading, with the actual duration of the storm given above the grey area. The block breakage event is identified with a dashed black line.

Up to the time of failure, the calibration location experienced 10 storms intermixed with quiescent periods. Table 3.3 below identifies oceanographic characteristics between the beginning of simulation in 2018 through the time of block failure; time periods are sectioned by field observations. The percentage of time water is in contact with identified elevations are normalized by the duration of time between sections. Average water contact levels do not indicate dramatically different regimes, however it is clear from the elevation data that the six storms between Aug. 4 and Sept. 9 were the most powerful with greater percentages of time in contact with higher bluff elevations. From Table 3.3 and visually from Figure 7 it is clear that a few large storms dominated the exposure of the bluff to oceanic water, especially the two storms between Sept. 1 and Sept. 9.

Date	% time $w(t) \leq 0$	% time $w(t) > 0.2$ m	% time $w(t) > 0.4$ m	% time $w(t) > 0.8$ m	Average $w(t)$ (m)	Number of storms	Average Water Temperature (K)	Average Salinity (psu)
Jul. 1 – Jul. 25	14.7	31.6	5.49	0.02	0.16	4	273.15	30.05
Jul. 25 – Jul. 30	12.8	46.6	6.94	0.00	0.19	2	273.15	29.96
Jul. 30 – Aug. 4	36.4	19.4	0.95	0.00	0.10	0	273.15	29.88
Aug. 4 – Sept. 1	39.6	24.3	8.52	0.57	0.13	4	273.61	28.74
Sept. 1 - Sept. 9	21.7	44.4	15.0	2.52	0.21	2	274.25	27.53

Table 3. Oceanographic characteristics between field observations over the 2018 summer in Drew Point Alaska. Water contact statistics (average contact levels and % of time in contact with identified elevations), temperature, salinity, and number of storms identified.

3.3.1 Generating Water Exposure Boundary Conditions

Although the variation of water on the bluff face occurs over fractions of a second, the thermal evolution of the permafrost, governed by conduction, is a much slower process (tens of minutes), and consequently the terrestrial model generally uses much larger timesteps than those used in the oceanographic modeling component. Additionally, the usage of water level data by the terrestrial model requires water level to be sampled on its own (vertical) spatial discretization. Hence the water level, salinity, and temperature were further processed to ensure the total mechanical and thermal energy delivered to the terrestrial model from the ocean is harmonized with the terrestrial model setup (both the simulation time step and vertical discretization).

To achieve this, an "exposure" time history, $w_{\text{terr}}(t)$, is constructed by sampling at the same spatial and temporal discretization as used by the terrestrial model. This processing seeks to evaluate the *cumulative duration* of water contact with the bluff per elevation of the original $w(t)$ over each hourly update to the wave spectrum (see Section 3.1) and ensure cumulative duration's are integer numbers of the terrestrial time-step. This construction ensures that each level of the bluff face is exposed to ocean water for the entirety of the simulation time step. If a level on the bluff face is cumulatively exposed for a period shorter than the simulation time step, this will not be included in the "exposure" time history. For a more detailed overview of the process for generating these wave exposure histories, the interested reader is referred to Supporting Information Text S1.

In the limit of small simulation time steps (0.5 seconds) and fine mesh discretization (0.01 m) the original water contact history, $w(t)$, would be recovered as the exposure time history boundary condition, but would have significant computational impacts. Sensitivity studies were completed in (D. L. Bull et al., 2020) that shows that the mesh discretization and coupling time step have a large control over the water exposure boundary conditions (Figures 5.1-4 and 5.1-5 within (D. L. Bull et al., 2020)); the coupling time

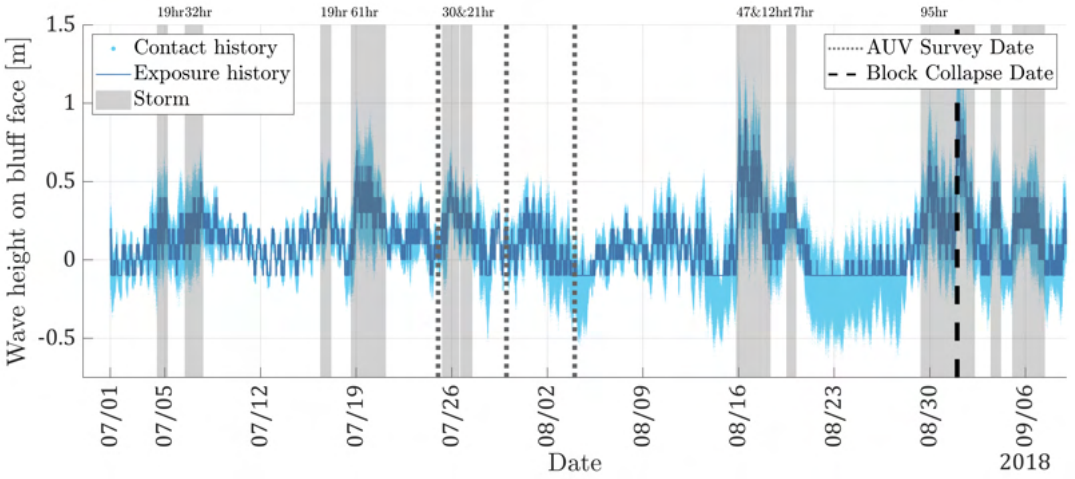

Figure 7. The ocean contact history is shown in light blue and the exposure history used to generate the Dirichlet temperature boundary conditions and Neumann pressure boundary conditions is shown in dark blue. An elevation of 0 m identifies the location of the toe of the bluff and thus values below this line indicate periods when no ocean water was in contact with the bluff face. The AUV surveys are identified with grey vertical dotted lines and the block breakage event is identified with the vertical black dashed line. Grey shading indicates periods of ocean storms, identified from the water contact history (light blue), and the duration's of the storms are identified at the top of the figure.

step, in particular, has a strong control over the representation of the highest water contact levels.

Figure 7 illustrates the impact of achieving the water exposure boundary conditions, $w_{\text{terr}}(t)$, with the dark blue data using a time step of 900 sec and grid resolution of 0.1 m. The effect of the exposure metric is clear: the peak levels decrease because these peak levels are in contact with the bluff face for less than 900 sec. This water exposure boundary condition is used to determine which cells are submerged by the ocean, which in turn will alter boundary conditions in the thermal problem (the temperature and salinity boundary conditions detailed in Section 4.2.2) and the mechanical problem (the pressure boundary condition as well as the minimum elastic modulus value applied ($E_{\text{m,o}}$) detailed in Section 4.3.2).

4 Terrestrial Model

The terrestrial component of the ACE model is based on a 3D thermo-mechanical finite element formulation within the open-source parallel HPC code known as `Albany-LCM`. `Albany-LCM` can be downloaded from `https://github.com/sandialabs/LCM`, and was created as a fork from the `Albany` code, located at `https://github.com/sandialabs/Albany`; for more detail on `Albany`, the interested reader is referred to (Salinger et al., 2016)) (Frederick et al., 2021). A thermal problem (Section 4.2), using the material model described in Section 4.2.3, solves the governing equations for 3D heat conduction in a porous media with solid-liquid phase change including the effects of salinity on pore fluid melting temperature. A mechanical problem (Section 4.3), using the material model outlined in Section 4.3.3, solves the governing equations for a 3D standard J_2 plasticity model extended to the large-deformation regime. Each subsection (4.2 and 4.3) first discusses

more generalized descriptions of the model components, and then provides additional details related to the specific implementation of the model at Drew Point, AK utilized for the presented calibration study. Novel to the ACE model is the interaction between the thermal and mechanical components of the terrestrial model, as detailed more fully in Section 4.4. Frozen water content in the ice-bonded sediment material, as calculated by the thermal material model, is used by the mechanical material model to define the local mechanical material properties, specifically the elastic modulus and yield strength. In this way, deformation and failure are coupled to the thermal state of the material, as calculated, rather than prescribed *a priori*. The reader is referred back to Figure 2 for an overview of the terrestrial component and interactions within as a guide for this section.

4.1 Calibration Study Simulation Domain

Although the finite element model is designed for full 3D geometry, as depicted in Figure 4(b), certain advanced features of the ACE terrestrial model—such as the moving pressure boundary condition—are not yet fully parallelized (see Section 4.3.4). This limitation constrains the mesh sizes that can be processed within a reasonable timeframe. To address this, we employ a one-element-thick slice of the original geometry for computational analysis in this calibration study. The dimensions of this slice match the relevant observed dimensions above and are detailed in Figure 4. We model only 0.9 m of the 4 m thick ice wedge, as it is exposed to boundary conditions solely along the top and undergoes minimal evolution during the simulated time frame.

While the thermal model accounts for continuously varying material properties throughout the domain, the mechanical model relies on material property definition per distinct element block. As a result, the mesh incorporates four separate material blocks: ice, a peat layer, and two ice-bonded sediment layers, each with distinct densities, material properties, and failure (erosion) criteria. Notably, the two ice-bonded sediment layers were chosen to capture a significant shift in bulk density due to the presence of peat (see Figures 5 and 9). As illustrated in Figure 4(c), the bottom ice-bonded sediment block spans 0 to 3.3 m in the z-direction (height), while the second ice-bonded sediment block extends from 3.3 to 4.7 m. The peat layer occupies 4.7 to 5.2 m, covering the ice wedge, which begins 0.3 m above the domain's base. As described in Sections 4.2 and 4.3, each material block is assigned unique definitions for mechanical and thermal properties.

The simplified geometry enables the use of 8-node hexahedral elements along with a structured mesh for discretization. This approach not only streamlines mesh generation but also minimizes potential numerical artifacts associated with more complex elements. The computational domain is discretized into 3,640 elements with a uniform mesh size of $h = 0.1$m, and the geometry remains one-element thick. Each element contains 8 nodes and 8 integration points. Primary variables, such as displacements and temperature, are stored at nodes, while state variables, including stress and ice saturation, are stored at integration points. Calibration simulations utilize a baseline time step of 900 seconds over a period of 2.5 months, typically requiring approximately 10 days of computational time.

Site-specific boundary conditions, described in subsequent sections, are applied to this geometry. The boundary $\partial\Omega$ is divided into four sub-boundaries: $\partial\Omega := \Gamma_{\text{bf}} \cup \Gamma_{\text{top}} \cup \Gamma_{\text{bot}} \cup \Gamma_{\text{lat}}$, where $\Gamma_{\text{lat}} := \Gamma_{\text{lat,x}} \cup \Gamma_{\text{lat,y}}$. Here, Γ_{bf} represents the bluff face, Γ_{top} the bluff top, Γ_{bot} the bluff bottom, and $\Gamma_{\text{lat,x}} \cup \Gamma_{\text{lat,y}}$ the remaining three lateral boundaries of the bluff, as shown in Figure 4.

578 ## 4.2 Thermal Component

579 ### *4.2.1 Governing Equations*

580 The thermal model follows the governing equation for heat transfer by conduction
581 in a saturated porous media including water-ice phase change, described by

$$\overline{\rho c_p}\frac{\partial T}{\partial t} = \nabla \cdot (\boldsymbol{K} \cdot \nabla T) + \Theta, \quad \text{in } \Omega, \tag{2}$$

582 where $\Omega \subset \mathbb{R}^3$ is a smooth bounded domain, ρ is the density, c_p is the specific heat,
583 T is the temperature, $\boldsymbol{K}$ is the thermal conductivity tensor, and Θ is the heat source
584 term due to phase change (latent heat). The bar over the term $\overline{\rho c_p}$ indicates a mixture
585 model for the density and specific heat of each material component. Considering poros-
586 ity as the ratio of the void volume to the total volume ($\theta = V_{\text{void}}/V_{\text{total}}$), the possible
587 material components include water and ice in the pore space (or void space), θ, and con-
588 stituent sediments (e.g. sand, silt, clay, peat) in the solid, $1 - \theta$. The water saturation,
589 w, and ice saturation, f, are defined as the fraction of water or ice occupying the effec-
590 tive pore space, respectively, and can vary from 0 to 1. The volume fraction of each ma-
591 terial component occupying the effective pore space is $S_f = \theta f$ for ice, and $S_w = \theta w$
592 for water. The mixture models for each thermal parameter are further described in Sec-
593 tion 4.2.3.

594 The source term Θ in Equation (2) is defined according to

$$\Theta := \rho_f L_f \frac{\partial f}{\partial t} = \rho_f L_f \frac{\partial f}{\partial T}\frac{\partial T}{\partial t}, \tag{3}$$

595 where ρ_f is ice density and L_f is the latent heat of water-ice phase change. The func-
596 tion $\frac{\partial f}{\partial T}$ represents the soil freezing curve and describes how ice saturation changes with
597 temperature. Equation (3) is non-zero only during phase change, and is further described
598 in Section 4.2.3.

599 Consistent with the apparent heat capacity method, the heat source term is refor-
600 mulated as a correction to the heat storage term,

$$\overline{\rho c_p}' := \overline{\rho c_p} - \rho_f L_f \frac{\partial f}{\partial T}. \tag{4}$$

601 Boundary conditions must be specified to complete the definition of the thermal prob-
602 lem and are described separately in Section 4.2.2.

603 It is straightforward to obtain the weak variational form of Equation (2):

$$\int_\Omega \left(\overline{\rho c_p} - \rho_f L_f \frac{df}{dT}\right)\frac{\partial T}{\partial t}\boldsymbol{\xi}\,\mathrm{d}V + \int_\Omega (\boldsymbol{K}\cdot\nabla T)\,\nabla\boldsymbol{\xi}\,\mathrm{d}V - \int_\Gamma \boldsymbol{\xi}\boldsymbol{q}\cdot\boldsymbol{n}\,\mathrm{d}S = 0, \tag{5}$$

604 where $\boldsymbol{\xi} \in \mathcal{V}$ is a square-integrable test function having a square-integrable first deriva-
605 tive, $\boldsymbol{q}$ represents a heat flux boundary condition on a given domain boundary Γ in the
606 case that one is applied, and $\boldsymbol{n}$ denotes the normal vector to Γ. As in Section 4.3, the
607 variational statement Equation (5) is satisfied by using a standard finite element discretiza-
608 tion in space, by means of isoparametric elements. For the presented work, Equation (5)
609 is advanced in time using a Forward Euler time-stepping scheme.

4.2.2 Initial and Boundary Conditions

4.2.2.1 General For the thermal PDEs (Section 4.2.1), a geothermal heat flux boundary condition of the form

$$\boldsymbol{K}\frac{\partial T(t)}{\partial z} = -\boldsymbol{q}(t) \text{ on } \Gamma_{\text{bot}}, \tag{6}$$

is prescribed on the bottom boundary, where $q(t)$ denotes heat flux, $\boldsymbol{K}$ is the thermal conductivity of the material at the bottom boundary, and $\frac{\partial T}{\partial z}$ is the temperature gradient with depth. This boundary condition is supplemented with a homogeneous Neumann boundary condition on the lateral boundary

$$\boldsymbol{K}\frac{\partial T(t)}{\partial x} = \boldsymbol{K}\frac{\partial T(t)}{\partial y} = \boldsymbol{0} \text{ on } \Gamma_{\text{lat}}, \tag{7}$$

and the following Dirichlet boundary conditions on the top and bluff face boundaries

$$T(t) = T_{\text{atm}}(t) \text{ on } \Gamma_{\text{top}}, \quad T(t) = \begin{cases} T_{\text{atm}}(t), \text{ on } \Gamma_{\text{bf}} \text{ if exposed to atmosphere} \\ T_{\text{ocean}}(t), \text{ on } \Gamma_{\text{bf}} \text{ if submerged under water} \end{cases} \tag{8}$$

where $T_{\text{atm}}(t)$ and $T_{\text{ocean}}(t)$ are the atmospheric and ocean temperatures at the bluff face. The values of these field are obtained from observational (e.g., weather station) data, or by running models (e.g., the oceanic model (Section 3) or Earth System Models). Note that it is not strictly necessary to use an air temperature as the atmospheric temperature, a skin temperature or 5 cm depth temperature could be used.

4.2.2.2 Drew Point Application The initial condition for the temperature is applied using a best fit curve to the vertical thermistor (see Section 5.1) and subsurface weather station data (see Section 2.2) recorded at July 01, 2018, 3:07:00 UTC, shown with a dashed black line in Figure 14 and given by the expression

$$T(z) = 265.02 + 0.2z - 4.9e^{-2}z^2 + 6.3e^{-2}z^3, \; R^2 = 0.9925, \tag{9}$$

where z is elevation. The initial ice saturation field is calculated according to the initial temperature field and the freezing curve determined by the material model.

Dirichlet boundary condition temperature values, from Equation (8), are shown in Figure 8; the wave exposure data described in Section 3.3.1 is used to determine whether or not an element along Γ_{bf} is submerged under water or exposed to the atmosphere. The atmospheric temperature T_{atm}, dark blue in Figure 8, is provided by subsurface weather station data at 5 cm depth, interpolated using a piecewise cubic to match the simulation time step. The oceanic temperature T_{ocean}, cyan in Figure 8, is provided by the oceanographic modeling suite. Ocean temperatures were cool over the 2018 calibration period; these cool values were confirmed with an independent dataset in (Ward Jones et al., To be Submitted). Given that ocean temperatures rarely went above 273.15 K, the majority of the season possesses the Delft3D-FLOW default value of freezing, only surpassing the warmer surrounding air temperature at the end of the season in September. As inferred in (Ward Jones et al., To be Submitted) it is likely that this low temperature had an effect on the efficacy of niche formation.

The Neumann boundary condition on Γ_{bot} is given as a constant geothermal heat flux derived from conditions on July 1st at 0 hrs. The temperature gradient at the bottom of the long vertical thermistor observing niche development (see Figure 14) was evaluated to yield a temperature gradient of $\partial T/\partial z = -0.23 \; K/m$. Combined with a thermal conductivity of 3.25 W K^{-1} m^{-1} derived from Figure 9, this yields a $\boldsymbol{q} = -0.76$ W/m^2.

A summary of the applied initial and boundary conditions are given in Table 5.

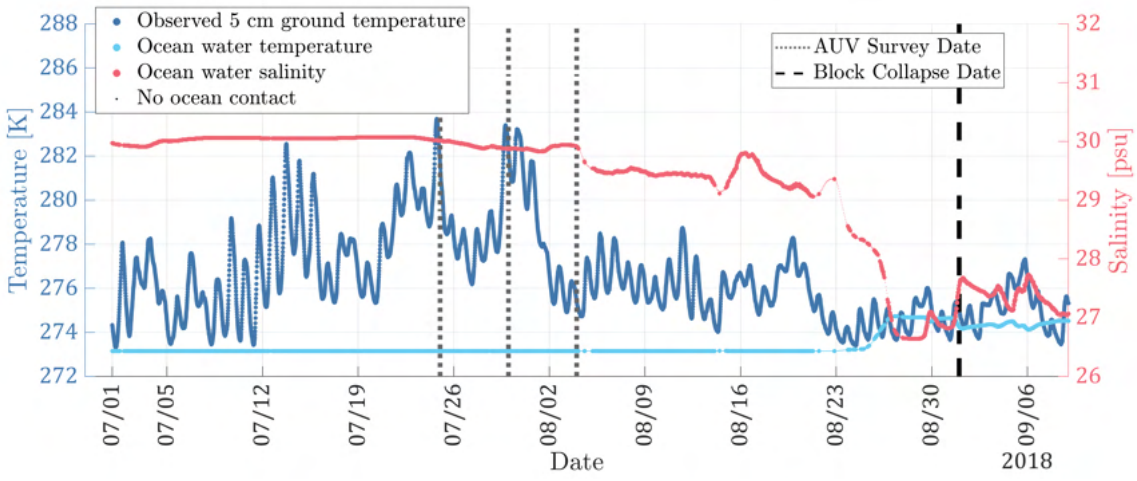

Figure 8. Temperature boundary condition magnitudes and salinity parameterization magnitudes applied to the bluff top and face (Γ_{top} and Γ_{bf}). The two blue curves identify the magnitude of the Dirlichet boundary condition temperature values on the bluff top and face. Instances in time for which the ocean water temperature was used at some level (as identified by the dark blue line in Figure 7) are identified with larger symbols. Note, the limitation of DelftFLOW to not accept temperatures below freezing (273.15 K) manifest in a straight freezing value through mid-August. The ocean salinity magnitude is shown in red on the right-hand axis. Instances in time for which the ocean salinity was used at some level (as identified by the dark blue line in Figure 7) are identified with larger symbols. The UAV surveys are identified with light grey vertical lines and the block breakage event is identified with the vertical black dashed line.

4.2.3 Material Model

4.2.3.1 General The thermal material model defines the bulk values of density, specific heat, and thermal conductivity, as well as the soil freezing curve (describing how ice saturation changes with temperature, $\frac{\partial f}{\partial T}$), based on the material constituents (ice, water, and sediment component fractions). A mixture model for the bulk-averaged density and specific heat (denoted by an over-bar) is then defined as

$$\overline{\rho} = S_f \rho_f + S_w \rho_w + (1 - \theta)\, \rho_s, \tag{10}$$

where ρ_w and ρ_s are the densities of water and sediment, respectively, and

$$\overline{c_p} = S_f c_{p_f} + S_w c_{p_w} + (1 - \theta)\, c_{p_s}, \tag{11}$$

where c_{p_f}, c_{p_w}, and c_{p_s} are the specific heats of ice, water and sediment, respectively.

The thermal conductivity tensor $\boldsymbol{K}$ can account for anisotropic materials; however, here we assume isotropic behavior, so that $\boldsymbol{K} := \kappa \boldsymbol{I}$, where $\boldsymbol{I}$ is an identity matrix, and $\kappa > 0$ is the isotropic value of the thermal conductivity. A volume-averaged mixture model for the bulk-averaged thermal conductivity $\overline{\kappa}$ is used, and is defined as

$$\overline{\kappa} = \theta\, (S_f \kappa_f + S_w \kappa_w) + (1 - \theta)\, \kappa_s \tag{12}$$

where κ_f, κ_w and κ_s are the thermal conductivities of ice, water and sediment respectively.

The values for ρ_s, c_{p_s}, and κ_s can be calculated with knowledge of the sediment composition and is based on a simple mass-averaged mixing model,

$$\zeta_s = F_{\text{peat}} \zeta_{\text{peat}} + F_{\text{sand}} \zeta_{\text{sand}} + F_{\text{silt}} \zeta_{\text{silt}} + F_{\text{clay}} \zeta_{\text{clay}}, \tag{13}$$

where ζ represents either ρ, c_p, or κ, and F_i denotes the peat, sand, silt, or clay mass fraction in the sediment mixture, depending on $i \in \{\text{peat}, \text{sand}, \text{silt}, \text{clay}\}$.

The freezing of saturated soils is a very complex process and depends on a number of factors, including but not limited to pore fluid salinity, sediment type, and pore size. In general, pore water freezing is mainly determined by the solution properties for pores larger than 0.2 μm, but for pores smaller than 0.2 μm, the effect of pore size on water freezing becomes important (Wan & Yang, 2020). Experimental studies by (M. Darrow et al., 2009), (M. Darrow, 2011), and (Kruse & Darrow, 2017) are used as the basis for soil freezing curves for clay and silt. A generalized logistic curve is used to describe the soil freezing curve, which gives the ice saturation, f, as a function of current temperature, T, and freezing temperature, T_f:

$$f(T, T_f) = A + \frac{D - A}{\left(C + Q e^{-G[T - (T_f - T_{\text{shift}})]}\right)^{1/v_{\text{bulk}}}}. \tag{14}$$

Equation (14) is a key component to correctly capturing the heat source due to phase change in the governing equation for heat transfer (see Equations (2) and (3)). The parameters (e.g., A, D, etc.) in Equation (14) dictate the general shape of the freezing curve and its width, with v_{bulk} in particular controlling the tail drop-off of the logistic curve.

The parameter v_{bulk} in Equation (14) is material-dependent and calculated according to

$$v_{\text{bulk}} = F_{\text{peat}} v_{\text{peat}} + F_{\text{sand}} v_{\text{sand}} + F_{\text{silt}} v_{\text{silt}} + F_{\text{clay}} v_{\text{clay}}. \tag{15}$$

The values of v_i for $i \in \{\text{peat}, \text{sand}, \text{silt}, \text{clay}\}$ are selected to be sediment-dependent, as (M. Darrow et al., 2009) shows that composition affects the freezing behavior of soils.

The freezing/melting temperature, T_f, is a function of the pressure and salinity of the pore water. The volume change that occurs during ice-water phase change is ignored. The freezing/melting temperature is calculated according to (UNESCO, 1983) using the formula

$$\begin{aligned} T_f \quad = \quad & \left(-5.75 \times 10^{-2}\right) S + \left(1.71 \times 10^{-3}\right) S^{1.5} + \\ & \left(-2.15 \times 10^{-4}\right) S^2 + \left(-7.53 \times 10^{-8}\right) P + 273.15, \end{aligned} \tag{16}$$

where S is the pore water salinity in psu, and P is the local hydrostatic pressure in Pascals (Pa). Since we model phase change at surface conditions, we ignore the pressure-dependency of this formula by setting $P = 0$. The salinity of the pore space is assigned, meaning there is no governing equation solved for the salinity in space and time. Salinity remains static, except for modification at the integration points exposed to ocean water (further details given below).

The quantity T_{shift} is calculated and applied to ensure that the freezing curve approaches the same, near-zero ice saturation $f = f_{\text{melt}}$ as $T \to T_f$, regardless of sediment-specific contributions. This is done to provide the freezing curve with a more physically realistic, material-independent "line-up" point at which the ice-bonded sediment is considered fully thawed. This can be approximated by solving (14) for $T = T_f$, i.e.

$$T_{\text{shift}} = -\frac{1}{G} \log\left(\frac{1}{Q}\left[\frac{D - A}{f_{\text{melt}} - A}\right]^{v_{\text{bulk}}}\right). \tag{17}$$

Lastly, a modification to the way salinity is represented from (Frederick et al., 2021) is the adjustment of salinity values to capture the effects of saline ocean water interacting with the permafrost bluff face. This is applied by assigning the permafrost pore water salinity (S) equal to the ocean salinity for elements exposed to the ocean, namely

$$S = S_{\text{ocean}}, \text{ on } \Gamma_{\text{bf}} \text{ if submerged under water.} \tag{18}$$

This changing salinity in the pore water in turn modifies the freezing temperature according to Equation (16), resulting in an enhanced melting when in contact with ocean water.

4.2.3.2 Drew Point Application With material constituents defined as a continuous function of elevation (see Figure 5), the resulting thermal model properties are also continuously varying. Hence, the distinction between the ice-bonded sediment layers and peat layer identified in Figure 4 are collapsed; however distinct properties are associated with the ice wedge. The standard latent heat of water, $334{\times}10^3\ \frac{J}{kg}$, is the only material block-agnostic constant employed, as all material blocks in the model domain may contain water.

Ice Wedge: Standard thermal properties of ice are employed (see Table 5). A small, but present, constant salinity of 1 ppt was also applied in this material block.

Ice-bonded Sediment and Peat: To develop continuously varying thermal model properties constituent values of ρ, c_p, and κ used in Equations (10, 11, 12, 13) are given in Table 4. Values of v_i used to evaluate the freezing curve in Equation (14), are selected to match the curve shapes in (M. Darrow, 2011) and additionally provided in Table 4.

Table 4. Thermal properties of ice-bonded sediment constituents. Values for ρ_i, c_{p_i}, and κ_i are guided by (Robertson, 1988),(O'Conner et al., 2020),(Gnatowski, 2016), (Boelter, 1968), (Rezanezhad et al., 2016). Values for v_i are chosen to match the curves provided in (M. M. Darrow, 2011).

constituent i	ρ_i [kg/m^3]	c_{p_i} [J/kg/K]	κ_i [W/K/m]	v_i –
Peat	250	1.9×10^3	0.08	0.1
Sand	2600	0.7×10^3	8.0	0.3
Silt	2500	0.7×10^3	4.9	0.3
Clay	2350	0.6×10^3	0.4	1.0
Ice	920	2.09×10^3	2.3	–
Water	1000	4.0×10^3	0.60	–

Combining the constituent thermal properties in Table 4 with the site specific data presented in Figure 5 results in the bulk thermal properties. Figure 9(a) shows $\overline{\rho}$ from Equation (10), Figure 9(b) shows $\overline{c_p}$ from Equation (11), and Figure 9(c) shows $\overline{\kappa}$ from Equation (12) for fully frozen ice-bonded sediment as a function of depth. The bulk density is calculated from the soil mass fractions in Equation (13) and compares well to measured core values as in Figure 9(a). Note that around 3.3 m elevation there is shift in the density as the peat content has fully disappeared and mineral constituents dominate; hence, two ice-bonded sediment material blocks are employed in the mechanical material model as shown in Figure 4 even though in the thermal material model the density is treated continuously. The specific heat capacity generally decreases as a function of depth, mostly due to decreasing contribution of ice or water to the bulk value. On the other hand, thermal conductivity generally increases with depth resulting from increasing contributions of the mineral sediments to the bulk value.

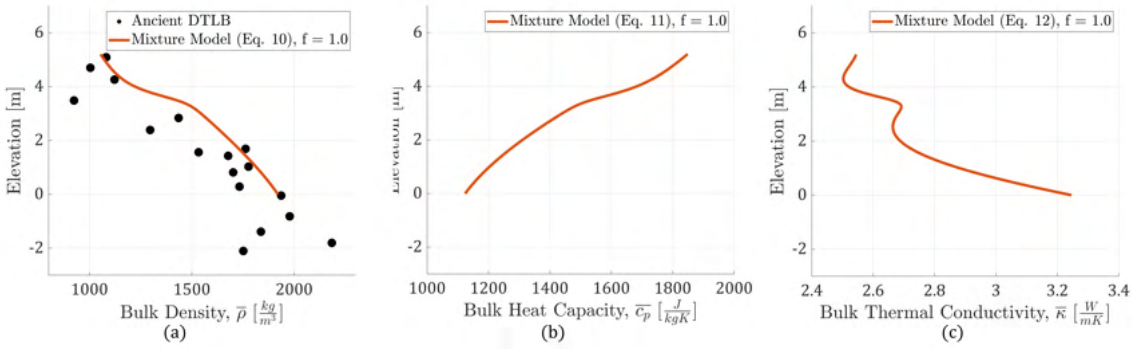

Figure 9. Fully frozen ($f = 1.0$) ice-bonded sediment bulk thermal properties as a function of elevation for an ancient drained lake basin geomorphology. The modeled bulk density, $\overline{\rho}$, is compared to measured core values (symbols) in panel (a), panel (b) shows the modeled bulk heat capacity, $\overline{c_p}$, and panel (c) shows the modeled bulk thermal conductivity, $\overline{\kappa}$.

The salinity profile shown in Figure 5(c) is applied in the calculation of the freezing/melting temperature in Equation (16). Material specific determination of ice satu-

ration (Equation (14)) is dependent upon ν_i identified in Table 4 and the freezing temperature with its ensuing dependence upon salinity. Due to the large pore size for sand and peat, we assume a narrow freezing curve width of approximately 4°C resulting in parameter values in Equation (14) being chosen to match the shapes in (M. Darrow, 2011): $A = 0.0$. $D = 1.0$, $C = 1.0$, $Q = 0.001$, $G = 10.0$. For the calculation of T_{shift} we select $f_{\text{melt}} = 0.01$ as the ice saturation "line-up point" to avoid divisions by zero in (17). The fraction of ice saturation as a function of temperature is shown for elevations 0.5 m, 2.5 m, 3.5 m, 4.0 m, and 5.0 m in this material in Figure 10. Here, the importance of the saline permafrost is clear with ∼45% of this high salinity horizon at 0.5 m elevation unfrozen even at 270 K (-3.0°C). The larger pore size horizons dominated by sand and peat (4.0 and 5.0 m) show much narrower freezing width curves.

Ocean water salinity provided by the oceanographic modeling suite is used to adjust the salinity of integration points on the bluff face Γ_{bf}. Figure 8 shows the magnitude of ocean salinity over the calibration time period; larger red symbols indicates instances in time (but not the level) when the salinity was applied on the bluff face. The water exposure history, the dark blue line in Figure 7, in conjunction with the salinity magnitude are used to apply the enhanced melting parameterization below the water exposure height according to Equation (18).

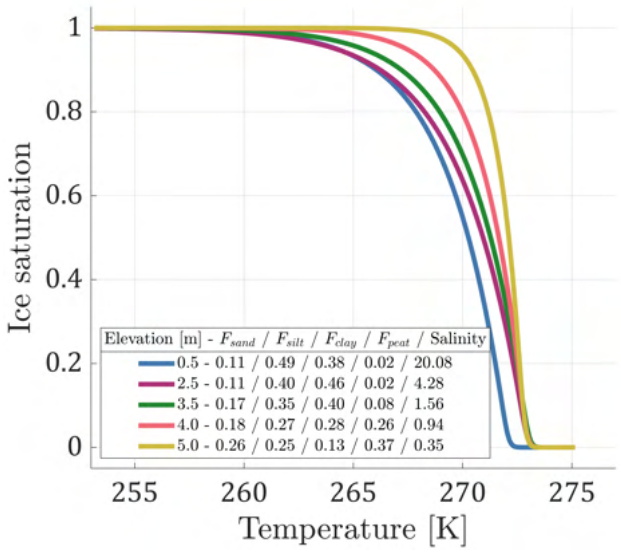

Figure 10. Example soil freezing curves used for Drew Point application, i.e. ice saturation volume fraction S_f, as a function of temperature for modeled soils in Figure 9 at different elevations (0.5 m, 2.5 m, 3.5 m, 4.0 m, and 5.0 m).

A summary of the thermal material properties implemented to represent our calibration location are given in Table 5.

Thermal problem quantities

Property	Value	Unit
General Properties		
Latent heat of water	334×10^3	J kg^{-1}
Ice Wedge Properties		
Density (ρ_{ice}) and	920	kg m^{-3}
Thermal conductivity (κ_{ice})	2.3	W K^{-1} m^{-1}
Heat capacity ($c_{p,ice}$)	2.0×10^3	J kg^{-1} K^{-1}
Salinity (S)	1	psu
Ice-bonded Sediment and Peat Layer Properties		
Bulk density ($\overline{\rho}$)	Fig. 9(a), Eq.(10)	kg m^{-3}
Bulk Thermal conductivity ($\overline{\kappa}$)	Fig. 9(b), Eq.(12)	W K^{-1} m^{-1}
Bulk Heat capacity ($\overline{c_p}$)	Fig. 9(c), Eq.(11)	J kg^{-1} K^{-1}
Porosity (θ)	Fig. 5(b)	–
Salinity (S)	Fig. 5(c)	ppt/psu
Initial condition		
Bluff temperature	Fig. 14	K
Boundary conditions		
Bluff back ($\Gamma_{\mathrm{lat,x}}$)	No heat flux	W m^{-2}
Bluff laterals ($\Gamma_{\mathrm{lat,y}}$)	No heat flux	W m^{-2}
Bluff bottom (Γ_{bot})	-0.76	W m^{-2}
Bluff face & top (Γ_{bf}, Γ_{top})	Temperatures in Fig. 8	K
Bluff face (Γ_{bf})	Salinity Fig. 8, Eq. (18)	psu

Table 5. Properties and boundary conditions for the thermal problem.

4.3 Mechanical Component

4.3.1 Governing Equations

The mechanical model defines the stresses and displacements of the modeled materials. We begin by presenting the standard finite deformation variational formulation for the solid mechanics problem, which governs the mechanical behavior of permafrost

Consider a given body represented as the regular open set $\Omega \subset \mathbb{R}^3$, undergoing motion described by the mapping $\boldsymbol{x} = \boldsymbol{\varphi}(\boldsymbol{X}, t) : \Omega \times I \to \mathbb{R}^3$, where $I := \{t \in [t_0, t_1]\}$ is a closed time interval with $0 \leq t_0 < t_1$, and $t_0, t_1 \in \mathbb{R}$. Here, $\boldsymbol{X} \in \Omega$ represents the material coordinates, and $t \in I$ is time. The initial displacement and velocity of the body at time t_0 are denoted as $\boldsymbol{x}_0 \equiv \boldsymbol{X} : \Omega \to \mathbb{R}^3$ and $\boldsymbol{v}_0 : \Omega \to \mathbb{R}^3$, respectively.

General boundary conditions are specified for either displacement (Dirichlet) or traction (Neumann). These are represented as $\boldsymbol{\chi} : \partial_{\boldsymbol{\varphi}}\Omega \times I \to \mathbb{R}^3$ and $\boldsymbol{T} : \partial_{\boldsymbol{T}}\Omega \times I \to \mathbb{R}^3$, where $\partial_{\boldsymbol{\varphi}}\Omega$ and $\partial_{\boldsymbol{T}}\Omega$ are the portions of the boundary where displacement and traction are prescribed, respectively. It is important to note that these boundaries do not overlap, i.e., $\partial_{\boldsymbol{\varphi}}\Omega \cap \partial_{\boldsymbol{T}}\Omega = \emptyset$.

Letting $\boldsymbol{F} := \nabla\boldsymbol{\varphi}$ be the deformation gradient, we can introduce the kinetic energy of the body as

$$T(\dot{\boldsymbol{\varphi}}) := \frac{1}{2}\int_\Omega \rho\dot{\boldsymbol{\varphi}}\cdot\dot{\boldsymbol{\varphi}}\ \mathrm{d}V, \tag{19}$$

and its potential energy as

$$V(\boldsymbol{\varphi}) := \int_\Omega A(\boldsymbol{F},\boldsymbol{Z})\ \mathrm{d}V - \int_\Omega \rho\boldsymbol{B}\cdot\boldsymbol{\varphi}\ \mathrm{d}V - \int_{\partial_{\boldsymbol{T}}\Omega}\boldsymbol{T}\cdot\boldsymbol{\varphi}\ \mathrm{d}S, \tag{20}$$

where $A(\boldsymbol{F},\boldsymbol{Z})$ is the Helmholtz free-energy density, $\boldsymbol{Z}$ is a collection of internal variables, ρ is the mass density in the reference configuration, and $\rho\boldsymbol{B}:\Omega\to\mathbb{R}^3$ represents the body force.

The Lagrangian function of the body is then defined as $L(\boldsymbol{\varphi},\dot{\boldsymbol{\varphi}}) := T(\dot{\boldsymbol{\varphi}}) - V(\boldsymbol{\varphi})$, which gives rise to the action functional $S[\boldsymbol{\varphi}] := \int_I L(\boldsymbol{\varphi},\dot{\boldsymbol{\varphi}})\ \mathrm{d}t$. According to the Variational Principle of Hamilton, the equation of motion is obtained by finding the critical point of the action functional $S[\boldsymbol{\varphi}]$ over the Sobolev space $W_2^1(\Omega\times I)$, which consists of all functions that are square-integrable and have square-integrable first derivatives, with fixed endpoints of the deformation mapping at t_0 and t_1 (Marsden & Ratiu, 1999).

We define

$$\mathcal{S} := \left\{\boldsymbol{\varphi}\in W_2^1(\Omega\times I) : \boldsymbol{\varphi}=\boldsymbol{\chi} \text{ on } \partial_{\boldsymbol{\varphi}}\Omega\times I; \boldsymbol{\varphi}=\boldsymbol{x}_0 \text{ on } \Omega\times t_0; \boldsymbol{\varphi}=\boldsymbol{x}_1 \text{ on } \Omega\times t_1\right\} \tag{21}$$

and

$$\mathcal{V} := \left\{\boldsymbol{\xi}\in W_2^1(\Omega\times I) : \boldsymbol{\xi}=\boldsymbol{0} \text{ on } \partial_{\boldsymbol{\varphi}}\Omega\times I\cup\Omega\times t_0\cup\Omega\times t_1\right\}, \tag{22}$$

where $\boldsymbol{\xi}$ is a test function. This leads to

$$\delta S := DS[\boldsymbol{\varphi}](\boldsymbol{\xi}) = \int_I\left[\int_\Omega(\nabla\cdot\boldsymbol{P}+\rho\boldsymbol{B}-\rho\ddot{\boldsymbol{\varphi}})\cdot\boldsymbol{\xi}\ \mathrm{d}V + \int_{\partial_{\boldsymbol{T}}\Omega}\boldsymbol{T}\cdot\boldsymbol{\xi}\ \mathrm{d}S\right]\ \mathrm{d}t = 0, \tag{23}$$

where $\boldsymbol{P} = \partial A/\partial\boldsymbol{F}$ denotes the first Piola-Kirchhoff stress. The Euler-Lagrange equation corresponding to (23) is

$$\nabla\cdot\boldsymbol{P}+\rho\boldsymbol{B} = \rho\ddot{\boldsymbol{\varphi}} \quad \text{in} \quad \Omega\times I. \tag{24}$$

The variational statement in Equation (23) is implemented using a standard finite element discretization in space (Hughes, 1987), with isoparametric elements, and an implicit Newmark integrator for time integration (Newmark, 1959).

4.3.2 Initial and Boundary Conditions

4.3.2.1 General Initial conditions for the displacement and velocity in the Euler-Lagrange equation (24) are given by

$$\boldsymbol{\varphi}(\boldsymbol{X},t_0) = \boldsymbol{x}_0,\ \ \dot{\boldsymbol{\varphi}}(\boldsymbol{X},t_0) = \boldsymbol{v}_0 \text{ in } \Omega, \tag{25}$$

while the displacement (Dirichlet) and traction (Neumann) boundary conditions are respectively given by

$$\boldsymbol{\varphi}(\boldsymbol{X},t) = \boldsymbol{\chi} \text{ on } \partial_{\boldsymbol{\varphi}}\Omega\times I,\ \ \boldsymbol{PN} = \boldsymbol{T} \text{ on } \partial_{\boldsymbol{T}}\Omega\times I. \tag{26}$$

Here, $\partial_{\boldsymbol{\varphi}}\Omega\times I$ and $\partial_{\boldsymbol{T}}\Omega\times I$ represent the domain boundaries along which displacement (former) or traction (latter) are prescribed.

A key advancement in our model compared to the original ACE model (Frederick et al., 2021) is the inclusion of a time-varying wave pressure boundary condition in the

mechanics formulation, Equation (24). To our knowledge, this is the first instance of accounting for the mechanical action of wave forces on Arctic coastal erosion. This additional Neumann boundary condition is applied on the bluff face boundary Γ_{bf} and captures the pressure exerted by the ocean in contact with the bluff face. This pressure is dictated by the water exposure history which is most appropriately represented by a time-varying hydrostatic pressure due to the large simulation time step. Specifically, we set the pressure at the bluff face to

$$p(t) = \rho_o g w_{\text{terr}}(t). \tag{27}$$

Here, g, ρ_o, and $w_{\text{terr}}(t)$ denote the acceleration due to gravity, the ocean water density ($\rho_o = 1022$ kg/m^3), and the water exposure history, respectively, as defined in Section 3.1.

We note that more advanced wave pressure formulations accounting for wave-induced pressures from orbital velocities within the waves (see Chapter 5 of (Holthuijsen, 2007) for linear wave theory, though nonlinear wave theory is more applicable in these shallow depths) or breaking waves (see (Partenscky, 1988)) could be considered. However, such formulations would require fine temporal resolutions to remain physically meaningful.

4.3.2.2 Drew Point Application Initially, there is no displacement or movement in any of the modeled materials, i.e., $\boldsymbol{x}_0 = 0$ and $\boldsymbol{v}_0 = 0$. Symmetry boundary conditions are applied on the lateral and bottom boundaries: $\Gamma_{\text{lat,x}}$, $\Gamma_{\text{lat,y}}$, and Γ_{bot}. Specifically, zero displacement in the x-direction is prescribed on $\Gamma_{\text{lat,x}}$, zero displacement in the y-direction is prescribed on $\Gamma_{\text{lat,y}}$, and zero displacement in the z-direction is prescribed on Γ_{bot}. On the top boundary of the bluff, Γ_{top}, a simple zero traction boundary condition is applied.

In Equation (27), $w_{\text{terr}}(t)$ is shown in Figure 7. For all grid cells exposed to the ocean at a given time, the elevation of each grid cell is multiplied by $g\rho_o$ to calculate the time-varying hydrostatic pressure applied by the ocean for the simulation time step. Consequently, the hydrostatic pressure is vertically resolved for each time step.

A summary of the initial and boundary conditions implemented in this study is provided in Table 6.

4.3.3 Material Model

4.3.3.1 General As detailed in (Frederick et al., 2021), we employ a standard J_2 plasticity model extended to account for large deformations to simulate the mechanical behavior of permafrost. While this model is fully capable of capturing plastic deformation, in this work, we limit its description to the elastic regime. This assumption aligns with the erosion framework, which removes elements upon reaching the yield stress, bypassing the plastic deformation regime (further discussed in Section 4.3.4).

We choose this modeling approach for several reasons. Firstly, the scale of our application is sufficiently large to justify the use of an isotropic material model, which adequately represents the microstructural characteristics of ice, and by extension for ice-bonded sediments in permafrost. Secondly, the model requires minimal calibration and integrates seamlessly with the Albany LCM codebase, which houses our erosion framework (Frederick et al., 2021).

For details on the full material modeling framework, including the formulation for plastic deformation regimes, the reader is referred to Appendix A of (Frederick et al., 2021). In this study, we adapt the mechanical material model for the purely elastic regime by incorporating dependence on porosity.

The thermo-mechanical response of the solids considered here is characterized by a free-energy density per unit undeformed volume of the form

$$A = A(\boldsymbol{F}, f, \theta),$$

where $\boldsymbol{F}$ is the deformation gradient, f is the ice saturation, and θ is the porosity (Lee, 1969). The mechanical response's dependence on the thermal state is assumed to be captured through variations in ice saturation.

We assume that the free-energy density A has the form

$$A(\boldsymbol{F}, f, \theta) = W^{\mathrm{e}}(\boldsymbol{F}^{\mathrm{e}}, f, \theta) \tag{28}$$

where $W^{\mathrm{e}}(\boldsymbol{F}^{\mathrm{e}}, f, \theta)$ is the elastic energy density per unit undeformed volume.

A simple form of the resulting elastic energy is

$$\begin{aligned} W^{\mathrm{e}}(\boldsymbol{\epsilon}^{\mathrm{e}}, f, \theta) &= W^{\mathrm{e,vol}}(\vartheta^{\mathrm{e}}, f, \theta) + W^{\mathrm{e,dev}}(\boldsymbol{\epsilon}^{\mathrm{e}}, f, \theta), \\ W^{\mathrm{e,vol}}(\vartheta^{\mathrm{e}}, f, \theta) &= \frac{k(f,\theta)}{2}(\vartheta^{\mathrm{e}})^2, \\ W^{\mathrm{e,dev}}(\boldsymbol{\epsilon}^{\mathrm{e}}, f, \theta) &= \mu(f,\theta)||\mathrm{dev}(\boldsymbol{\epsilon}^{\mathrm{e}})||^2, \end{aligned} \tag{29}$$

where $\boldsymbol{\epsilon}^{\mathrm{e}} := \frac{1}{2}\log(\boldsymbol{F}^{\mathrm{eT}}\boldsymbol{F}^{\mathrm{e}})$, $\vartheta^{\mathrm{e}} = \log J^{\mathrm{e}}$, and $J^{\mathrm{e}} := \det(\boldsymbol{F}^{\mathrm{e}})$. In this framework, the yield stress $Y(f,\theta)$, bulk modulus $k(f,\theta)$ and the shear modulus $\mu(f,\theta)$ are assumed to depend on the ice saturation and the porosity. For the bulk and shear moduli, this dependence is introduced to the elastic modulus $E(f,\theta)$, but not to the Poisson's ratio ν, as

$$k(f,\theta) = \frac{E(f,\theta)}{3(1-2\nu)}, \quad \mu(f,\theta) = \frac{E(f,\theta)}{2(1+\nu)}. \tag{30}$$

From these expressions the Cauchy stress can be computed as

$$\boldsymbol{\sigma} := \boldsymbol{\sigma}^{\mathrm{vol}} + \boldsymbol{\sigma}^{\mathrm{dev}}, \tag{31}$$

in which the volumetric component of the Cauchy stress is

$$\boldsymbol{\sigma}^{\mathrm{vol}} := k(f,\theta)\mathrm{vol}(\boldsymbol{\epsilon}^{\mathrm{e}}), \tag{32}$$

and the corresponding deviatoric component of the Cauchy stress as

$$\boldsymbol{\sigma}^{\mathrm{dev}} := \frac{2\mu(f,\theta)}{J^e}\boldsymbol{F}^{\mathrm{e},-\mathrm{T}}\mathrm{dev}(\boldsymbol{\epsilon}^{\mathrm{e}})\boldsymbol{F}^{\mathrm{e,T}}, \tag{33}$$

and where $\mathrm{vol}(\bullet) := \frac{1}{3}\mathrm{tr}(\bullet)\boldsymbol{I}$ and $\mathrm{dev}(\bullet) := (\bullet) - \mathrm{vol}(\bullet)$.

A measure of the shear stress in the material can be expressed as

$$s(f,\theta) := 2\mu(f,\theta)||\mathrm{dev}(\boldsymbol{\epsilon}^{\mathrm{e}})||, \tag{34}$$

and a simple yield stress function for perfect elasto-plastic material can be formulated simply as

$$Y_{\mathrm{eff}}(f,\theta) := \sqrt{\frac{2}{3}}Y(f,\theta). \tag{35}$$

A key development in the material model, with significant implications for the novel erosion criterion introduced in Section 4.3.4, involves considering the extent of shear deformation that the material can undergo before being classified as eroded. This development also addresses how shear deformation interacts with variations in the elastic modulus.

As ground-ice melts within ice-bonded sediments, it generates a slurry composed of low ice saturation, water, and sediment. This slurry undergoes denudation through a sloughing process, characterized by material stretching in both tension and shear. While the previous version of the ACE model (Frederick et al., 2021) captured thermo-denudation through tensile and compressive yield criteria, it did not account for shear deformation in the assessment of material erosion. In this approach, we extend the model to include the role of shear deformation in material failure.

Shear deformation is quantified using the deviatoric right Cauchy-Green deformation tensor, defined as

$$\gamma = \frac{||J^{-\frac{2}{3}}\boldsymbol{F}^{\mathrm{T}}\boldsymbol{F}||}{\sqrt{3}} \tag{36}$$

where J and $\boldsymbol{F}$ are defined through Equation (29).

This deviatoric strain, referred to simply as strain, reflects shear deformation when its values deviate from one. An erosion criterion is then introduced to impose a threshold on the amount of strain the material can experience before it is considered eroded. This strain limit can be defined as continuously varying throughout the material, which presents the opportunity to introduce a functional dependence on desired material properties/composition. For example, from field observations, it is clear that intact plant material, such as roots and fibers, within the peat significantly increase the degree of strain before failure (see the vegetative mat in Figure 1(a)). These structures allow the material to extend and contract through relative motion between fibers, which holds the natural material together and delays failure. Hence, we have chosen to define the strain tolerance (detailed further in Section 4.3.4) to depend on peat mass fraction, which may serve as an analog for the presence of vegetation and root structures.

In conjunction with the consideration of shear deformation, allowing the elastic modulus (and, by extension, the bulk and shear moduli) to vary with f and θ enables the model to capture the changing mechanical behavior of ice-bonded sediment as it thaws. As shown in Figure 6, the elastic modulus decreases significantly in regions of low ice saturation, eventually reaching the minimum allowable elastic modulus value, E_{m}. This results in ice-bonded sediment material becoming increasingly compliant, experiencing larger deformations under a given stress, and ultimately leading to greater material failure as governed by the strain tolerance when approaching a more thawed state.

Building on the concept of deformation described above, niche development is modeled in the context of accelerated deformation. When ocean water interacts with the terrestrial environment, ice-bonded sediment transitions into an unconsolidated slurry, which eventually dissolves into the ocean. In the limit, this process can be interpreted as significant deformation of the ice-bonded sediment.

To represent this transition, the material in contact with ocean water is assigned a distinct and lowered minimum allowable elastic modulus, $E_{\mathrm{m,o}}$, reflecting the slurry-like state where much larger shear deformations occur under a given applied stress. This approach effectively captures the dissolution of thawed ice-bonded sediment into ocean water, leading to niche formation. This conditional assignment of material properties is applied at each time step based on ocean wave exposure, as discussed in Section 3.2.

A final important modification introduced in this study to the standard J_2 plasticity model is the asymmetric treatment of the yield stress, $Y(f, \theta)$, under compression and tension. While the conventional J_2 plasticity model assumes equal tensile and compressive yield stresses, more advanced geotechnical models capture the inherent asymmetry between these behaviors. Since ice, and by assumption, ice-bonded sediment, exhibits such asymmetric yield characteristics (see (Petrovic, 2003) or Figure 6(b-c)), we

implemented a distinct tensile yield strength to avoid the complexity of more intricate material models. As a result, while the material's stress-strain response remains symmetric, the yield stresses in compression and tension are distinct. This adjustment enables the formation of tensile cracks in frozen permafrost regions, as demonstrated in (Thomas et al., 2020).

In summary, the material model incorporates three essential concepts: (1) the dependence of the elastic modulus and yield strength on ice saturation and porosity, (2) accelerated deformation to capture niche development through a distinctly lowered minimum allowable elastic modulus for ocean-contacted material, and (3) the asymmetry in compressive and tensile yield strength. These three aspects of the mechanical model are critical for governing the distinct erosion processes that the ACE model captures: thermo-denudation and thermo-abrasion, including appropriate niche formation and subsequent block collapse. Given the challenges in characterizing the mechanical properties of ice-bonded sediment, these components of the material model require careful tuning, with parameter selection forming the focus of the calibration study.

4.3.3.2 Drew Point Application The mechanical model defines some of its material properties (i.e. density) by distinct material blocks, and hence multiple material blocks are defined within the computational domain as shown in Figure 4. Each block can possess distinct densities, material properties, and failure criteria. Table 6 lists the material constants used in the ACE model simulations and summarizes all material properties employed in the calibrated results.

Ice Wedge: The ice wedge is assigned standard values for density (920 kg/m^3) and a constant elastic modulus (10 GPa), as reported in (Petrovic, 2003). A constant Poisson ratio of 0.3 is used, consistent with values found in the literature (Petrovic, 2003).

Ice-bonded Sediment: Two ice-bonded sediment blocks are defined with distinct average densities to better capture the variation observed in Figure 9(a). The top block $\overline{\rho_1}$ (1239 kg m^{-3}) is obtained from the mean value of densities in Figure 9(a) between $3.3 < z \leq 4.7$. The bottom block $\overline{\rho_2}$ (1733 kg m^{-3}) is obtained from the mean value of densities in Figure 9(a) between $0.0 < z \leq 3.3$. The elastic modulus, $E(f, \theta)$, varies continuously throughout the domain and is defined according to the surface shown in Figure 6(a). For the minimum allowable elastic modulus (lilac plane in Figure 6(a)), two calibrated parameters are introduced: one specific to ocean contact and the other general, both of which are explored in Section 5. A constant Poisson ratio of 0.21 is employed, supported by prior experimentation (D. L. Bull et al., 2020).

Peat: The peat block is mechanically distinct from the ice-bonded sediment block to account for the effects of root structures, which form a matted matrix in the peat layer. Observationally, it is common to see an overhanging vegetative mat of peat, as depicted in Figure 1(a). This block is assigned an average density, $\overline{\rho}$, of 958 kg/m^3, derived from the mean value of densities in Figure 9(a) between $4.7 < z \leq 5.2$. The elastic modulus, $E(f, \theta)$, for peat is the same as that of ice-bonded sediment (shown in Figure 6(b)). However, to better capture the mat's ability to droop significantly without breaking, a higher minimum elastic modulus, E_{m}, of 1×10^5 Pa is assigned. A constant Poisson ratio of 0.21 is used, supported by prior experimentation (D. L. Bull et al., 2020).

Mechanical problem quantities

Property	Value	Unit
Ice Wedge Properties		
Bulk density ($\overline{\rho_{ice}}$)	920	kg m^{-3}
Elastic modulus (E_{ice})	10×10^9	Pa
Poisson's ratio (ν)	0.30	–
Ice-bonded Sediment Properties		
Top layer bulk density ($\overline{\rho_{p1}}$)	1239	kg m^{-3}
Bottom layer bulk density ($\overline{\rho_{p2}}$)	1733	kg m^{-3}
Poisson's ratio (ν)	0.21	–
Elastic modulus ($E(f, \theta)$)	Fig. 6	Pa
Minimum allowable elastic modulus (E_{m})	$1.1{\times}10^{4*}$	Pa
Minimum allowable elastic modulus in contact with ocean ($E_{\mathrm{m,o}}$)	220^*	Pa
Peat Layer Properties		
Bulk density ($\overline{\rho_v}$)	958	kg m^{-3}
Poisson's ratio (ν)	0.21	–
Elastic modulus ($E(f, \theta)$)	Fig. 6	Pa
Minimum allowable elastic modulus (E_{m})	1×10^5	Pa
Boundary conditions		
Bluff back & bottom ($\Gamma_{\mathrm{lat,x}}$, Γ_{bot})	Zero displacement	m
Bluff laterals ($\Gamma_{\mathrm{lat,y}}$)	Zero displacement	m
Bluff top (Γ_{top})	Zero traction	Pa
Bluff face (Γ_{bf})	Eq. (27) and zero traction	Pa

Table 6. Properties and boundary conditions for the mechanical problem. Calibrated parameters are denoted with asterisks*, as discussed in Section 5.2.

4.3.4 Mesh Erosion

4.3.4.1 General A unique feature of the terrestrial component of the ACE model is its ability to remove mesh elements based on topology manipulation according to a series of failure criteria, referred to as "mesh erosion." During each timestep, failure criteria are evaluated at all 8 integration points within each element. Integration points that meet the failure criteria are marked as failed. Proper topological representation of the mesh to enable mesh element removal is essential for this process. As described in (Frederick et al., 2021), a graph representation for simplicial elements is adopted, which can be extended to non-simplicial topologies (Mota et al., 2008).

Many of the advances in the representation of material model, discussed in Section 4.3.3, have been made to better represent erosion, and hence the criteria by which failure and element removal are assessed. In the terrestrial ACE model, there are three main classes of failure: 1) when the ice saturation is low, 2) when the ice saturation is high, and 3) to preserve numerical solver stability. Each class of failure employs distinct criteria to evaluate element removal (presented respectively to prior list): 1) strain and stress criteria, 2) stress criteria, and 3) kinematic criteria. Two new failure criteria—strain and

tensile yield stress—are introduced here in addition to those presented in (Frederick et al., 2021). All criteria are summarized below.

Strain criterion. This criterion addresses situations where the material is weak enough to deform significantly under low stress. It is defined as $\gamma > \gamma_{\text{tol}}$, where $\boldsymbol{\gamma}$ is given by (36), and γ_{tol} is a strain limit which will be represented as a function of F_{peat}. This criterion specifically targets shear or deviatoric deformation, which is not fully captured by the other criteria. For this work, the relationship $\gamma_{\text{tol}} \sim 1.0 + F_{\text{peat}}$ was chosen as the simplest form to reflect this behavior. For example, in the peat layer (where $F_{\text{peat}} \sim 40\%$), the material can stretch approximately 10 times more than mineral soil (where $F_{\text{peat}} \sim 3.5\%$) before failing. The minimum distortion tolerance, $\gamma_{\text{tol}} = 1.04$, corresponds to a material distortion of 4% of its original length before erosion in soils devoid of peat. As this criterion targets material experiencing larger deformations, it is more likely to act on material with a low elastic modulus (i.e. more compliant material).

Compressive yield criterion. This criterion assumes that failure occurs when the shear stress in the material, $s(f, \theta)$ (given by Equation (34)), reaches the effective yield stress $Y_{\text{eff}}(f, \theta)$ (given by Equation (35)). Thus, integration points in the mesh for which $s > Y_{\text{eff}}$ are marked for failure. Note here that the effective yield stress is dependent on the yield strength function developed in Section 2.1.2 and shown in Figure 6(b), with corresponding minimum allowable value Y_{m}, which is calibrated.

Tensile yield criterion. Given that most geomaterials, such as ice-bonded sediment and ice, are weaker in tension, this criterion accounts for failure under tensile stress. This criterion assumes that for material in tension, failure occurs when $\max\left((\text{eig}\,\boldsymbol{\sigma})\right) > \sigma_{\text{tol}}$, where $\boldsymbol{\sigma}$ is the Cauchy stress given by (31), and σ_{tol} is a tensile stress tolerance. In this case, σ_{tol} is shown by as the upper plane Figure in 6(c). It is worth noting that material in tension may also fail in cases where $s > Y_{\text{eff}}$ but $\max\left((\text{eig}\,\boldsymbol{\sigma})\right) < \sigma_{\text{tol}}$; the presence of σ_{tol} simply imposes an upper limit on the yield stress that is distinct in tension to capture this material weakening in tension. This concept is illustrated in Section 2.1.2, Figure 6(c), where the yield surface derived for compression and minimum compressive allowable yield Y_{m} (lower lilac plane) are shown alongside the the tensile stress tolerance σ_{tol} (upper lilac plane).

Angle criterion. This criterion removes elements from the mesh when their tilt exceeds a specified angle. It is defined as $|\cos^{-1}\left[\frac{1}{2}(\text{tr}\boldsymbol{R} - 1)\right]| > \phi_{\text{tol}}$, where $\boldsymbol{R}$ is the rotation tensor obtained from the polar decomposition of the deformation gradient $\boldsymbol{F}$, and ϕ_{tol} is a tilt angle tolerance.

Displacement criterion. This criterion removes elements based on excessive displacement. It is defined as $|\boldsymbol{u}| > u_{\text{tol}}$, where $\boldsymbol{u}$ is the displacement vector at a material point, and u_{tol} is a displacement tolerance.

4.3.4.2 Drew Point Application For all materials, failure occurs only when all 8 integration points of a hexahedral element surpass the specified thresholds summarized in Table 7. Additionally, the following kinematic criteria are applied regardless of material: a tilt angle tolerance, $\phi_{\text{tol}} > 1.4$ rad, and a displacement tolerance, $u_{\text{tol}} > 0.35$ m, will result in failure. These criteria help maintain numerical solver stability when elements tilt or displace excessively, often due to the removal of neighboring elements by the strain and yield criteria. As shown in (D. L. Bull et al., 2020), observations of tilt indicate angles of 0.2 rad can be sustained for long periods. Hence, since the main design of these criteria is numerical solver stability, conservative tolerances are chosen.

Ice Wedge: Failure criteria for the ice wedge are based on standard values in the literature. Compressive stresses exceeding $Y_{\text{eff},ice} > 5$ MPa and tensile stresses exceeding $\sigma_{\text{tol},ice} > 1.43$ MPa will result in failure (Petrovic, 2003). The strain criterion is not applied to the ice wedge due to the high elastic modulus, E_{ice}, assigned to the material.

Ice-bonded Sediment and Peat: Experimental investigation, described in Section 2.1.2, was required to establish the material behavior controlling the failure criteria for ice-bonded sediments. However, these experimental investigations revealed that capturing the mechanical behavior, especially at low ice saturation and/or porosity, could be very difficult. Hence, many of the tolerances which dictate failure require calibration as detailed in Section 5.2. To succinctly summarize all criteria, we present calibration values obtained in Section 5.2 here. The yield strength, $Y_{tol}(f, \theta)$, is shown in Figure 6(a), while the minimum allowable compressive yield value, Y_{m}, was calibrated to be 5.0×10^6 Pa. The tensile stress tolerance, σ_{tol}, was informed by measured values in Figure 6(c), and was calibrated to be $1.4{\times}10^5$ Pa. The strain limit is defined as $\gamma_{\mathrm{tol}} = \max(1.04, 1.0 + F_{\mathrm{peat}})$, where F_{peat} represents the fraction of peat in the sediment mixture. For example, in the peat layer (where $F_{\mathrm{peat}} \sim 40\%$), the material can stretch approximately 10 times more than mineral soil (where $F_{\mathrm{peat}} \sim 3.5\%$) before failing. The minimum distortion tolerance, $\gamma_{\mathrm{tol}} = 1.04$, corresponds to a material distortion of 4% of its original length before erosion in soils devoid of peat.

Erosion criteria related quantities

Property	Value	Unit
Consistent across material		
Angle of rotation (ϕ_{tol})	1.40	radians
Displacement (u_{tol})	0.35	m
Number of failed nodes	8	–
Ice Wedge		
Compressive yield stress (Y_{ice})	5.0×10^6	Pa
Tensile yield stress ($\sigma_{\mathrm{tol},ice}$)	1.43×10^6	Pa
Strain	N/A	
Ice-bonded Sediment and Peat		
Compressive yield stress ($Y(f, \theta)$)	Fig. 6(a), with $Y_{\mathrm{m}} = 5 \times 10^{4*}$	Pa
Tensile yield stress (σ_{tol})	$1.4 \times 10^{5*}$	Pa
Strain (γ_{tol})	max(1.04, 1+F_{peat})	–

Table 7. Erosion criteria properties utilized. Calibrated parameters are denoted with asterisks*, and are described further in Section 5.2.

4.4 Sequential thermo-mechanical coupling

4.4.1 General

The coupling between the thermal and mechanical PDEs defining the ACE terrestrial model is performed on a time-step by time-step basis via a sequential coupling algorithm modeled after the existing iterative alternating Schwarz-based coupling framework available in `Albany-LCM` (Mota et al., 2017, 2020).

In general, the coupling approach is represented in Figure 2 and is described more fully below. For a given time k, timestep Δt_k, and bluff geometry Ω_k, the thermal step is solved first for temperature and ice saturation fields T_{k+1} and f_{k+1}, which are provided to the mechanical step to update material models dependent on ice saturation. Next, the mechanical step solves for the material stresses, displacements, and any occurring ero-

sion, yielding the (potential) new geometry Ω_{k+1} which is provided to the subsequent thermal step. We emphasize that there is no direct dependence between the thermal and mechanical PDEs; instead, the dependence/coupling happens implicitly through the relevant material models and the evolving mesh geometry.

Given that mechanical failure, like the block failure shown in Figure 1(d), can occur on vastly different time scales (e.g., fractions of a second) compared with the thermal problem dynamics (e.g. tens of minutes to hours), the coupling method also features an adaptive time stepping, which is central to enabling the capture of both primary modes of erosion – denudation and block failure. The adaptive time stepping algorithm is triggered for timesteps where a given step is deemed unsuccessful – typically, when the mechanical solver has not converged (due to fast-moving dynamics that are not temporally resolved appropriately). If a thermo-mechanical solve is unsuccessful, the time-step Δt_k is reduced by a given reduction factor r_f (where $0 \leq r_f \leq 1$) and the solution process is repeated without updating the geometry until a successful solve is achieved. In contrast, if a given solve is successful, the time-step is incremented based on the previous time-step multiplied an the amplification factor a_f (where $a_f > 1$), but not allowed to surpass a maximum allowable timestep $\Delta t_{\max}$ (which is predominantly the governing timestep for a simulation). The time-step amplification serves to regain a generally desired time-step value once the simulation has stabilized after a period of required time-step reductions. The coupling algorithm and time-step adaptation logic is outlined in Algorithm 1.

Algorithm 1: Sequential thermo-mechanical coupling algorithm with adaptive time-stepping.
Let us denote the following: Ω_0 as the initial domain on which the problem is solved; Δt_0 the initial timestep, $\Delta t_{\min}$ the minimum allowable timestep, $\Delta t_{\max}$ the maximum allowable timestep (and the predominantly used timestep throughout the simulation) t_0 and t_{final} as the initial and final simulation times; $r_f \in [0, 1]$ as the "reduction factor" for the time-step adaptation; $a_f \geq 1$ as the "amplification factor" for the time-step adaptation.

Given: Δt_0, t_{final}, t_0, $\Delta t_{\min}$, $\Delta t_{\max}$, r_f, a_f, Ω_0;
Set $k = 0$;
while *time* $t_k < t_{final}$ **do**
  Set $t_{k+1} = t_k + \Delta t_k$;
  Advance thermal problem in Ω_k from t_k to t_{k+1}, extract ice saturation, $f_{k+1}(T_{k+1})$;
  Advance mechanical problem in Ω_k from time t_k to t_{k+1} with updated material models based on ice saturation $f_{k+1}(T_{k+1})$, which will produce (possibly new eroded) geometry $\tilde{\Omega}_{k+1}$;
  if *time advancements are successful* **then**
    Set $\Delta t_{k+1} = \min(a_f \Delta t_k, \Delta t_{\max})$, $k = k + 1$, $\Omega_k = \tilde{\Omega}$;
  else
    Set $\Delta t_k = \max(r_f \Delta t_k, \Delta t_{\min})$;
  end
end

Thanks to the modular design of `Albany-LCM`, users can select from a variety of time-integration methods available within the `Piro` and `Tempus` packages of `Trilinos` for advancing the semi-discretized model forward in time. Our coupling algorithm does not specify which time-integration scheme must be used to advance the thermal and mechanical problems. This enables us to advance the thermal problem explicitly with Forward Euler and the mechanical problem implicitly with the standard trapezoial rule Newmark (Newmark, 1959) scheme (Newmark parameters: $\beta = 0.25$, $\gamma = 0.5$). It turns

out that this feature is critical to good computational performance of the coupled model; additional disadvantages of employing a monolithic solve are detailed in (Frederick et al., 2021).

4.4.2 Drew Point Application

The general timestep utilized (corresponding to $\Delta t_{\max}$) for the presented calibration simulations is 900 seconds (or 15 minutes). For the time-step adaptation, we utilize a minimum allowable timestep $\Delta t_{\min} = 1 \times 10^{-6}$, a reduction factor $r_f = 0.5$, and an amplification factor $a_f = 1.2$. In the calibrated simulation case, timestep reduction is utilized for $1,530$ out of the $11,074$ total simulated timesteps (roughly 15% of the steps); i.e. the 900 second timestep is utilized for $\sim 85\%$ of the steps.

5 ACE Model Calibration

For the presented work, the ACE model calibration is focused on four parameters related to mechanical material properties of the modeled ice-bonded sediment. The parameters, first introduced in Section 2.1.2 and described further in Section 4.3.3, are the minimum allowable compressive yield strength Y_{m}, the minimum allowable elastic moduli (general and ocean-contacted) E_{m} and $E_{\mathrm{m,o}}$, and the tensile yield strength σ_{tol}. In particular, the goal of the calibration is to (1) understand the impact of these parameters on erosion behavior and (2) identify appropriate values to capture the distinct mechanisms of erosion were observed at Drew Point during the 2018 field campaign (D. L. Bull et al., 2020; Ward Jones et al., To be Submitted).

As a result, this section is organized as follows. First, Section 5.1 describes the bluff face erosion and niche formation measurements taken in the field study which are used to establish "target erosion behavior" to capture for model calibration. Section 5.2 outlines the simulation studies conducted to determine calibrated values for each of the parameters outlined above, and discusses the influence these parameters have on modeled erosion behavior. Lastly, Section 5.3 explores simulation results from the calibrated model, assesses model performance compared with observational data, and draws insights regarding erosion failure mechanisms used in the model.

5.1 Calibration Observations

5.1.1 Bluff Face Erosion Measurements

Bluff face erosion measurements were collected through four repeat AUV surveys as well as from daily-resolved time-lapse calibrated images. These measurements are most representative of the changes experienced at the top of the bluff. Both measurements are employed in the calibration and are described below.

A quad-rotor phantom AUV acquired repeat images along a 1.5 km stretch of coastline (highlighted as a dashed yellow line in Figure 3) on Jul. 25, Jul. 30, Aug. 04, and after block collapse on Sept. 30 2018 (note, all dates and times are presented in Greenwich Mean Time (GMT)). Images were processed into orthomosaics and digital surface models (DSM) using Pix4d software that relied upon 24 ground control points established with Leica differential GPS as described in detail in (Ward Jones et al., To be Submitted). We further processed the data into products that represented the bluff edge in order to determine erosion rates using the USGS DSAS tool (Himmelstoss et al., 2018). We extracted the bluff edge using a 100% change in slope based on the DSM data and this vector file was manually corrected to account for any noise evident in the nearshore setting. Figure 11 shows the generated shoreline near the calibration site for each AUV measurement during the summer of 2018. Changes in the location of the bluff edge were used to calculate erosion rates and differentiate between erosion types (block failure vs. de-

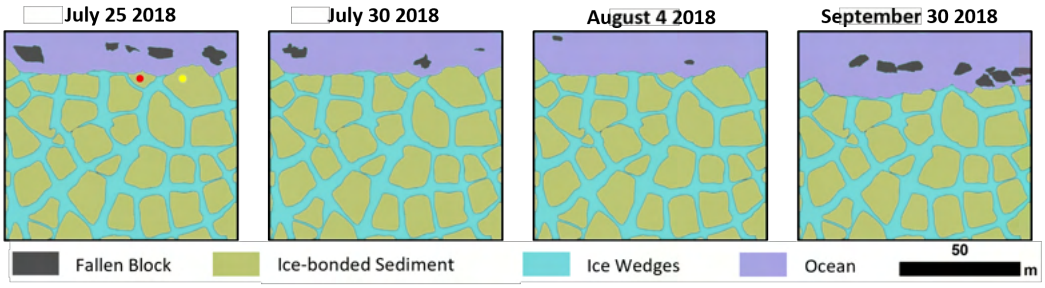

Figure 11. A series of processed images after bluff edge extraction for a portion of the 1.5 km stretch of Drew Point coastline acquired by AUV. The locations of the vertical thermistor (red) and time lapse camera (yellow) are shown by the colored dots in the first panel. As identified by the camera, bluff collapse at the thermistor location occurred on Sept. 1 2018.

nudation) as aggregated over the 1.5 km stretch in (Ward Jones et al., To be Submitted).

Twelve transect lines intersect with the calibration polygon with the red dot in Figure 11, providing a spread in erosional measurements. The average values of erosion between Jul. 25 to Jul. 30 and Jul. 30 to Aug. 4 were 0.28 ±0.22 m and 0.27 ±0.22 m respectively. However, these average values encompass a wide variability as the standard deviations show. Thermo-denudation data from each transect line is presented in Figure 12 as a scatter of points on each day. No individual transect will be selected as most representative, but the entire range will be used for calibration. The last survey on Sept. 30 reveals a total erosional average of 5.82 ±2.13 m since Jul. 25; although some denudation likely occurred between Sept. 1 and Sept. 30, this can be mostly attributed to the block failure.

A time-lapse camera (Buckeye cam x80 model) was installed in April in the center of the permafrost polygon neighboring the polygon with a vertical thermistor probe (see the yellow dot in Figure 11). Figure 13 presents photographs of and from the time lapse camera at the calibration site. It was configured to take hourly photos and documents the polygon with the vertical thermistor breaking along an ice wedge between Aug. 31 and Sept. 1 2018 (Figure 13). Photographs from this camera were analyzed using reference distances to create a daily record of bluff top erosion. Daily amounts of thermo-denudation between Jul. 1 and Aug. 31 from this analysis is presented in Figure 12 as a black dashed line. As established by the camera, on Sept. 1 the block has collapsed with a corresponding total erosion distance of 5.55 m since Jul. 25.

Comparison of the thermo-denudation measurements in Figure 12 show that the camera measurement underestimates the high resolution AUV measurements for the majority of the transects. However, there are at least 4 of the transects (four markers in Figure 12) for which the AUV and camera measurements are in concert. Additionally, the overall magnitude of erosion (estimated as 5.55 m from camera between Jul. 25 and Sept. 1 and 5.82 m from AUV between Jul. 25 and Sept. 30) are also in unison.

This analysis sufficiently constrains the daily resolution erosion values from the camera such that it can serve as the basis for the denudation comparisons. The AUV measurements and total erosion estimates indicate that slightly more aggressive denudation values may be acceptable and potentially more valid.

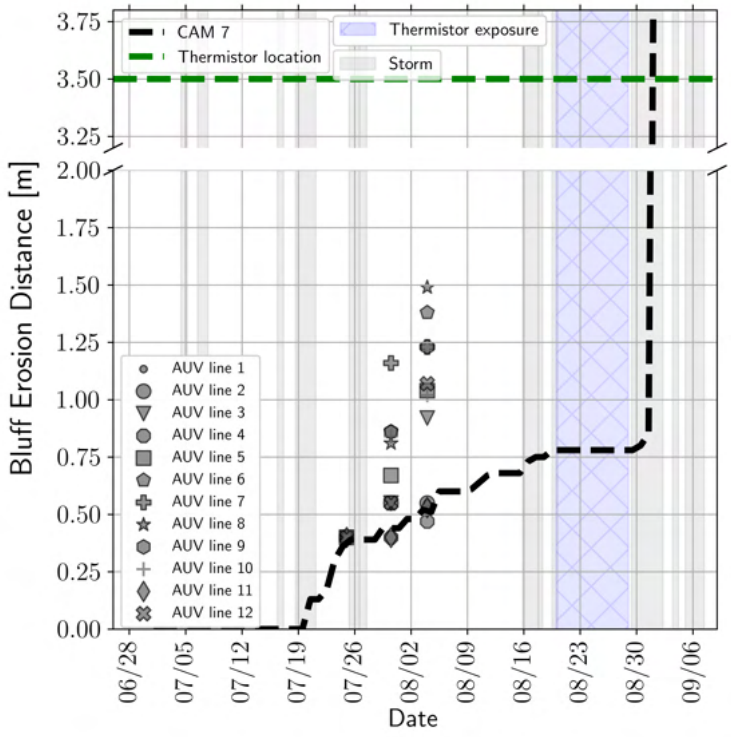

Figure 12. Time series of erosion measurements near the top of the bluff from the 12 AUV transects (gray markers) and the time-lapse camera (dashed black line). The grey shading indicates periods of ocean storms (Figure 7) and blue hatched shading corresponds to the time period of warming thermistor sensors (red lines in Figure 14). The green dashed line above the y-axis break represents the thermistor location on Jul. 1. The bottom of the bluff should approach the green line where it intersects with the blue hatching. Calibration studies will employ these observations as targets in Section 5.2.

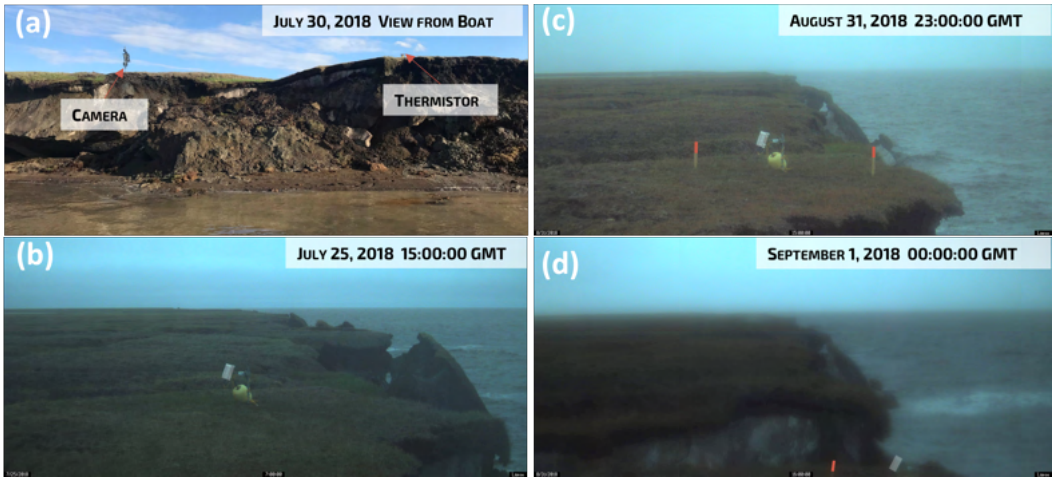

Figure 13. Photographs of and from the time lapse camera documenting the calibration site; (a) shows the neighboring locations of the camera and thermistor as seen from a boat, (b-d) show a series of time-lapse photographs looking west towards the thermistor probe documenting the pre- and post- block breakage event. The stationary field of view confirms measurable denudation between (b) and (c). Although blurry, it is clear in (d) that the block broke at the ice wedge as the orange marker and white box are now almost out of frame. Pictures have been lightened and the orange markers and white box artificially enhanced for clarity.

5.1.2 Niche Development Measurements

Niche measurements are inferred from vertically resolved temperature changes observed at the calibration polygon with the red dot in Figure 11. A vertical thermistor string was installed within the ice-bonded sediment borehole in April; using the AUV survey and erosion information presented above, it has been determined that this was at a distance of 3.5 m inland from the ocean on Jul. 1. Shavings from boring were added around the thermistor and the vegetative mat used to plug the top of the borehole. The D405 BeadedStream satellite telemetered datalogger with a 5.5 m long standard digital temperature cable recorded temperature values every day from Apr. 22 to Jul. 20 and then hourly from Jul. 20 through the block failure event. The thermistor string had 10 sensors measuring temperature changes at the following bluff elevations: -0.3, 0.0, 0.2, 0.5, 0.7, 1.7, 2.7, 3.7, 4.2, and 4.7 m.

Select temperature measurements between Jul. 1 and Sept. 1 are shown in Figure 14. These temperature records uniquely capture niche formation that ultimately led to block collapse. As the lower portion of the vertical thermistor became exposed to the environment (a combination of atmospheric and ocean water between 273-276 K between Aug. 15 and Sept. 1 (see Figure 8)), the temperatures distinctly increased relative to the bluff temperature thus encoding the first known observation of evolving niche geometry, and ensuing block collapse as captured by the camera, along the Arctic coastline.

The first period of observed niche development is seen between Aug. 15 and Aug. 25 (see red lines in Figure 14) and is associated with three closely spaced storms (47, 12, and 17 hours in duration) during which water height exposures of up to 0.9 m occurred (as shown in dark blue in Figure 7). The temperatures indicate that the borehole is still frozen, however a niche is close enough such that thermal conduction is warming the thermistor. This time period when the niche is close to the thermistor probe, but the probe

is not yet reading ocean/atmospheric temperatures, is identified with blue cross-hatched shading in Figure 12 spanning Aug. 20 through Aug. 29.

Next, a faster and more significant niche progression occurred during the second storm between Aug. 29 and Sept. 1; this time period, just before block breakage, is associated with a 95-hour long storm starting on Aug. 29 resulting in exposures up to 1 m in height (see dark blue in Figure 7). Let us recall that the thermistor is located 3.5 m back from the initial bluff face location. Then, by examination of which thermistor elevations possess $\sim$ ocean/atmospheric temperatures in Figure 14, an estimation of the niche geometry can be ascertained as follows. The niche is at least 3.5 m deep (as indicated by our green dashed line on Figure 12): (a) on Aug. 29, 17 hours at z = 0.2 m elevation, (b) on Aug. 29, 19 hours, at z = 0.5 m elevation, (c) by roughly Aug. 29, 20-21 hours, at z = 0.7 m, (d) and just before collapse Sept. 1, 0 hours, at z = 1.7 m. Combined this implies that a niche of at least 3.5 m depth and greater than 1.7 m height (as implied by the vertex of the green lines in Figure 14) would have formed by the time the block failure event happened. As noted above, the time-lapse camera confirms failure at this last measurement on Sept. 1 at 0 hr and the erosion observations (AUV and time-lapse camera generated) estimate the width of the block between 5.5 - 5.8 m right before the block collapse.

The green dashed line and blue hatched shading in Figure 12 will serve as a target in the calibration study when assessing the modeled niche formation. During the time period spanning Aug. 20 through Aug. 29 (blue hatched shading) elevations between 0 and 0.7 m should be close to the green dashed line. After Aug. 29, these elevations should surpass the green dashed line and, although not observed, the depth of the niche will surpass 3.5 m. By Sept. 1, elevations up 1.7 m should surpass the green dashed line.

5.2 Calibration Study

Calibration studies were conducted in a step-by-step manner to best assess the influence of individual parameters (the minimum allowable compressive yield strength Y_{m}, the minimum allowable elastic moduli (general and ocean-contacted) E_{m} and $E_{\mathrm{m,o}}$, and the tensile yield strength σ_{tol}) on resulting erosion behavior and select appropriate values. First, a Y_{m} was selected. Next, a large parameter sweep on E_{m} and $E_{\mathrm{m,o}}$ was conducted to facilitate a study of these parameters' effect on erosion and interaction with one another. During this phase of the study, the tensile yield criterion was deactivated – this enabled an examination of the growing tensile stress in the back of the bluff throughout the summer and around the observed block collapse date, to establish a range of σ_{tol} to be considered for calibration. A subset of results from this large study can be seen in Supporting Information Text S2 and Figure S1 . At this point, a final value for E_{m} was selected based upon upper-bluff denudation, and a finalized smaller range of eligible $E_{\mathrm{m,o}}$ values was identified. Then, a smaller parameter sweep (see Supporting Information Text S3 and Figure S2) was conducted on $E_{\mathrm{m,o}}$ and σ_{tol}, using bounds for σ_{tol} established in the previous stage. This was used to select a final $E_{\mathrm{m,o}}$ and σ_{tol} in concert based on niche formation and block collapse.

Finalized parameter studies and their effect on erosion sensitivity are shown in Figures 15 and 16; Figure 15 highlights the erosion sensitivity with varying E_{m} and $E_{\mathrm{m,o}}$ with the tensile yield strength σ_{tol} set to its final calibrated value, while Figure 16 shows erosion sensitivity with respect to varying σ_{tol}, with E_{m} and $E_{\mathrm{m,o}}$ set to their final calibrated values. Details of the calibration studies and individual parameter selection are presented below.

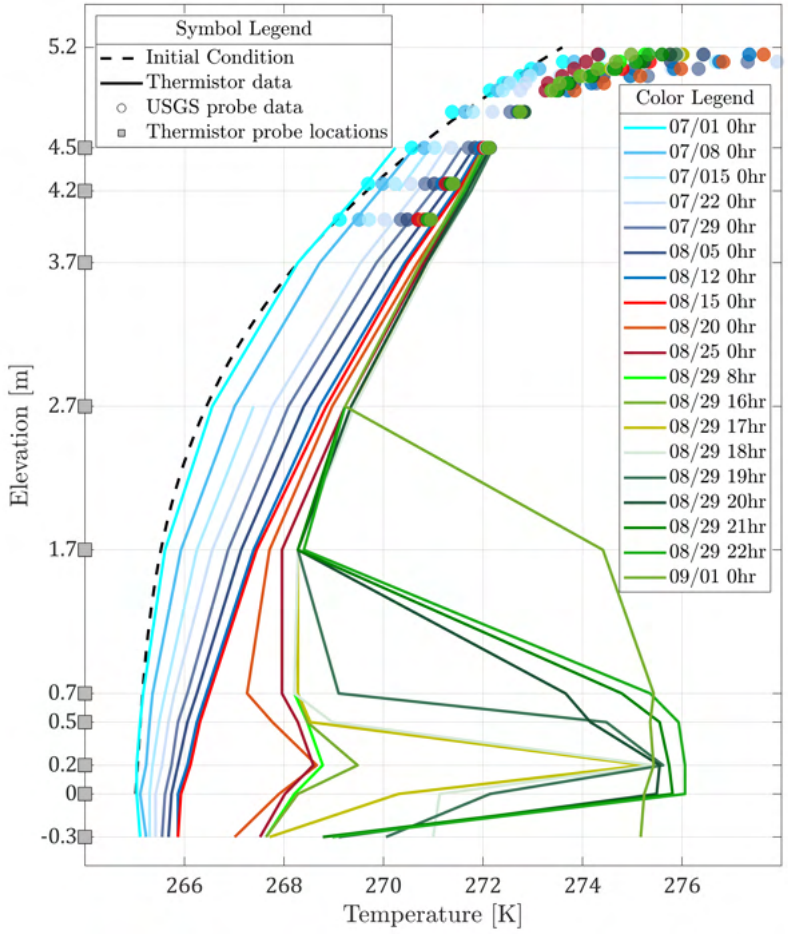

Figure 14. Permafrost borehole temperature profile showing evolution of permafrost temperature over the calibration period and niche development. Thermistor measurement data is depicted in lines, while USGS probe data is shown in markers. Thermistor measurement locations are shown on the left axis with solid squares relative to the top of the bluff at 5.2 m. The bluff toe is at 0 m and matches the oceanographic reference frame. Initial niche development occurred between Aug. 15 and Aug. 20, as indicated by a localized temperature rise in the dashed red lines. Secondary niche development that led to block failure began on Aug. 29 with the series of green lines; on Aug. 29 at 19 GMT, the thermistor becomes exposed to the warmer ocean water and atmospheric temperatures. Niche height grew to approximately 2 m between Aug. 29 and Sept. 1 prior to block failure.

5.2.1 Minimum Allowable Compressive Yield Strength

A range of minimum allowable compressive yield strengths were considered. The two guiding considerations were: (1) ensuring a lack of run-away compressive failure at the back of niche and (2) establishing low yield strengths for regimes of low ice saturation. These two considerations were in balance with one another: the runaway niche behavior required a large value and the other a small value.

The minimum allowable strength was set first to be 0.05 MPa, i.e., the magnitude of the lilac plane in Figure 6 was set at 0.05 MPa. This value was informed by extending the behavior observed in (Li et al., 2015; Rehman et al., 2018) to water content levels comparable with what are considered in this model. After evaluating performance over multiple simulations this value was determined to achieve satisfactory performance and hence a formal sensitivity analysis was not performed.

5.2.2 Minimum Allowable Elastic Modulus

The minimum allowable elastic modulus (E_{m}) directly controls the amount of strain (e.g., shear deformation) of material in response to a given stress in regimes of low ice saturation and/or porosity. In the current calibration study, the porosity values for the domain never go below $\sim 30\%$, and so regions of low ice saturation are the dominating regimes where this value is active. This dictates the material behavior of the thawed ice-bonded sediment which primarily resides at the bluff face (see the ice saturation profiles in the center column of Figure 18). As a result, this value controls thermo-denudation; low values of E_{m} enable large deformations of thawed material which can then surpass the strain removal criterion.

To select the optimal value of the minimum allowable elastic modulus active generally throughout the ice-bonded sediment material, observed rates of denudation from repeated AUV surveys and daily photographs were compared with simulated rates of denudation. The comparison focused on high elevations (z = 4.5, 4.0, and 3.5 m) as the observations were representative of the top of the bluff. A large sensitivity study with E_{m} ranging from 7.5×10^3 to 1.6×10^4 Pa was launched.

As discussed in Section 4.3.3, ocean water interacts with thawed ice-bonded sediment in a way that dissolves the sediment into the ocean over time. This process is represented by applying a distinctly lowered minimum elastic modulus for ocean-contacted material ($E_{\mathrm{m,o}}$) to allow for larger deformations and subsequent larger rates of erosion per the strain limit criteria. Consequently, this value largely controls the rate of niche formation.

To select the optimal value of the minimum elastic modulus for ocean-contacted material, the observed niche geometry (as inferred from the thermistor location and measurements shown in Figure 14) was compared with simulated niche geometry. To facilitate the large sensitivity study, considered values for $E_{\mathrm{m,o}}$ were initially treated simply as a fraction of the E_{m}, with the fractional relationship $\frac{E_{\mathrm{m}}}{E_{\mathrm{m,o}}}$ ranging from $1 - 2000$.

Sensitivity of these parameters was studied simultaneously as there is interaction between the material response in the upper and lower bluff (i.e., changed niche geometries will affect stresses and deformations in the top of the domain for instance). For this study, the tensile yield criterion was effectively deactivated by holding σ_{tol} at an artificially high value of 1000 MPa. This allowed for a more focused study on thermo-denudation in the domain with E_{m}, niche development with $E_{\mathrm{m,o}}$, and tensile stress evolution in the domain. Supporting Information Text S2 illustrates a subset of these simulations in Figure S1 .

5.2.3 Tensile Yield Strength

Significant interaction between the niche geometry and the accumulated tensile stress is anticipated from the results presented in (Thomas et al., 2020). As $E_{\mathrm{m,o}}$ plays a strong role in dictating niche formation, the combined selection of $E_{\mathrm{m,o}}$ and σ_{tol} largely govern the modeled thermo-abrasion. Thus, σ_{tol} was co-optimized in a sensitivity study with $E_{\mathrm{m,o}}$, using a constant $E_{\mathrm{m}} = 1.1 \times 10^4$ identified in the previous stage of calibration. Since the parameter sweep on E_{m} and $E_{\mathrm{m,o}}$ (shown in Supporting Information Text S2 and Figure S2) was completed such that no block failure could occur, interrogation of the tensile stress at the back of the bluff enabled identification of an appropriate range of tensile yield strength values to simulate. As a result, four tensile yield values of 0.12, 0.13, 0.14, and 0.15 MPa were simulated for each $E_{\mathrm{m,o}}$ 55.0, 110.0, 220.0, 550.0 Pa.

The observations guiding the most appropriate performance were: 1) inducing block failure within 3 days of the observed failure, 2) achieving block failure near the ice wedge as was observed, and 3) reproducing the observed niche geometry as closely as possible. Supporting Information Text S3 and Figure S2 in presents results for all of these combinations.

5.2.4 Calibrated Values

The interaction between the calibration parameters E_{m}, $E_{\mathrm{m,o}}$, and σ_{tol} and their impact on thermo-denudation and thermo-abrasion can be best understood via two final sets of simulations, where each set varies two of the parameters and holds the third constant. These are presented in Figures 15 and 16: Figure 15 varies E_{m} and $E_{\mathrm{m,o}}$ using a constant calibrated $\sigma_{tol} = 1.4 \times 10^5$ Pa, while 16 varies σ_{tol} when $E_{\mathrm{m,o}}$ is 220 Pa with a constant calibrated value of $E_{\mathrm{m}} = 1.1 \times 10^4$ Pa. Together, these studies showcase the performed calibration in both thermo-denudation and thermo-abrasion.

Figure 15 presents the co-optimization of E_{m} (varied along the columns) and $E_{\mathrm{m,o}}$ (varied along the rows). As depicted in Figure 12, the camera observed rates of denudation are shown as a continuous black dashed line in Figure 15 while the more aggressive AUV measurements are shown with the markers. As the camera observed the top of the bluff, optimization occurs by evaluating the simulated high elevations (5.0, 4.5, 4.0, and 3.5 m) against the observed values. Since the vegetative mat is simulated with distinct material characteristics, heavier emphasis is placed on matching the 4.5 (rose), 4.0 (yellow), and 3.5 (olive) m elevations to the time-lapse camera and AUV measurements.

As described in Section 5.1.2, the location of the thermistor and the timing of thermistor warming serve as targets in matching observed niche behavior. Figures 12 and 15 highlight the thermistor location 3.5 m back from the initial bluff face with a green dashed horizontal line, and the date range of thermistor exposure to warming temperatures during Aug. 20 - Aug. 29 with a blue shaded and hatched rectangle. The target behavior for the $0 \leq z < 1.0$ lines (purple, dark blue, and blue lines in Figure 15) as outlined in Section 5.1.2 is to: (a) approach the thermistor location, but not reach it, by Aug. 20 (b) reach the thermistor location by Aug. 29 (c) show stratification of approach to the thermistor location by elevation (i.e. $z = 0.25$ line reaches thermistor before $z = 0.5$ line, etc.), as the thermistor data indicates elevations $z = 0.2$, $z = 0.5$, $z = 0.7$ first reached thermistor location on Aug. 29 at roughly 17, 19, and 21 hours respectively.

The center larger panel in Figure 15 achieves both of these targets with a calibrated value of 1.1×10^4 Pa for E_{m} paired with an $E_{\mathrm{m,o}}$ of 220 Pa. The selection of the optimal $E_{\mathrm{m,o}}$ value is dependent upon σ_{tol} with Figure 16 revealing the differing niche geometries with distinct σ_{tol}. Looking across the multiple panels of Figure 15, the degree of control that E_{m} and $E_{\mathrm{m,o}}$ exert over erosion and hence bluff geometry is large. Values of E_{m} that are too low can result in accelerated denudation (left column), while val-

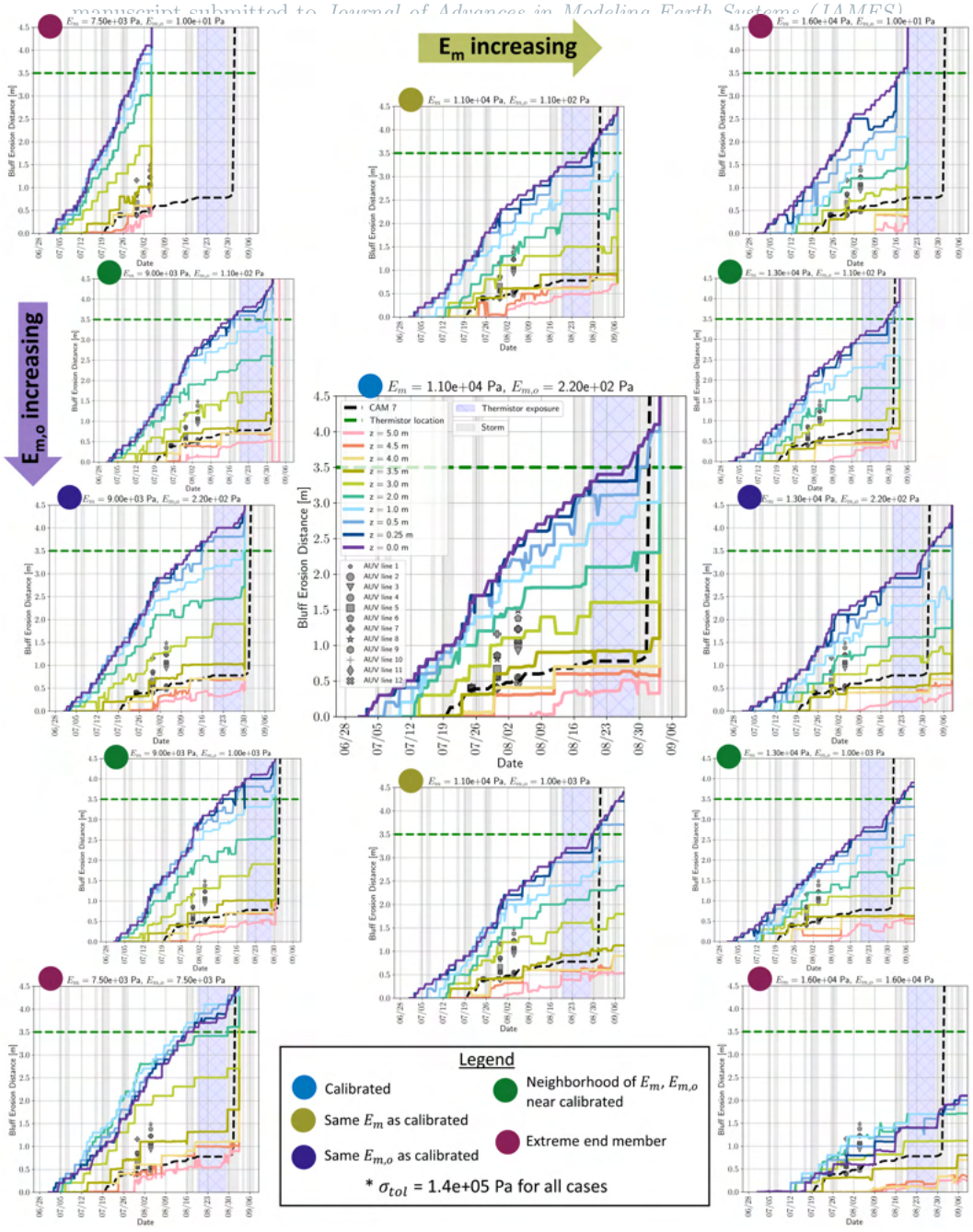

Figure 15. Erosion sensitivity with respect to varying combinations of E_{m} (columns) and $E_{\mathrm{m,o}}$ (rows). Each panel represents a distinct combination of calibration parameters. Within each panel: observed erosion measurements are shown with the time-lapse camera (dashed black line) and 12 AUV transects (gray markers); simulated rates of erosion are shown as a function of elevation through distinctly colored lines; and grey shading indicates periods of ocean storms, blue hatched shading corresponds to the time period of warming thermistor sensors (red lines in Figure 14), and the horizontal green dashed line indicates the thermistor location. A simulation calibrated for E_{m} is one in which high elevations match the dashed black line and low elevations approach and then surpass the green dashed line within the blue shading. ice-bonded sediment material stiffness is increased as one moves down and to the right across the panels. The bottom row represents simulations for which $E_{\mathrm{m}} = E_{\mathrm{m,o}}$ – there is no differentiating material property with and without ocean contact.

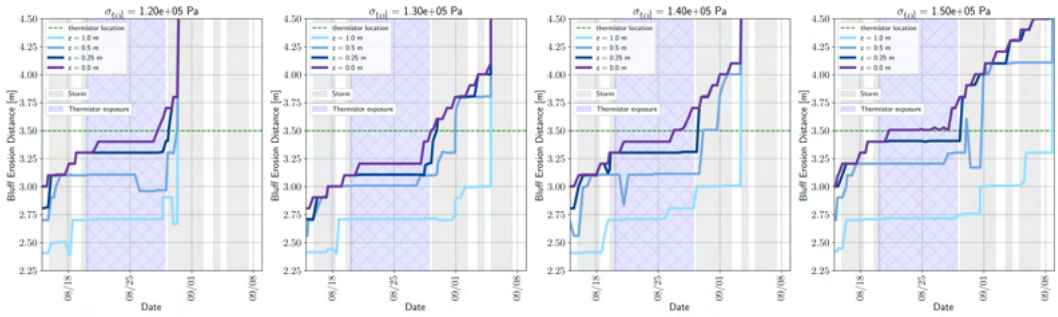

Figure 16. Erosion sensitivity with respect to varying σ_{tol}, as displayed on the titles of each panel, for $E_{\mathrm{m}} = 1.1 \times 10^4$ Pa and $E_{\mathrm{m,o}} = 220$ Pa. These panels focus on the time period when the thermistor was recording the niche geometry and only on the lower elevations (z = 0, 0.25, 0.5, and 1.0 m) in comparison to Figure 15. Differences in the niche geometry are clearly a function of σ_{tol}, with 1.4×10^5 Pa obtaining the desired characteristics (close to the green line at the beginning of the blue cross-hatched shading and surpassing the green line after the blue cross-hatched shaded region with good stratification) whilst still achieving block failure within 2.5 days of the observed.

ues that are too high will suppress most denudation (right column). This is also true of $E_{\mathrm{m,o}}$; when $E_{\mathrm{m,o}}$ is very low (top row) it is clear that the niche develops quickly, whereas when it is high (bottom row) it takes much longer to develop. Furthermore there is a clear interaction between E_{m} and $E_{\mathrm{m,o}}$; for instance, achieving more aggressive rates of denudation at the top of the bluff favors lower values of E_{m}, however, these low values result in niche geometries that progress too fast (left column). Additionally, the relevance of applying an $E_{\mathrm{m,o}}$ that is distinct from E_{m} to help account for ocean contact is clear; scenarios where the two parameters are equal (bottom row) result in incorrect niche geometries with concave shapes (i.e., 0.0 erodes less than 0.25 m).

Figure 16 shows the effect of distinct tensile yield strengths with the calibrated E_{m} and $E_{\mathrm{m,o}}$ values. A $E_{\mathrm{m,o}}$ calibrated value of 220 Pa was selected as this consistently showed the niche geometries close to the desired shape (close to the green line at the beginning of the blue cross-hatched shading and surpassing the green line after the blue cross-hatched shaded region with good stratification). Evaluating the effect of the tensile yield on both niche geometry and block breakage date in Figure 16 reveals premature breakage for values that are too low and delayed breakage for values that are too high. A final calibrated value of $1.4{\times}10^5$ Pa was selected as the shape of the niche achieved higher depths across taller elevations whilst still causing block breakage withing a few days of the observed breakage.

As clearly shown in Figure 6(c) the calibrated value is lower than the majority of the experimental values, except one point. Previous literature, (Hoque & Pollard, 2009), calibrated the tensile yield to lie between 1.0×10^5 - 2.0×10^5 Pa and (Barnhart, Anderson, et al., 2014) employed the upper value of 2.0×10^5 Pa from (Hoque & Pollard, 2009) in her simulations. Thus, even though this is lower than the experimental values, it does fall within previously identified ranges. Additionally, as shown in Figure 16, even moving to 1.5×10^5 Pa results in a significant delay for block breakage and it is clear that selecting a much higher value that is representative of the experimental values would not result in block breakage. It is also worth noting that tension at the back of the bluff is developed by the weight of the elements overhanging the niche, and this optimized value may be affected by the simulation domain's constraint to a slice that is only one element thick.

5.3 Calibrated Results

The results presented below employ the calibrated values obtained in the studies above of $Y_{\mathrm{m}} = 5.0 \times 10^4$ Pa, $E_{\mathrm{m}} = 1.1 \times 10^4$ Pa, $E_{\mathrm{m,o}} = 220.0$ Pa, and $\sigma_{tol} = 1.4 \times 10^5$ Pa, and the parameter values identified in Tables 5, 6, and 7.

5.3.1 Thermal Evolution

5.3.1.1 Comparison between modeled and observed ground temperature In comparing the modeled thermal evolution against observational data, two temperature probes were utilized – the USGS probe at Drew Point (Urban & Clow, 2018; Urban, 2021), and the thermistor probe installed in a borehole 3.5 m from the bluff face on Jul. 1, 2018, previously described in Section 5.1.2. The USGS probe provides ground temperature measurements at depths up to 120 cm (elevations $4.0 < z < 5.2$ m), while the vertical thermistor string provides readings at elevations at $-0.3 < z < 4.5$ m. The modeled thermal evolution is compared with observations from each of these probes, and the difference between observed and simulated subsurface temperatures, $T_{\mathrm{probe}} - T_{\mathrm{sim}}$, is displayed in Figure 17(a-c). Panel (a) highlights differences varying with elevation for selected dates in color, with triangle markers denoting USGS comparison and circle markers denoting thermistor comparison, while Panels (b-c) show differences evolving in time with elevations noted in color, comparing against (b) the USGS probe and (c) the vertical thermistor string. For all plots, the uncertainty between probes is established by taking the maximum difference between the thermistor string and USGS probe observations at overlapping elevations over the time period considered, which is $\sim$ 0.4 K. We choose to plot dates from Jul. 1 - Aug. 19, as afterwards the thermistor begins to experience warming due to the approaching niche, and temperature comparisons at low elevations are less informative due to differences in timing between modeled and observed niche incursion.

In general there is good agreement between modeled and observed temperatures at either lower ($z < 2$ m) or higher ($z > 4.75$ m) elevations. This is to be expected, as the lower elevations feature less temperature change overall, and the higher elevation points are closer to the domain boundary at $z = 5.2$ m, which uses the USGS temperature at 5 cm depth as a boundary condition on the temperature. At the middle elevations ($2 < z < 4.75$) there is a greater difference between modeled and observed temperatures; the highest deviations reach $\sim 1.5 - 2.0$ K by the end of the 1.5 month period, with both observational probes measuring a higher temperature than the modeled. The differences also grow slightly over time, suggesting that the observational probes experienced a higher rate of warming at these elevations compared with the model.

Upon first glance, this finding is a bit surprising – we expected to best match the observed temperature from the vertical thermistor probe, because the thermal material properties and freezing curve characteristics utilized for the study (Section 4.2.3, Figures 9, 10) were derived using constituent material characteristics obtained from cores taken from that exact location (Section 2.1.1, Figure 5). However, even at comparable elevations where data from both probes is available (i.e. $z = 4.2{-}4.5$), there is better agreement with the USGS probe than the thermistor. One potential explanation for this is simply that the USGS probe temperature was used as a boundary condition for the top of the modeled bluff; it is possible that the location of the vertical thermistor string saw slightly different upper elevation temperatures than the USGS probe, and thus has a slightly differing thermal evolution. Another possibility is that the borehole where the thermistor was placed possessed different thermal properties than what was modeled because of the removal of the cores used for constituent material characterization; i.e. upon removal of the cores, the surrounding sediment may have collapsed into the hole (resulting in a different porosity than what was originally measured), or pore water may have

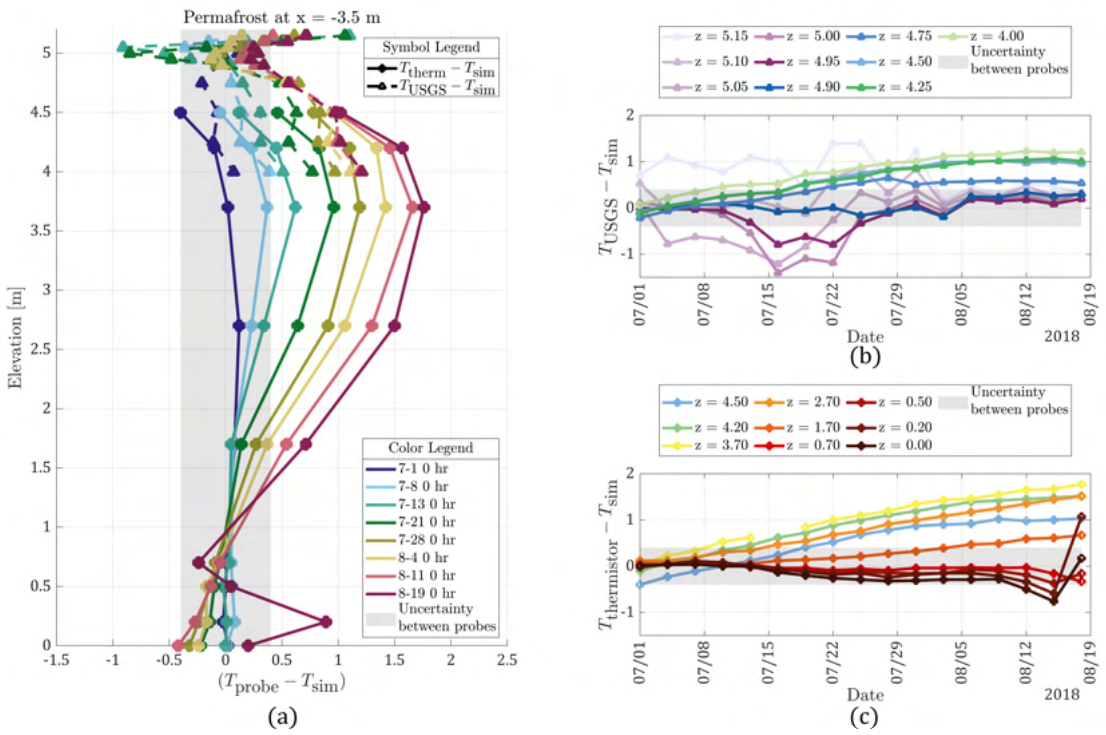

Figure 17. Comparison of temperature evolution of modeled permafrost at $x = -3.5$ m in simulation domain with observed temperatures from USGS probe and vertical thermistor string. The difference between modeled and observed temperatures is shown: (a) varying with elevation for selected dates in color, with triangle markers denoting USGS comparison and circle markers denoting thermistor comparison, and (b-c) evolving in time for different elevations shown in color, comparing against (b) the USGS probe and (c) the vertical thermistor string. For all plots, the uncertainty between probes is established by taking the maximum difference between the thermistor string and USGS probe observations at overlapping elevations over the time period considered.

seeped in, resulting in altered thermal properties from Figures 9 and 10 of the surrounding ice-bonded sediments.

Comparison of the ice wedge's thermal evolution located at x = -6.55 m of the simulation domain (see Supporting Information Text S4 and Figure S3) with the ice-bonded sediment's thermal evolution clearly confirms that the model responds appropriately to different thermal material properties. The better agreement with the probes at these middle elevations in the ice wedge indicates that higher thermal diffusivities ($\alpha = k/(\rho C_p)$), as seen with ice as compared with ice-bonded sediments (see Supporting Information Text S4 and Figure S4), may be responsible for the observed faster thermal evolutions. This discrepancy in diffusivity could arise from incorrect representation of material properties surrounding the thermistor (as mentioned above) or from shortcomings in capturing the freezing curve behavior resulting in non-representative ice saturation's. The elevations where the highest differences in probe versus modeled temperature occur are in a region of transition from high to intermediate modeled ice saturation ($0.6 < f < 1.0$, see Supporting Information Text S4 and Figure S5). If the model is biased towards thawing material prematurely, this could result in a lowered thermal diffusivity (see Sup-

porting Information Text S4 and Figure S4), and consequent slower thermal evolution compared to the observed.

Future studies aimed at evaluating the thermal model's performance over a larger time period, i.e. several years, could be an excellent opportunity to assess the thermal model in greater depth and identify areas for improvement. For example, thermal models such as those in (Nicolsky et al., 2017) and (Westermann et al., 2013) compare modeled versus observed ground temperature profile over decadal climatologies and 2 years respectively. Both studies take the approach of calibrating ground thermal properties based on observed ground temperature from site-specific boreholes. Thermal properties calibrated to match temperature histories at Drew Point and Utqiagvik in (Nicolsky et al., 2017) are within $\pm \sim 40\%$ of our mixture model derived thermal properties at comparable elevations, with (Nicolsky et al., 2017) calibrating thermal diffusivities higher than that of pure ice at 1.0 m depth. Both models obtain deviations between modeled and observed of up to $\sim 2-5$ K. This current study may be the first, to date, that derives temperature evolution at these depths based on mixture model derived thermal properties, and so it would be interesting to see how the presented thermal model compares with these studies on these longer time scales.

Nonetheless, for the purpose of the current study, the agreement with observations is more than sufficient. Most importantly, the agreement is very good (remains generally bounded within the uncertainty between the two observational probes) closer to the surface (and by extension we assume to the bluff face) where regions of lowest ice saturation ($0 \leq f <\sim 0.4$) occur, which have the largest impact on transition in mechanical material properties (i.e. decreasing elastic modulus and yield strength as $f \rightarrow 0$) and consequent erosion mechanisms (i.e. removal by strain limit). In particular, removal by strain limit, which is responsible for the majority of mesh erosion (see Section 5.3.4 Figure 20), occurs in this regime. The tensile yield criterion σ_{tol}, which is key for capturing block failure, is active independent of ice saturation (recall plane in Figure 6(c)), and thus is not affected by ice saturation in the current model configuration.

5.3.1.2 Temperature and ice saturation progression The thermal evolution of the calibrated simulation is informative, as it is this progression that controls the ice saturation f and the resulting mechanical characteristics. The modeled thermal state of the entire simulation domain for selected dates is illustrated in Figure 18, with the temperature shown in the far left column, and the ice saturation f in the middle column (note, Supporting Information Movie S1 provides an animation of this figure over the entire simulation time period). The temperature colormap is incremented over set ranges centered around 271 K, corresponding to intermediate ice saturation regimes of $0.4 < f <\sim 0.8$ (as shown in the freezing curves of in Figure 10) to more clearly illustrate the spatial temperature patterns.

As expected, grid cells closest to the top and bluff face boundaries exhibit the warmest temperatures, with corresponding near-complete thaw – ice saturations of $f \sim 0$ occur throughout almost the entire peat layer and along the bluff face typically $1-3$ grid cells deep. Farther from these boundaries, there is a larger region of intermediate ice saturation ($f \sim 0.6-0.8$), before reaching the fully frozen state at lower elevations and in the ice wedge.

Lower elevations also experience an intermediate level of thaw over time as the niche develops, bringing warmer temperatures as the boundary encroaches from both the ocean and atmospheric boundary conditions. As the freezing curve given in Equation (14) collapses to $f = 1$ for $\nu_{\text{bulk}} = 0$, the ice wedge region of the domain remains fully frozen throughout the simulation, due to the lack of constituent sediment materials in this area. The influence of salinity can be noted in the fourth row (Aug. 20), where the higher salinity at lower elevations (recall Figures 5(c) and 10) depresses the freezing point. This results in a lower ice saturation at colder temperatures within the lower elevation region

$0 < z < 1.0$ m compared with the warmer but fully frozen region above it at $1.0 < z < 2.0$ m.

Ice saturation is one of the fundamental controls over the material properties presented in Sections 4.2.3 and 4.3.3. Cells with low ice saturation will possess the minimum allowable for elastic modulus value, $E = E_{\mathrm{m}}$, resulting in a very compliant material and enabling relatively large deformations. Cells in this regime are more likely to be removed via the strain criterion, which imposes a limit on the extend of shear deformation that can occur. In contrast, cells with high ice saturation will possess elastic modulus values somewhere along the rising curve portion of Figure 6(a), resulting in a stiffer material that will not deform as much but is more likely to accumulate stress up to the compressive or tensile yield values ($Y_{tol}(f, \theta)$ or σ_{tol}).

5.3.2 Erosion by Thermo-denudation

The last column of Figure 18 illustrates, with failure indicators, how close an element is to meeting either strain or tensile yield removal rules. Strain failure criteria control thermo-denudation along the ice-bonded sediment elevations close to the surface (4.5, 4.0, and 3.5 m). The strain indicator is evaluated as the shear deformation experienced by the cell (see Equation (36)) divided by the strain limit value (as identified by γ_{tol}) – when it possess a value of 1, the cell will be removed.

The black line running above the peat layer illustrates the observed denudation from the time-lapse camera. A total of 0.80 m of erosion was observed from Jul. 1 through Aug. 31 in the higher elevations by the camera; thermo-denudation estimates from the AUV are larger as detailed in Section 5.1. Daily RMSE is assessed between modeled and observed erosion amount by evaluating RMSE $= \sqrt{\frac{1}{N}\sum_n^N \left(y_{\mathrm{obs}}^n - y_{\mathrm{sim}}^n\right)^2}$, where N = number of days observed. Simulated erosion over the same time period in the z = 4.5, 4.0, and 3.5 m elevations was 0.91, 0.71, and 0.91 m with daily root-mean square error (RMSE) values from a total of 60 measurements of 0.20, 0.14, and 0.14 m respectively. The average denudation over these three horizons is 0.7 m with a RMSE of 0.16 m. Hence, although our denudation is less aggressive then that observed by either the camera or the AUV surveys, it does achieve average thermo-denudation magnitudes with a low RMSE.

It is noteworthy that calibrating the top elevations for denudation confines us to a certain section of the strain criterion with higher peat fractions. However, by 3.5 m elevation, the peat fraction has dropped significantly and denudation performance at this horizon is still quite strong.

5.3.3 Erosion by Thermo-abrasion

Thermo-abrasion is characterized by the development of a niche at the base of the bluff through the thermo-mechanical interaction with the ocean. As the niche grows deeper, this stress increases in high ice saturation ice-bonded sediment behind the niche, and, as anticipated from the work of (Thomas et al., 2020), results in block failure. The last column of Figure 18 illustrates the geometry of the niche and the tensile stress indicator over the summer calibration period, and Figure 19 highlights the rapid dynamics underlying block failure failure.

5.3.3.1 Niche Formation The achieved niche geometry must be realistic to then attain tensile stresses that could result in block failure. Hence, we first evaluate how close the simulated niche geometry was to observed values. Observations from the thermistor indicate that the niche depth would have been *at least* 3.5 m with a height of 1.7 m just before the block broke, as noted in Section 5.2. The best calibrated niche shown in Figure 18 does surpass 3.5 m depth at the lowest elevations (0, 0.25, 0.5 m) but the height of the niche is much lower, extending only up to 0.8 m instead of 1.7 m.

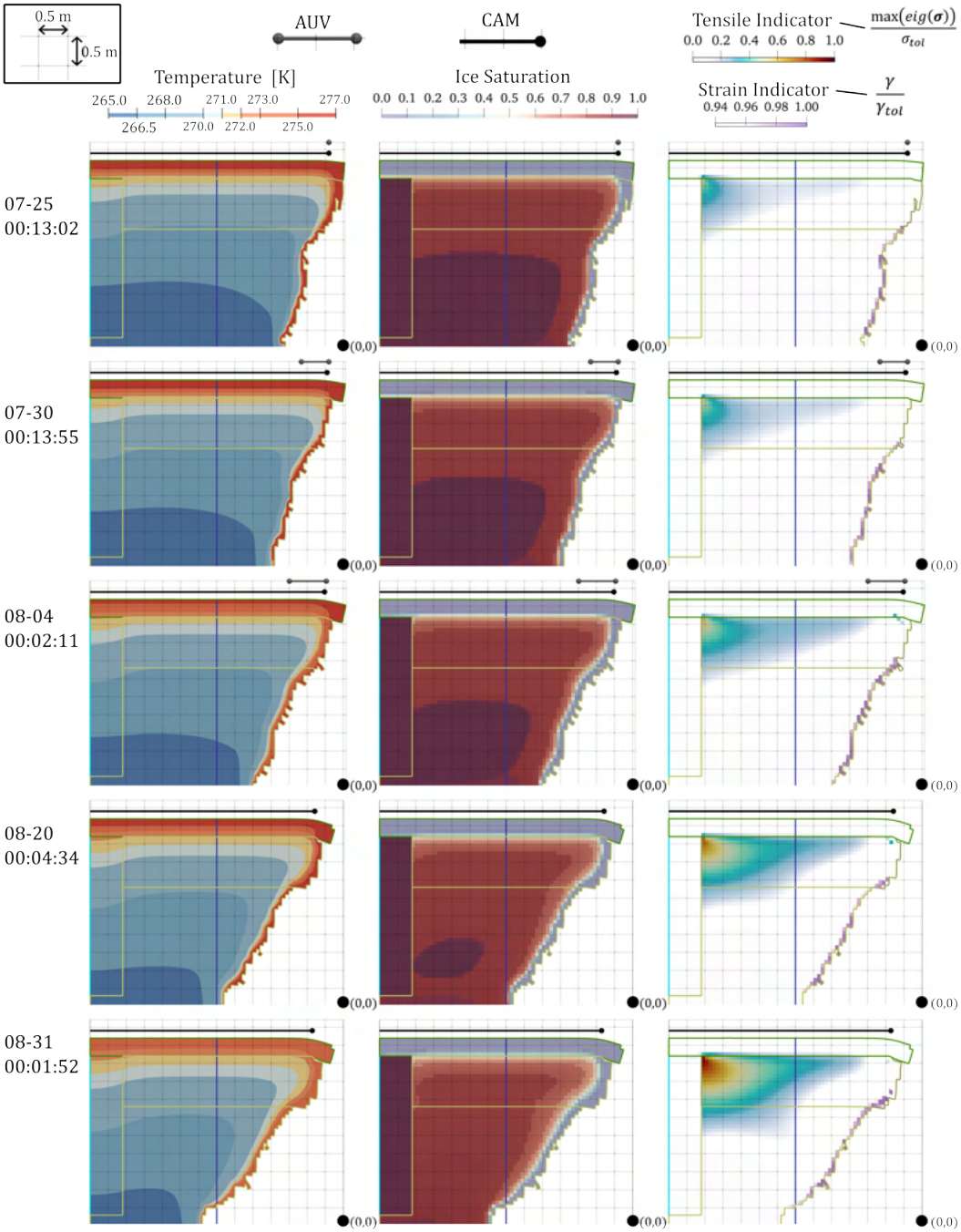

Figure 18. Snapshots of the bluff (left) temperature, (center) ice saturation, and (right) strain and tensile failure indicators at select dates (rows), where a failure indicator value's proximity to one represents how close an element is to meeting removal by that criterion. Supporting Information Movie S1 provides an animation for each of these columns over the entire simulation time period. The thermistor location is shown with a blue vertical line. The ice wedge, peat, two ice-bonded sediment layer material blocks are outlined in cyan, green, and mustard respectively. Horizontal lines above the bluff profile show the denudation magnitudes measured by the camera (black) and AUV (grey, when available).

The niche experienced accelerated progression during the storm that commenced on Aug. 29 at 8 am. During this 95 hour long storm with water temperatures above freezing, the niche depth of 3.7 m and height of 0.2 m progressed to a depth of 4.1 m and height 0.8 m. This progression is a direct result of the interaction with the ocean during this time period and demonstrates the models responsiveness to environmental drivers. This niche geometry was maintained until the mid-day block failure on Sept. 3.

Since the water contact history is processed into an exposure history (see Section 3.3.1), the highest water contact levels, surpassing 1.2 m in Figure 7, will only be included as an exposure history boundary condition if the cumulative contact time surpasses the time step ($\Delta t_{\max} = 900$ sec in Algorithm 1). Given that these highest water contact levels do not achieve this condition, the highest water contact levels are not embodied as boundary conditions. Hence, an underestimation of niche height should be anticipated from the model given its current instantiation.

5.3.3.2 Block Failure The last column of Figure 18 and the time-series in Figure 19 illustrates the tensile indicator. This is the ratio of a cell's maximum tensile stress value (Equation (31)) divided by the constant calibrated tensile yield stress, σ_{tol}. As is the case for the strain indicator, when a cell possesses a high value (yellow to red), the cell is close to removal via the tensile yield failure criteria. In both Figures 18 and 19, this indicator is high behind the niche near the surface.

Figure 19 clearly illustrates how block failure is a direct result of tensile failure. Tensile stress accumulates in the mostly frozen cells near the ice wedge after the completion of the Aug. 29 storm, and the niche geometry remains static. The cells near the ice wedge are the first to surpass the strain limit resulting in their removal and the development of a crack; tension cracks like the one simulated here have been documented and discussed in (Thomas et al., 2020). With the development of the crack, the adaptive time-stepping is activated, and the "reduction factor" r_f, as described in Algorithm 1, is continually employed until converged solutions are obtained for all of the elements in the domain resulting in the very short time steps between updated geometries displayed in the Figure 19 time series. This crack then moves quickly along the ice wedge towards the back of the niche. As it does so, the bluff begins to displace and rotate under gravitational forcing. As the displacement and rotations become large enough their respective tolerances are surpassed and cells are removed. The time evolution of the block failure occurs over only a few seconds (around 2 sec). Supporting Information Movie S2 provides an animation of these snapshots.

Camera observations estimated the extent of the ice-bonded sediment before the ice wedge to be 5.95 m on Jul. 1 with a total of 0.8 m of thermo-denudation by Aug. 31. Hence a total of 5.15 m of ice-bonded sediment has been observed as collapsing in a block failure event on Sept. 1 2018. Here we simulate a total of 5.4 m (initial extent of 6.1 m denuded by 0.7 m) of permafrost collapsing in a mid-day block failure event on Sept. 3 2018.

As discussed in Section 5.2, the selection of σ_{tol} has been selected to achieve this failure within 3 days of the observed failure; here we achieve failure within 2.5 days of the observed. Block failure is a direct result of the niche geometry and the accumulating tensile stresses in the remaining bluff. In this calibrated simulation, the selected σ_{tol} is likely an underestimation of the true σ_{tol} as this simulation cannot develop magnitudes of tensile stresses likely experienced in the field. Simulated stresses are likely less than field stresses for two reasons: 1) niche heights that are too low and 2) calibrating on only a slice of the morphology instead of the 3D representation. Regardless, the selected σ_{tol} is within the range that was established in (Hoque & Pollard, 2009).

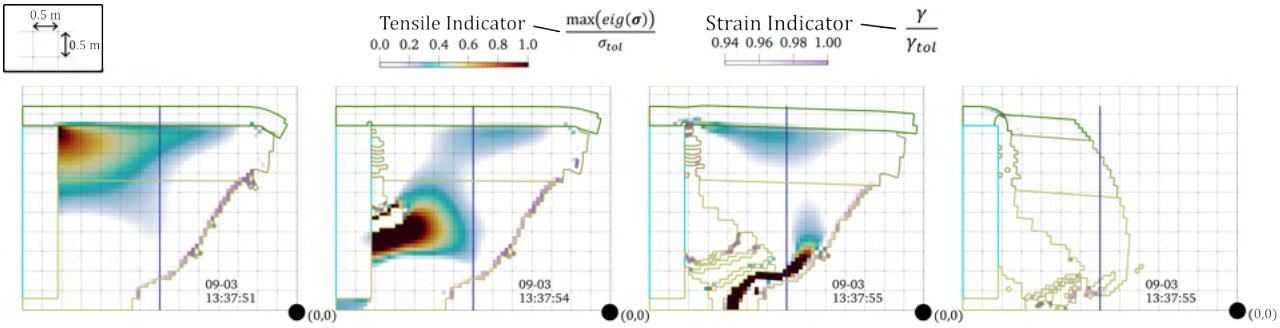

Figure 19. Snapshots of the bluff profile during the ∼2 sec block failure event; the date and time stamp are displayed in the bottom right corner of each panel (Supporting Information Movie S2 provides an animation of these snapshots). Similar to Figure 18, each panel displays tensile yield and strain failure mechanisms through indicator values representing how close an element is to meeting the removal criteria, the thermistor location is shown with a blue line and each block of material (ice wedge, peat, and the two ice-bonded sediment layers) are outlined in cyan, green, and mustard respectively.

5.3.4 Calibration Summary

Figures 18 and 19 illustrate the geometry and key field values (temperature, ice saturation, and failure indicators) for the calibrated simulation. As summarized below in Table 8 the ACE model has calibrated values of Y_{m}, E_{m}, $E_{\mathrm{m,o}}$, and σ_{tol} to match observed erosion through thermo-denudation and thermo-abrasion. In calibrating the simulation, it was not possible to simultaneously optimize all metrics and hence each one is imperfect, but, on the whole, the overall erosion characteristics in terms of the time evolution of total volume of material eroded are quite good. The daily-based average RMSE of 0.16 m over the z= 4.5, 4.0, and 3.5 m elevations further solidifies the temporally evolving accuracy of the calibrated ACE model.

	Erosion from Jul. 1 to Aug. 31 (denudation) [m]	Erosion from Aug. 31 to Sept. 9 (block collapse) [m]	Niche height before block collapse [m]	Niche depth before block collapse date [m]	Date of block collapse
Observed/Inferred	0.80	5.14	1.7	> 3.5	Sept. 1, 0 hr
Simulated	0.70	5.40	0.80	4.10	Sept. 3, 13 hr

Table 8. Comparison of observed and inferred erosion via thermo-denudation and thermo-abrasion, niche geometry (depth and height), and date of block collapse with simulated values from the calibrated ACE model. Thermo-denudation magnitudes (first column) are obtained by averaging the erosion amounts over Jul. 1 to Aug. 31 at z = 3.5, 4.0, and 4.5 m.

Importance of erosion failure mechanisms can be measured in two ways: 1) in its efficacy to remove material, 2) in its temporal dominance. To understand the role of the five erosion criteria over the summer, the log of the cumulative failure of integration points is shown in Figure 20. All 8 integration points within a grid cell must fail for the cell to be removed and so some integration points may be counted as failed for multiple timesteps before their corresponding grid cell is removed resulting in totals of more than 100%. Figure 20 clearly indicates that failure in strain (rose) is the most common failure mechanism highlighting the importance of thermo-denudation as a key erosion driver along the Arctic coastline. The kinematic failure mechanisms (displacement (dark blue) and rotation (blue)) are the next most important. As can be see in Figure 18, cells undergoing significant strain also displace and rotate, hence, these two rules work in concert to remove grid cells experiencing thermo-denudation. However, as summarized in Table 8 the degree of erosion is much less in thermo-denudation than in thermo-abrasion. This dichotomy was also highlighted in (Ward Jones et al., To be Submitted) and is central to why simultaneously simulating both thermo-denudation and thermo-abrasion is needed to accurately predict future erosion rates. The adaptive time-stepping employed in the model, as described in Section 4.4, is central to our ability to capture slowly evolving thermo-denudation and highly dynamic block failure events.

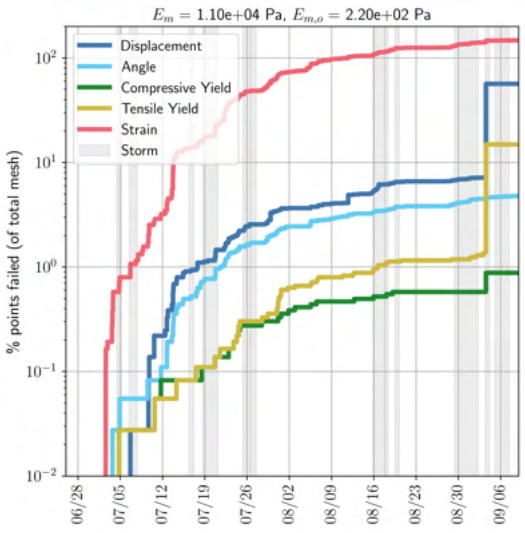

Figure 20. Overall importance of each failure mechanism as a function of time displayed through the log of cumulative failure of integration points for each failure mechanism; totals larger than 100% possible as some integration points may be counted as failed for multiple timesteps before their corresponding grid cell is removed. Failure through strain shown in rose, through displacement in dark blue, through rotation in blue, through tensile yield in mustard, and through compressive yield in green. Oceanographic storms highlighted with grey shading.

A key aspect of the dynamic block failure events is that they are the result of stresses building over a much longer time period (Figure 18 last column). As demonstrated here, stress had to accumulate near the ice wedge for the tensile crack to develop, reinforcing the finding in (Ward Jones et al., To be Submitted) that block failure can occur at unpredictable times that may be lagged from the storm itself. With the advent of this crack, the tensile failure mechanism (mustard) increases in importance in Figure 20. As the bluff detaches from the ice wedge, shown in Figure 19, the majority of the interior cells are

then removed via the displacement failure mechanism (dark blue) causing a large spike the failed integration points.

6 Discussion and Conclusions

Development and calibration of the ACE model has resulted in the first-of-its kind multi-physics simulator with the potential to predict permafrost erosion in response to complex interactions between model components (Figure 2). The ACE model calibration matched total magnitudes of erosion; a 12.5% error for thermo-denudation and 5.06% error for block failure. The temporal evolution was also matched; an daily RMSE of 0.16 m was achieved for denudation and block failure occurred within 2.5 days of the observed. Three other aspects of the calibration are notable. The first lies in the dichotomous behavior that although thermo-abrasion accounts for the largest magnitude of removal, thermo-denudation occurred more often. The second lies in exposing how stress accumulation behind the niche is responsible for block failure and that this model is capable of representing lagged block failure behavior to storms. And lastly, sensitivity of the ACE model to environmental drivers of varying degree has been established with storms clearly acting to accelerate erosion for the calibrated values. We have thus illustrated that this local, event-based simulation framework possesses sufficient physics such that it is capable of predicting permafrost erosion rates.

As constructed, the ACE model is capable of producing mixture based thermal models for a wide range of terrestrial compositions and linking the mechanical material behavior to the thermal state, thus catering the mechanical attributes to distinct compositions. Simulation domain construction is not agnostic to the morphological characteristics of the site, again heightening the applicability of the model to distinct locations. Relevant terrestrial material properties include fractions of constituent sediments and peat, porosity, salinity, and morphological information. Significant effort was invested in determining these material properties as a function of bluff elevation. Additional experimental work was performed to determine mechanical material properties as a function of ice saturation and porosity. It has yet to be established how extensible these mechanical material properties are. Polygons at Drew Point of distinct geologic origin (e.g. primary material or drained lake basin) offer an excellent opportunity to validate the ACE model as material properties were collected as a function of elevation during the 2018 field campaign. This validation at other Drew Point polygons can be further bolstered with the field campaign extending into 2019 with a much more aggressive erosion regime (Figure 3(b) and (Ward Jones et al., To be Submitted)). Additional extension to other well-studied sites (e.g. Barter Island (A. E. Gibbs et al., 2021)) would offer an even deeper exploration of the extensibility of the Drew Point derived stress-strain characteristics as a function of f and θ. These validations are the subject of future research which is now possible as it will stand upon a baseline calibrated model.

Although much emphasis has been placed on the development of the finite-element terrestrial model in this paper, the role of spatio-temporally matched environmental drivers in establishing realistic time evolution of erosion should not be underestimated. Representing the process of ocean water interacting with thawed ice-bonded sediment to dissolve the sediment into the ocean over time as an accelerated deformation enabled the accurate depth of niche formation even though this was achieved through a somewhat crude hijacking of the E_{m}. A more realistic treatment of this process would employ the time-varying wave pressure sensitive to the persistence of water submergence coupled with fluid flow to determine more appropriate rates of sediment dissolution. Additionally, the exposure time history plays a significant role in determining when $E_{\mathrm{m,o}}$ are employed. Although initial sensitivity studies were performed to determine the trade-offs between coupling time-step and grid resolution with exposure time history, a thorough analysis of implications of larger time steps and grid resolutions could deepen the understanding of the ACE model performance.

Thus far, the inability of the current model implementation to support evolving Neumann boundary conditions with an eroding mesh in parallel has limited simulations to 2D due to computational expense constraints. As such, while the model performance here is notable, this work has yet to be tested in its full 3D configuration. The tensile yield stress, in particular, may require a distinct tuning when transferring to 3D. Further code development to enable parallelization of the model will expand the computational capability to full 3D simulations.

As shown in this article, the calibrated ACE model has successfully reproduced both the thermo-denudation erosion process and the thermo-abrasion process as embodied by niche formation and block breakage. Calibration data, components of the ACE model (see Figure 2), and tuned parameter values were presented within this paper. Future analyses will focus on deepening the applicability of the model through validation studies at sites with distinct material properties, altering the representation of niche formation, and pursuing computational alterations to enable 3D configurations. This model can be used to predict rates of erosion in response to changing environmental drivers and with sensitivity to geomoprhological composition. This enables the model to be utilized for community-based adaptive actions, as well as facilitating land-to-ocean fluxes at circum-Arctic scales.

Open Research Section

Albany-LCM is available at https://github.com/sandialabs/LCM. The commit ID used to produce results for this paper is b1a0c09ccb6d643fca4e4f6c348ee65a0484806d. Observational data presented in this paper is available at `https://doi.org/10.5281/zenodo.14862274` (D. Bull et al., 2025). Simulation output and analysis scripts are available at `https://doi.org/10.5281/zenodo.14920734` (Bayat et al., 2025).

Acknowledgments

This research was funded as part of the Interdisciplinary Research for Arctic Coastal Environments (InteRFACE) project through the Department of Energy, Office of Science, Biological and Environmental Research RGMA program. This work was additionally supported by the Laboratory Directed Research and Development program at Sandia National Laboratories, a multimission laboratory managed and operated by National Technology and Engineering Solutions of Sandia, LLC., a wholly owned subsidiary of Honeywell International, Inc., for the U.S. Department of Energy's National Nuclear Security Administration under contract DE-NA-0003525. Additional support for BMJ and MKWJ was provided by the U.S. National Science Foundation (OPP-2336164) and to BMJ through a Broad Agency Announcement award from ERDC-CRREL, PE 0603119A. The writing of this manuscript was funded in part by IKT's Presidential Early Career Award for Scientists and Engineers (PECASE). We would additionally like to thank other original team members on the development of the model or experimentation: Jim McClelland, Jeremy Kasper, Craig Connolly, Richard Buzzard, Matt Thomas, and Eloise Brown. We would like to thank Ethan Conley for his help in creating Figure 3 and Eric Lundin for his help in creating Figures 1, 11, 4. Additionally we would like to thank Erik Rogers for providing the WW3 grid. Lastly, we'd like to acknowledge Paul Tol's note on color-blind friendly colormaps (Tol, 2021). This written work is authored by an employee of NTESS. The employee, not NTESS, owns the right, title and interest in and to the written work and is responsible for its contents. Any subjective views or opinions that might be expressed in the paper do not necessarily represent the views of the U.S. Department of Energy or the United States Government. The publisher acknowledges that the U.S. Government retains a non-exclusive, paid-up, irrevocable, world-wide license to publish or reproduce the published form of this written work or allow others to do so, for U.S. Government purposes. The DOE will provide public access to results of federally sponsored research in accordance with the DOE Public Access Plan.

References

Amante, C., & Eakins, B. W. (2009). *Etopo1 arc-minute global relief model: procedures, data sources and analysis* (Tech. Rep.). NOAA Technical Memorandum NESDIS NGDC-24. National Geophysical Data Center, NOAA. doi: https:\\doi.org\10.7289\V5C8276M

Aré, F. E. (1988a). Thermal abrasion of sea coasts (part i). *Polar Geography and Geology*, *12*(1), 1-1. Retrieved from https://doi.org/10.1080/10889378809377343 doi: https://doi.org/10.1080/10889378809377343

Aré, F. E. (1988b). Thermal abrasion of sea coasts (part ii). *Polar Geography and Geology*, *12*(2), 87-87. Retrieved from https://doi.org/10.1080/10889378809377352 doi: https://doi.org/10.1080/10889378809377352

Barnhart, K. R., Anderson, R. S., Overeem, I., Wobus, C., Clow, G. D., & Urban, F. E. (2014). Modeling erosion of ice-rich permafrost bluffs along the alaskan beaufort sea coast. *Journal of Geophysical Research: Earth Surface*, *119*(5), 1155-1179. Retrieved from https://agupubs.onlinelibrary.wiley.com/doi/abs/10.1002/2013JF002845 doi: https://doi.org/10.1002/2013JF002845

Barnhart, K. R., Overeem, I., & Anderson, R. S. (2014). The effect of changing sea ice on the physical vulnerability of arctic coasts. *The Cryosphere*, *8*(5), 1777–1799. doi: https://doi.org/10.5194/tc-8-1777-2014

Bayat, E., Bull, D., Frederick, J., Mota, A., & Tezaur, I. (2025). *Model output dataset and analysis scripts/tools used in the calibration of the arctic coastal erosion (ace) model at drew point, ak.* Zenodo. Retrieved from https://zenodo.org/doi/10.5281/zenodo.14920733 doi: 10.5281/ZENODO.14920733

Boelter, D. (1968). Important physical properties of peat materials. In *In: Proceedings, third internationalpeat congress; 1968 august 18-23; quebec, canada.[place of publication unknown]: Department of engery, minds and resources and national research council of canada: 150-154.*

Bristol, E. M., Connolly, C. T., Lorenson, T. D., Richmond, B. M., Ilgen, A. G., Choens, R. C., ... others (2020). *Geochemical characterization and material properties of coastal permafrost near drew point, alaska.* Environmental Data Initiative. doi: https://doi.org/10.6073/pasta/cc4d53a91ed873765224fcb6d09f5eb7

Bristol, E. M., Connolly, C. T., Lorenson, T. D., Richmond, B. M., Ilgen, A. G., Choens, R. C., ... others (2021). Geochemistry of coastal permafrost and erosion-driven organic matter fluxes to the beaufort sea near drew point, alaska. *Frontiers in Earth Science*, *8*, 598933. doi: https://doi.org/10.3389/feart.2020.598933

Bull, D., Bristol, E., Jones, B., Choens, R., Kanevskiy, M., Iwahana, G., ... McClelland, J. W. (2025). *Observational dataset from drew point, alaska used in the calibration of the arctic coastal erosion (ace) model.* Zenodo. Retrieved from https://zenodo.org/doi/10.5281/zenodo.14862274 doi: 10.5281/ZENODO.14862274

Bull, D. L., Bristol, E. M., Brown, E., Choens, R. C., Connolly, C. T., Flanary, C., ... others (2020). *Arctic coastal erosion: Modeling and experimentation* (Tech. Rep.). Sandia National Laboratories, Albuquerque, NM (United States); SAND2020-10223. doi: https://doi.org/10.2172/1670531

(C3S), C. C. C. S. (2017). *ERA5: Fifth generation of ECMWF atmospheric reanalyses of the global climate.* Copernicus Climate Change Service Climate Data Store (CDS), https://cds.climate.copernicus.eu.

Casas-Prat, M., & Wang, X. L. (2020). Projections of extreme ocean waves in the arctic and potential implications for coastal inundation and erosion. *Journal of Geophysical Research: Oceans*, *n/a*(n/a), e2019JC015745. Retrieved from https://agupubs.onlinelibrary.wiley.com/doi/abs/10.1029/2019JC015745 (e2019JC015745 2019JC015745) doi: https://doi.org/10.1029/2019JC015745

Cummings, J. A. (2005). Operational multivariate ocean data assimilation. *Quarterly*

Journal of the Royal Meteorological Society: A journal of the atmospheric sciences, applied meteorology and physical oceanography, *131*(613), 3583–3604. doi: https://doi.org/10.1256/qj.05.105

Cummings, J. A., & Smedstad, O. M. (2013). Variational data assimilation for the global ocean. In *Data assimilation for atmospheric, oceanic and hydrologic applications (vol. ii)* (pp. 303–343). Springer.

Danielson, S., Curchitser, E., Hedstrom, K., Weingartner, T., & Stabeno, P. (2011). On ocean and sea ice modes of variability in the bering sea. *Journal of Geophysical Research: Oceans*, *116*(C12). doi: https://doi.org/10.1029/2011JC007389

Danielson, S., Johnson, M., Solomon, S., & Perrie, W. (2008). 1 km gridded bathymetric dataset based on ship soundings: a research tool for the waters of eastern russia, alaska, & western canada. In *Poster presentation at the 2008 alaska marine science symposium, anchorage, alaska.*

Danielson, S. L., Dobbins, E. L., Jakobsson, M., Johnson, M. A., Weingartner, T., Williams, W., & Zarayskaya, Y. (2015). Sounding the northern seas. *Eos*, *96*(10.1029). Retrieved from `https://sciencesprings.wordpress.com/2015/12/29/from-eos-sounding-the-northern-seas/`

Darrow, M. (2011). Thermal modeling of roadway embankments over permafrost. *Cold Regions Science and Technology*, *65*, 474–487. doi: https://doi.org/10.1016/j.coldregions.2010.11.001

Darrow, M., Huang, S., & Akagawa, S. (2009). Adsorbed cation effects on the frost susceptibility of natural soils. *Cold Regions Science and Technology*, *55*, 263–277. doi: https://doi.org/10.1016/j.coldregions.2008.08.002

Darrow, M. M. (2011). Thermal modeling of roadway embankments over permafrost. *Cold Regions Science and Technology*, *65*, 474–487. doi: https://doi.org/10.1016/j.coldregions.2010.11.001

Deltares. (2018a). *Delft3d-flow: Simulation of multi-dimensional hydrodynamic flows and transport phenomena, including sediments: User manual* (Tech. Rep.). Deltares, The Netherlands.

Deltares. (2018b). *Delft3d-wave: Simulation of short-crested waves with swan: User manual* (Tech. Rep.). Deltares, The Netherlands.

developed by the US Naval Research Laboratory, G. O. F. S. (2017). *GOFS3.1: a navy ocean/ice nowcasting and forecasting capability based on the hybrid coordinate ocean model (hycom), two-way coupled to the community ice code (cice) and using the navy coupled ocean data assimilation (ncoda).* https://www.hycom.org/dataserver/gofs-3pt1/analysis.

Frederick, J., Mota, A., Tezaur, I., & Bull, D. (2021). A thermo-mechanical terrestrial model of arctic coastal erosion. *Journal of Computational and Applied Mathematics*, *397*, 113533. Retrieved from `https://www.sciencedirect.com/science/article/pii/S0377042721001527` doi: https://doi.org/10.1016/j.cam.2021.113533

Gibbs, A., Ohman, K., & Richmond, B. (2015). *National assessment of shoreline change: a gis compilation of vector shorelines and associated shoreline change data for the north coast of alaska, u.s.-canadian border to icy cape.* USGS Open-File Report 2015-1048. doi: https://doi.org/10.3133/ofr20151030

Gibbs, A. E., Erikson, L. H., Jones, B. M., Richmond, B. M., & Engelstad, A. C. (2021). Seven decades of coastal change at barter island, alaska: exploring the importance of waves and temperature on erosion of coastal permafrost bluffs. *Remote Sensing*, *13*(21), 4420. doi: https://doi.org/10.3390/rs13214420

Gnatowski, T. (2016). *Thermal properties of degraded lowland peat-marsh soils, EPSC2016-8105.* EGU General Assembly 2016, April 17-22, 2016, Vienna, Austria.

Guégan, E. B., & Christiansen, H. H. (2017). Seasonal arctic coastal bluff dynamics in adventfjorden, svalbard. *Permafrost and Periglacial Processes*, *28*(1), 18–31. doi: https://doi.org/10.1002/ppp.1891

Günther, F., Overduin, P. P., Sandakov, A. V., Grosse, G., & Grigoriev, M. N. (2013). Short- and long-term thermo-erosion of ice-rich permafrost coasts in the laptev sea region. *Biogeosciences*, *10*(6), 4297–4318. Retrieved from https://bg.copernicus.org/articles/10/4297/2013/ doi: https://doi.org/10.5194/bg-10-4297-2013

Günther, F., Overduin, P. P., Yakshina, I. A., Opel, T., Baranskaya, A. V., & Grigoriev, M. N. (2015). Observing muostakh disappear: permafrost thaw subsidence and erosion of a ground-ice-rich island in response to arctic summer warming and sea ice reduction. *The Cryosphere*, *9*(1), 151–178. doi: https://doi.org/10.5194/tc-9-151-2015

Himmelstoss, E. A., Henderson, R. E., Kratzmann, M. G., & Farris, A. S. (2018). *Digital shoreline analysis system (dsas) version 5.0 user guide* (Tech. Rep.). US Geological Survey. doi: https://doi.org/10.3133/ofr20181179

Hinkel, K., Eisner, W., Bockheim, J., Nelson, F., Peterson, K., & Dai, X. (2003). Spatial extent, age, and carbon stocks in drained thaw lake basins on the barrow peninsula, alaska. *Arctic, Antarctic, and Alpine Research*, *35*(5), 291–300. doi: https://doi.org/10.1657/1523-0430(2003)035[0291:SEAACS]2.0.CO;2

Holthuijsen, L. (2007). *Waves in oceanic and coastal waters*. Cambridge: Cambridge University Press.

Holthuijsen, L., Booij, N., & Ris, R. (1993). A spectral wave model for the coastal zone. In *Ocean wave measurement and analysis* (pp. 630–641).

Hoque, A., & Pollard, W. (2009). Arctic coastal retreat through block failure. *Canadian Geotechnical Journal*, *46*(10), 1103-1115. Retrieved from https://doi.org/10.1139/T09-058 doi: 10.1139/T09-058

Hoque, A., & Pollard, W. (2016). Stability of permafrost dominated coastal cliffs in the arctic. *Polar Science*, *10*(1), 79 - 88. Retrieved from http://www.sciencedirect.com/science/article/pii/S1873965215300177 doi: https://doi.org/10.1016/j.polar.2015.10.004

Hughes, T. (1987). *The finite element method: Linear static and dynamic finite element analysis*. Prentice Hall.

Irrgang, A., Bendixn, M., Farquharson, L., Baranskaya, A., Erikson, L., Gibbs, A., ... Jones, B. (2022). Drivers, dynamics and impacts of changing arctic coasts. *Nature Reviews Earth and Environment*, *3*, 39–54. doi: https://doi.org/10.1038/s43017-021-00232-1

Islam, M. A., & Lubbad, R. (2022). A process-based model for arctic coastal erosion driven by thermodenudation and thermoabrasion combined and including nearshore morphodynamics. *Journal of Marine Science and Engineering*, *10*(11). Retrieved from https://www.mdpi.com/2077-1312/10/11/1602 doi: https://doi.org/10.3390/jmse10111602

Iwahana, G., Cooper, Z. S., Carpenter, S. D., Deming, J. W., & Eicken, H. (2021). Intra-ice and intra-sediment cryopeg brine occurrence in permafrost near utqiaġvik (barrow). *Permafrost and Periglacial Processes*, *32*(3), 427–446. doi: https://onlinelibrary.wiley.com/doi/10.1002/ppp.2101

Jones, B., Arp, C. D., Beck, R. A., Grosse, G., Webster, J. M., & Urban, F. E. (2009). Erosional history of cape halkett and contemporary monitoring of bluff retreat, beaufort sea coast. *Alaska Polar Geogr.*, *32*, 129–142. doi: https://doi.org/10.1080/10889370903486449

Jones, B. M., Arp, C. D., Jorgenson, M. T., Hinkel, K. M., Schmutz, J. A., & Flint, P. L. (2009). Increase in the rate and uniformity of coastline erosion in arctic alaska. *Geophysical Research Letters*, *36*(3). Retrieved from https://agupubs.onlinelibrary.wiley.com/doi/abs/10.1029/2008GL036205 doi: https://doi.org/10.1029/2008GL036205

Jones, B. M., Farquharson, L. M., Baughman, C. A., Buzard, R. M., Arp, C. D., Grosse, G., ... Romanovsky, V. E. (2018, 10). A decade of remotely sensed observations highlight complex processes linked to coastal permafrost bluff

erosion in the arctic. *Environmental Research Letters*, *13*(11), 115001. Retrieved from https://dx.doi.org/10.1088/1748-9326/aae471 doi: https://doi.org/10.1088/1748-9326/aae471

Jones, M., Grosse, G., Jones, B., & Walter Anthony, K. (2012). Peat accumulation in drained thermokarst lake basins in continuous, ice-rich permafrost, northern seward peninsula, alaska. *J. Geophys. Res.: Biogeo.*, *117*. doi: https://doi.org/10.1029/2011JG001766

Jorgenson, M., & Brown, J. (2005). Classification of the alaskan beaufort sea coast and estimation of carbon and sediment inputs from coastal erosion. *Geo-Marine Letters*, *25*, 69–80. doi: https://doi.org/10.1007/s00367-004-0188-8

Kanevskiy, M., Shur, Y., Jorgenson, M., Ping, C.-L., Michaelson, G., Fortier, D., ... Tumskoy, V. (2013). Ground ice in the upper permafrost of the beaufort sea coast of alaska. *Cold Regions Science and Technology*, *85*, 56-70. Retrieved from https://www.sciencedirect.com/science/article/pii/S0165232X12001644 doi: https://doi.org/10.1016/j.coldregions.2012.08.002

Kobayashi, N. (1985). Formation of thermoerosional niches into frozen bluffs due to storm surges on the beaufort sea coast. *Journal of Geophysical Research: Oceans*, *90*(C6), 11983–11988. doi: https://doi.org/10.1029/JC090iC06p11983

Kobayashi, N., Vidrine, J., Nairn, R., & Soloman, S. (1999). Erosion of frozen cliffs due to storm surge on beaufort sea coast. *Journal of coastal research*, 332–344. Retrieved from https://www.jstor.org/stable/4298946

Kruse, A., & Darrow, M. (2017). Adsorbed cation effects on unfrozen water in fine-grained frozen soil measured using pulsed nuclear magnetic resonance. *Cold Regions Science and Technology*, *142*, 42–54. doi: 10.1016/j.coldregions.2017.07.006

Lantuit, H., Atkinson, D., Paul Overduin, P., Grigoriev, M., Rachold, V., Grosse, G., & Hubberten, H.-W. (2011). Coastal erosion dynamics on the permafrost-dominated bykovsky peninsula, north siberia, 1951–2006. *Polar Research*, *30*(1), 7341. doi: https://doi.org/10.3402/polar.v30i0.7341

Lantuit, H., Overduin, P. P., Couture, N., Wetterich, S., Aré, F., Atkinson, D., ... Vasiliev, A. (2012). The arctic coastal dynamics database: A new classification scheme and statistics on arctic permafrost coastlines. *Estuaries and Coasts*, *35*(2), 383–400. Retrieved 2023-08-28, from http://www.jstor.org/stable/41486638

Lee, E. (1969). Elastic-plastic deformation at finite strains. *J. Appl. Mech.*, *36*(1), 1–6. doi: https://doi.org/10.1115/1.3564580

Li, X., Wen, H., Muhunthan, B., & Wang, J. (2015). Modeling and prediction of the effects of moisture on the unconfined compressive and tensile strength of soils. *Journal of Geotechnical and Geoenvironmental Engineering*, *141*(7), 04015028. doi: https://doi.org/10.1061/(ASCE)GT.1943-5606.0001308

Li, X., Yan, Y., & Ji, S. (2022). Mechanical properties of frozen ballast aggregates with different ice contents and temperatures. *Construction and Building Materials*, *317*, 125893. doi: https://doi.org/10.1016/j.conbuildmat.2021.125893

Liu, Q., Babanin, A. V., Zieger, S., Young, I. R., & Guan, C. (2016). Wind and wave climate in the arctic ocean as observed by altimeters. *Journal of Climate*, *29*(22), 7957–7975. doi: https://doi.org/10.1175/JCLI-D-16-0219.1

Marsden, J., & Ratiu, T. (1999). *Introduction to mechanics and symmetry: A basic exposition of classical mechanical systems*. Springer-Verlag, New York.

Mentaschi, L., Vousdoukas, M. I., Pekel, J.-F., Voukouvalas, E., & Feyen, L. (2018). Global long-term observations of coastal erosion and accretion. *Scientific reports*, *8*(1), 12876. doi: https://doi.org/10.1038/s41598-018-30904-w

Moon, T. A., Thoman, R., Druckenmiller, M., Ahmasuk, B., Backensto, S. A., Ballinger, T. J., ... others (2023). The arctic. *Bulletin of the American Meteorological Society*, *104*(9), S271–S321. doi: https://doi.org/10.1175/BAMS-D-23-0079.1

Mota, A., Knap, J., & Ortiz, M. (2008). Fracture and fragmentation of simplicial finite element meshes using graphs. *International Journal for Numerical Methods in Engineering*, *73*(11), 1547-1570. Retrieved from `https://onlinelibrary.wiley.com/doi/abs/10.1002/nme.2135` doi: https://doi.org/10.1002/nme.2135

Mota, A., Tezaur, I., & Alleman, C. (2017). The Schwarz alternating method. *Comput. Meth. Appl. Mech. Engng.*, *319*, 19–51. doi: https://doi.org/10.1016/j.cma.2017.02.006

Mota, A., Tezaur, I., & Phlipot, G. (2020). The Schwarz alternating method for transient solid dynamics. *Comput. Meth. Appl. Mech. Engng. (under review)*.

Nederhoff, K., Erikson, L., Engelstad, A., Bieniek, P., & Kasper, J. (2022). The effect of changing sea ice on wave climate trends along alaska's central beaufort sea coast. *The Cryosphere*, *16*(5), 1609–1629. Retrieved from `https://tc.copernicus.org/articles/16/1609/2022/` doi: https://doi.org/10.5194/tc-16-1609-2022

Newmark, N. M. (1959). A method of computation for structural dynamics. *Journal of the Engineering Mechanics Division*, *85*(3), 67-94. Retrieved from `https://ascelibrary.org/doi/abs/10.1061/JMCEA3.0000098` doi: https://doi.org/10.1061/JMCEA3.0000098

Nicolsky, D. J., Romanovsky, V. E., Panda, S. K., Marchenko, S. S., & Muskett, R. R. (2017). Applicability of the ecosystem type approach to model permafrost dynamics across the alaska north slope. *Journal of Geophysical Research: Earth Surface*, *122*(1), 50–75. doi: https://doi.org/10.1002/2016JF003852

Nielsen, D. M., Pieper, P., Barkhordarian, A., Overduin, P., Ilyina, T., Brovkin, V., ... Dobrynin, M. (2022). Increase in arctic coastal erosion and its sensitivity to warming in the twenty-first century. *Nature Climate Change*, *12*(3), 263–270. doi: https://doi.org/10.1038/s41558-022-01281-0

O'Conner, M., Cardenas, M., Ferencz, S., Wu, Y., Neilson, B., Chen, J., & Kling, G. (2020). Empirical models for predicting water and heat flow properties of permafrost soils. *Geophysical Research Letters*, *47*(11). doi: https://doi.org/10.1029/2020GL087646

Overeem, I., Anderson, R. S., Wobus, C. W., Clow, G. D., Urban, F. E., & Matell, N. (2011). Sea ice loss enhances wave action at the arctic coast. *Geophysical Research Letters*, *38*(17). doi: https://doi.org/10.1029/2011GL048681

Partenscky, H.-W. (1988). *Dynamic forces due to waves breaking at vertical coastal structures.* 21st International Conference on Coastal Engineering, June 20-25, Costa del Sol-Malaga, Spain.

Petrovic, J. (2003). Review mechanical properties of ice and snow. *Journal of materials science*, *38*, 1–6. doi: https://doi.org/10.1023/A:1021134128038

Pribyl, D. W. (2010). A critical review of the conventional soc to som conversion factor. *Geoderma*, *156*(3-4), 75–83. doi: https://doi.org/10.1016/j.geoderma.2010.02.003

Rantanen, M., Karpechko, A. Y., Lipponen, A., Nordling, K., Hyvärinen, O., Ruosteenoja, K., ... Laaksonen, A. (2022). The arctic has warmed nearly four times faster than the globe since 1979. *Communications Earth & Environment*, *3*(1), 168. doi: https://doi.org/10.1038/s43247-022-00498-3

Ravens, T. M., Jones, B. M., Zhang, J., Arp, C. D., & Schmutz, J. A. (2012). Process-based coastal erosion modeling for Drew Point, North Slope, Alaska. *Journal of Waterway, Port, Coastal, and Ocean Engineering*, *138*(2), 122–130. doi: https://doi.org/10.1061/(ASCE)WW.1943-5460.0000106

Rehman, Z. u., Khalid, U., Farooq, K., & Mujtaba, H. (2018). On yield stress of compacted clays. *International Journal of Geo-Engineering*, *9*, 1–16. doi: https://doi.org/10.1186/s40703-018-0090-2

Rezanezhad, F., Price, J. S., Quinton, W. L., Lennartz, B., Milojevic, T., & Van Cappellen, P. (2016). Structure of peat soils and implications for water

storage, flow and solute transport: A review update for geochemists. *Chemical Geology*, *429*, 75–84. doi: https://doi.org/10.1016/j.chemgeo.2016.03.010

Robertson, E. C. (1988). *Thermal properties of rocks.* U.S. Geological Survey Open-File Report 88-441.

Rogers, W., & Zieger, S. (2014). New wave-ice interaction physics in wavewatch iii®. In *Proc. 22nd iahr intl. symp. on ice.*

Salinger, A. G., Bartlett, R. A., Bradley, A. M., Chen, Q., Demeshko, I. P., Gao, X., ... others (2016). Albany: using component-based design to develop a flexible, generic multiphysics analysis code. *International Journal for Multiscale Computational Engineering*, *14*(4), 415–438. doi: https://doi.org/10.1615/IntJMultCompEng.2016017040

Service, N. N. O. (2019). *Prudhoe Bay, AK - Station ID: 9497645: The prudhoe bay station is part of the water level observation network and collects meteorological observations, water temperature, and conductivity data.* https://tidesandcurrents.noaa.gov/stationhome.html?id=9497645.

Smith, S. L., O'Neill, H. B., Isaksen, K., Noetzli, J., & Romanovsky, V. E. (2022). The changing thermal state of permafrost. *Nature Reviews Earth & Environment*, *3*(1), 10–23. doi: https://doi.org/10.1038/s43017-021-00240-1

Thomas, M. A., Mota, A., Jones, B. M., Choens, R. C., Frederick, J. M., & Bull, D. L. (2020). Geometric and material variability influences stress states relevant to coastal permafrost bluff failure. *Frontiers in Earth Science*, *8*, 143. doi: https://doi.org/10.3389/feart.2020.00143

Thomson, J., & Rogers, W. E. (2014). Swell and sea in the emerging arctic ocean. *Geophysical Research Letters*, *41*(9), 3136–3140. doi: https://doi.org/10.1002/2014GL059983

Tol, P. (2021, August). *Paul tol's notes - color schemes.* `https://personal.sron.nl/~pault/`.

UNESCO. (1983). Algorithms for the computation of fundamental properties of seawater. *UNESCO Technical Papers in Marine Science*, *44*, 1–55.

University of Alaska Fairbanks Institute of Northern Engineering, U. A. C. o. E. C. R. R., U.S. Army Corps of Engineers Alaska District, & Laboratory, E. (2019). *Statewide threat assessment: Identification of threats from erosion, flooding, and thawing permafrost in remote alaska communities* (Tech. Rep. No. INE 19.03). Denali Commission. Retrieved from `https://www.denali.gov/wp-content/uploads/2019/11/Statewide-Threat-Assessment-Final-Report-20-November-2019.pdf`

Urban, F. (2021). *Data release associated with data series - doi/gtn-p climate and active-layer data acquired in the national petroleum reserve-alaska and the arctic national wildlife refuge, 1998-2019 (ver. 3.0, march 2021)* [Data Release]. U.S. Geological Survey data release. doi: https://doi.org/10.5066/F7VX0FGB

Urban, F., & Clow, G. (2018). *Doi/gtn-p climate and active-layer data acquired in the national petroleum reserve–alaska and the arctic national wildlife refuge, 1998–2017 (ver. 1.2, july 2021)* (Data Series No. 1092). U.S. Geological Survey. doi: https://soi.org10.3133/ds1092

Walker, H. (1988). Permafrost and coastal processes. In *Proceedings of the fifth international conference on permafrost* (Vol. 3, pp. 35–42).

Wan, X., & Yang, Z. (2020). Pore water freezing characteristic in saline soils based on pore size distribution. *Cold Regions Science and Technology*, *173*. doi: https://doi.org/10.1016/j.coldregions.2020.103030

Wang, M., & Overland, J. E. (2015). Projected future duration of the sea-ice-free season in the alaskan arctic. *Progress in Oceanography*, *136*, 50–59. doi: https://doi.org/10.1016/j.pocean.2015.01.001

Ward Jones, M. K., Jones, B. M., Nitze, I., Gessner, M., Grosse, G., Bartsch, A., & Bull, D. (To be Submitted). Assessing annual and sub-seasonal dynamics of a rapidly eroding coastline along the beaufort sea coast in northern alaska. *To be*

submitted to Scientific Reports.

Westermann, S., Schuler, T., Gisnås, K., & Etzelmüller, B. (2013). Transient thermal modeling of permafrost conditions in southern norway. *The Cryosphere*, *7*(2), 719–739. doi: https://doi.org/10.5194/tc-7-719-2013

Wobus, C., Anderson, R., Overeem, I., Matell, N., Clow, G., & Urban, F. (2011). Thermal erosion of a permafrost coastline: Improving process-based models using time-lapse photography. *Arctic, Antarctic, and Alpine Research*, *43*(3), 474–484. doi: https://doi.org/10.1657/1938-4246-43.3.474

(WW3DG), W. I. D. G. (2019). *User manual and system documentation of wavewatch iii® version 6.07. tech. note 333* (Tech. Rep.). NOAA/NWS/NCEP/MMAB College Park, MD, USA.

Supporting Information for "The Arctic Coastal Erosion Model: Overview, Developments, and Calibration at Drew Point, Alaska"

Elyce Bayat[1], Diana L. Bull[1], Jennifer M. Frederick[1], Alejandro Mota[2], Benjamin M. Jones[3], Irina Tezaur[2], Christopher Flanary[5], Emily M. Bristol[4], Melissa Ward Jones[3], Robert C. Choens[1], , Craig A. Jones[5]

[1]Sandia National Laboratories, Albuquerque, NM, USA

[2]Sandia National Laboratories, Livermore, CA, USA

[3]University of Alaska, Fairbanks, AK, USA

[4]University of Texas at Austin, Port Aransas, TX, USA

[5]Integral Consulting Inc., Santa Cruz, CA, USA

Contents of this file

Additional Supporting Information (Files uploaded separately)

1. Movies S1 to S2

February 25, 2025, 7:36am

Text S1. As mentioned in Section 3.3.1 of the main text, both spatial and temporal processing of water level data output from the oceanographic model components is required in order to utilize the data as boundary condition inputs for the terrestrial model. Denoting the original water level data as $w(t)$, the goal is to generate a new signal for time-varying water level $w_{\text{terr}}(t)$ sampled at the same spatial and temporal discretization as used by the terrestrial model, in a way that ensures that water is contacting a bluff elevation for the entirety of the time step used by the terrestrial model. It could be that a given elevation is contacted four distinct times, each with a unique duration, to achieve that final duration of contact equal to the terrestrial model time-step. But if over an hour, the noted update rate for the wave spectrum in Section 3.1, a the duration of contact for a given elevation is less than the time-step that elevation will not be included in $w_{\text{terr}}(t)$. Hence, this processing seeks to evaluate the *cumulative duration* of water contact with the bluff per elevation of the original $w(t)$ over each hour and ensure cumulative duration's are integer numbers of the terrestrial time-step.

For understanding the procedure, let us first consider the following notations:

- $w(t)$ is the time-varying water level provided by the oceanographic model, sampled on the time discretization of Δt_{wave} (in this case, 2 Hz, or 0.5 seconds).
- Δt_{terr} is the time step used by the terrestrial model.
- Δz_{terr} is the spatial discretization used by the terrestrial model, resulting in discrete elevations along the bluff z_i.
- $w_{\text{terr}}(t)$ is the new water level signal we seek to generate, sampled on Δt_{terr} spatially and Δt_{wave} temporally.

To generate this new signal, the following steps are taken, as shown in Algorithm 1. First, the water level $w(t)$, which can take on a continuous value spatially, is sampled onto discrete z_i consistent with terrestrial grid using a center-binning approach (**STEP 1**). Next, the cumulative duration of water level contact with each z_i is computed, as this is the quantity we seek to evaluate when generating the new signal (**STEP 2**). Then, the cumulative duration of water level contact per z_i is sampled on the terrestrial time step Δt_{terr} in a way that best preserves the duration per z_i (**STEP 3**). This requires finding and representing durations of contact as the largest integer number of terrestrial time steps Δt_{terr} for which a given z level z_i is entirely "exposed" to water. For durations that do not evenly divide into an integer number of Δt_{terr}, the remainder is "carried over" to the next largest z_i (i.e. for $\Delta z_{\text{terr}} = 0.1$, leftover durations at $z = 0.8$ are passed to the count for $z = 0.7$, etc.). The rationale behind this logic is that if water was in contact with $z = 0.8$ it was also in contact with $z = 0.7$. Lastly, the new $w_{\text{terr}}(t)$ signal, now sampled appropriately on a Δz_{terr}, Δt_{terr} discretization, is generated (**STEP 4**). This is done by creating an $w_{\text{terr}}(t)$ for which the number of z_i values in the signal reflect appropriate durations in a given time block, as calculated in the previous step.

Algorithm 1: Algorithm for generating wave exposure history used in terrestrial model boundary conditions

```
Given: w(t), Δt_wave, Δt_terr, Δz_terr, z_i
// Array that will hold the new, processed water level data
w_terr = [];
// Loop over each distinct new wave spectrum, which is updated in hourly blocks

for block b in num_spectrum_time_blocks do
    // Perform processing for times in each new updated wave spectrum

    for time t_n in time block b do
        → STEP 1
        // Count the number of times the water level "contacts" a given z_i on the terrestrial grid
        num_contacts_per_z = zeros(size(z_locations_terr))

        for z_i in z_locations_terr do

            if ((z_i − Δz_terr/2) ≤ w(t_n) < (z_i + Δz_terr/2) ) then
                num_contacts_per_z(i) = num_contacts_per_z(i) + 1 ;

            end

        end
        → STEP 2
        // Convert this frequency of contacts over a time block into a total duration of
        // contact during the time block
        duration_per_z_level = num_contacts_per_z * Δt_wave
        → STEP 3
        num_dt_terr_exposed_per_z = zeros(size(z_locations_terr))

        for z_i in sort(z_locations_terr, 'ascend') do
            num_dt_terr_exposed_per_z(i) = floor(duration_per_z_level(i)/Δt_terr)
            duration_carryover = mod(duration_per_z_level(i)/Δt_terr)
            duration_per_z_level(i-1)= duration_per_z_level(i-1) + duration_carryover

        end
        → STEP 4
        // Create an array of water heights that
        // contains an appropriate number of counts per z level
        w_tmp = []

        for z_i in z_locations_terr do

            for n in num_dt_terr_exposed_per_z(i) do
                w_tmp.append(z_i)

            end

        end
        // Now, randomly shuffle them to create
        // new water height signal during this time block
        w_terr_block = random.shuffle(w_tmp)
        // Finally, concatenate the new signal for this block
        // with the array holding the overall new signal for all times
        w_terr = concat(w_terr, w_terr_block)

    end

end
```

Text S2. This text accompanies Figure S1 in describing the large parameter sweep conducted on the minimum allowable elastic moduli E_{m} and $E_{\mathrm{m,o}}$ to understand the interaction between these two parameters and resulting influence on erosion behavior. In particular, this study served as a first stage in the calibration process to determine appropriate parameter values/ranges for best matching observational thermo-denudation.

As discussed in Section 5.2.2 of the main text, the tensile yield value σ_{tol} was held at a large static value of 1000 MPa to effectively deactivate the tensile yield criterion (and by extension, prevent any block collapse) while sensitivity of thermo-denudation and niche formation were studied simultaneously by varying E_{m} and $E_{\mathrm{m,o}}$ respectively. E_{m} was simulated for the following values, all in Pa: 0.75×10^4, 0.8×10^4, 0.9×10^4, 1.0×10^4, 1.1×10^4, 1.2×10^4, 1.3×10^4, 1.4×10^4, 1.5×10^4, and 1.6×10^4. $E_{\mathrm{m,o}}$ was simulated as a fraction of E_{m} ($\frac{E_{\mathrm{m}}}{E_{\mathrm{m,o}}}$) for the following values: 1, 250, 500, 700, 800, 900, 1100, 1300, 1500, and 2000. Figure S1 illustrates a subset of these simulations with each panel representing a distinction combination of E_{m} (increasing towards the right along the columns) and $E_{\mathrm{m,o}}$ (increasing as descending down the rows). It is noted that due to either runaway erosion or computational limits, not all simulations in this larger exploratory study were run to full completion.

As in Figure 15 in the main text, within each panel: observed erosion measurements are shown with the time-lapse camera (dashed black line) and 12 AUV transects (gray markers); simulated rates of erosion are shown as a function of elevation through distinctly colored lines; and grey shading indicates periods of ocean storms, blue hatched shading corresponds to the time period of warming thermistor sensors (red lines in main text Figure 14 in the main text, and the horizontal green dashed line indicates the thermistor

location. A simulation calibrated for E_{m} is one in which high elevations match the dashed black line and low elevations approach and then surpass the green dashed line within the blue shading. Ice-bonded sediment material stiffness is increased as one moves down and to the right across the panels.

The description and patterns for Figure 15 in the main text are also valid here. The third column, $E_{\mathrm{m}} = 1.1e4$ Pa, possesses the desired niche evolution behavior (outside of the last row) as the $z = 0, 0.25$, and 0.5 m elevations intersect the green line within the blue hatched shading. Within that third column the second and third rows ($E_{\mathrm{m,o}} = 22$ Pa in the second row and 44 Pa in the third row) possess thermo-denudation with the desired characteristics as $z = 4.5, 4.0$, and 3.5 m all closely track the time-lapse camera observed denudation. This subset of the full sensitivity sweep highlights how it was possible to select a constant $E_{\mathrm{m}} = 1.1e4$ Pa for use in the selection of the tensile yield strength.

Text S3. This text accompanies Figure S2 in describing the larger parameter sweep conducted on σ_{tol} and $E_{\mathrm{m,o}}$ when calibrating for thermo-abrasion which best matched observational data. This is discussed in Section 5.2.3 of the main text with a subset of these panels shown in Figure 16. The interaction between niche geometry and accumulated tensile stress governing block failure was studied by varying the tensile yield σ_{tol} and minimum ocean-contacted elastic modulus $E_{\mathrm{m,o}}$ for a static and calibrated value of minimum elastic modulus $E_{\mathrm{m}} = 1.1 \times 10^4$ Pa. $E_{\mathrm{m,o}}$ values of 55.0, 110.0, 220.0, 550.0 Pa were paired with σ_{tol} magnitudes informed by the simulations shown in Figure S1. The magnitude of tensile stress was evaluated near the ice wedge on Sept. 01, 2018. This evaluation revealed 1.2×10^5, 1.3×10^5, 1.4×10^5, and 1.5×10^5 Pa as the appropriate range over which σ_{tol} should be varied. Figure S2 shows all of the simulated ranges with increasing σ_{tol} along the columns and increasing $E_{\mathrm{m,o}}$ along the rows.

While the final calibrated values for $E_{\mathrm{m,o}}$ and σ_{tol} were selected as $E_{\mathrm{m,o}} = 220$, $\sigma_{\mathrm{tol}} = 1.4 \times 10^5$, the next best candidate out of this set was identified as $E_{\mathrm{m,o}} = 550$, $\sigma_{\mathrm{tol}} = 1.4 \times 10^5$, which produces very similar performance in upper bluff thermo-denudation, and achieves a block collapse closer to the observed date. The rationale behind selecting $E_{\mathrm{m,o}} = 220$ Pa came from examining the difference in the overall bluff geometry between the two cases. Two key elements of the geometry are considered: 1) depth of niche, 2) stratification of erosion along the bluff face. A deeper niche is obtained for the $E_{\mathrm{m,o}} = 220$ Pa case as opposed to the $E_{\mathrm{m,o}} = 550$ Pa case slightly elevating it as the most preferred. Additionally, evaluation of $z = 1.0, 2.0, 3.0$ m shows that they have more erosion for $E_{\mathrm{m,o}} = 220$ Pa; again slightly elevating it as more preferred. In any case, both produce

very good results, which suggests that selections for $E_{\mathrm{m,o}}$ within this value range $220-550$ are appropriate.

Text S4. This text accompanies Figures S3, S4, S5 in discussion around the comparison between modeled and observed ground temperature thermal evolution.

Figure S4 showcases the thermal diffusivity ($\alpha = k/(\rho C_p)$ of pure ice (cyan), pure water (blue), and ice-bonded sediment (purple, green, yellow, pink) at varying levels of ice saturation f. The α presented for ice-bonded sediment is calculated using the thermal mixture models and constituent material characterization data presented in the main text (Figures 5 and 9 in the main text). Pure ice has a higher thermal diffusivity than the considered ice-bonded sediment for all ice saturation except fully frozen ($f = 1.0$), and so we expect that modeled pure ice will have a faster thermal evolution compared to ice-bonded sediment.

Figure S3 shows a ground temperature comparison between modeled ice wedge and observational probes (USGS probe and vertical thermistor string) varying with both (a) elevation and (b-c) in time. When comparing Figure S3 with Figure 17 of the main text, it is clear that the modeled ice wedge has a different thermal evolution than the modeled ice-bonded sediment, with the modeled ice better matching the probe data due to its faster thermal evolution. This comparison between modeled ice and ice-bonded sediment serves as a good confirmation that the presented model produces expected differential response to thermal material properties provided.

Figure S5 shows (a) ice saturation and (b) thermal diffusivity for the modeled ice-bonded sediment varying with elevation for select dates. Examining both at elevations ~ 3 m, a drop in ice saturation from fully frozen ($f = 1.0$) to partially thawed ($f \sim 0.8$) can be seen, with a corresponding decrease in thermal diffusivity. In the comparison of temperatures between modeled ice-bonded sediment and observational probes discussed

in the main text (Figure 17), the largest differences between modeled and observed were at elevations of $\sim 2 - 4.75$ m. If the model is biased towards thawing material prematurely, this could result in a lowered thermal diffusivity and in a consequent slower thermal evolution compared to the observed.

Movie S1. Animation of the final calibrated simulation from July 1 to September 8 2018, showing mesh erosion over time in three columns displaying profiles for temperature (left), ice saturation (middle), and mesh erosion failure indicators (right). Failure indicator values' proximity to one represents how close an element is to meeting removal by that criterion. The right column shows failure indicators for the strain criterion (mainly active at the bluff face) and tensile yield criterion (increasing over time at the back left corner of the ice-bonded sediment). Legends for all three fields are shown on the bottom of each column.

Movie S2. Animation of block failure for the final calibrated simulation on September 3 2018 with the tensile and strain failure indicators shown. Failure indicator values' proximity to one represents how close an element is to meeting removal by that criterion. The entire animation covers $\sim$ 45 minutes, with the actual block failure occurring over 4 seconds. During block failure, the tensile indicators at the back left corner near the ice-wedge can be seen approaching 1 (dark red) and precedes the crack which travels towards the vertex of the niche. Once the crack has traveled the entirety of the elevation, the remaining material is removed via the kinematic erosion criteria.

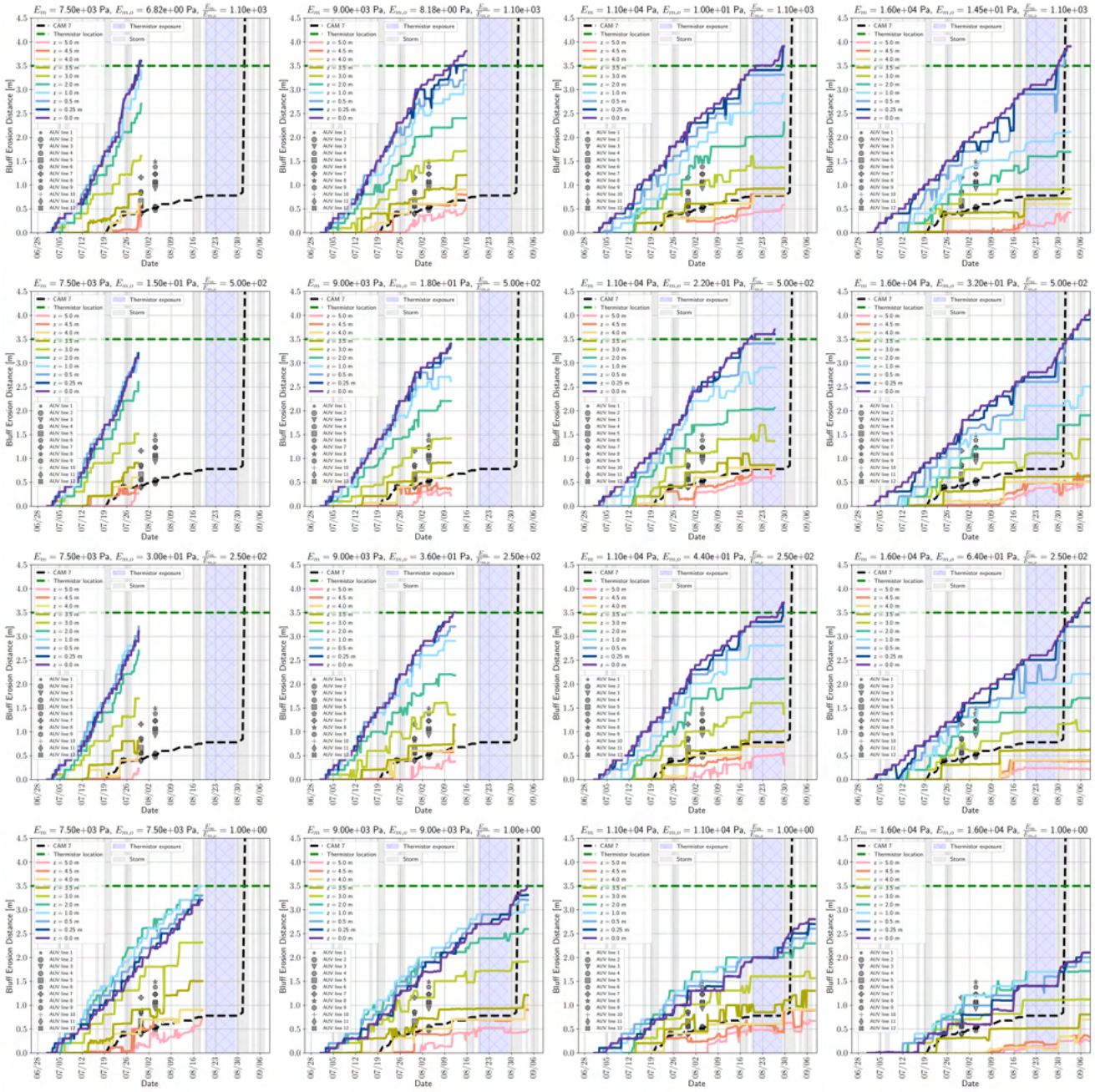

Figure S1. Results of larger exploratory parameter sweep on E_{m} and $E_{\mathrm{m,o}}$ during which σ_{tol} was held artificially high to deactivate tensile yield. Values of E_{m} increase from left to right, while values of $E_{\mathrm{m,o}}$ increase from top to bottom. As the initial study was done varying the fractional relationship $\frac{E_{\mathrm{m}}}{E_{\mathrm{m,o}}}$, each row possesses a distinct value of $\frac{E_{\mathrm{m}}}{E_{\mathrm{m,o}}}$ rather than $E_{\mathrm{m,o}}$. Material is most compliant in the upper left, and increases in stiffness as we move down and right across the plots.

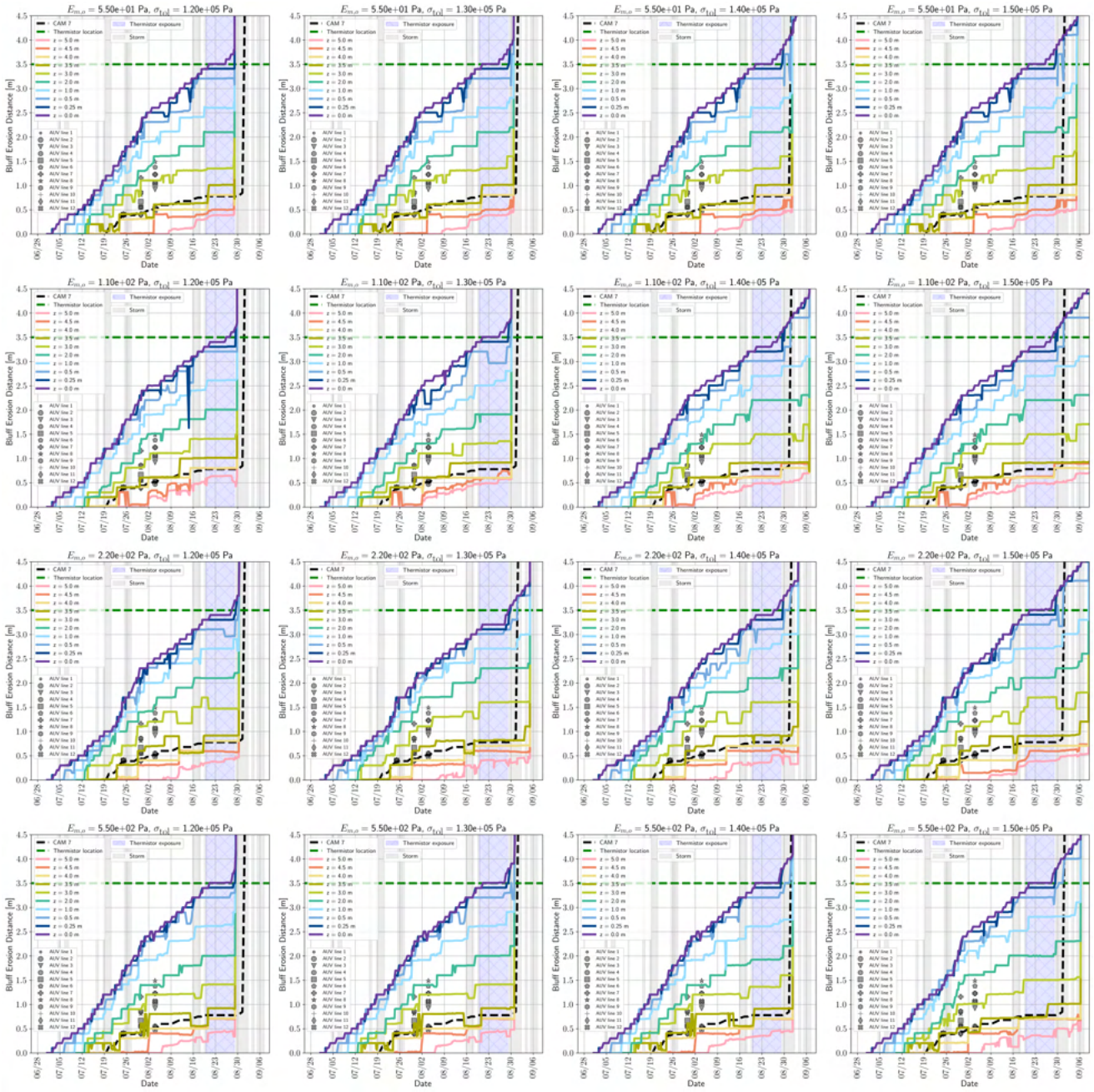

Figure S2. Results of larger parameter sweep on σ_{tol} and $E_{\mathrm{m,o}}$ used to identify combination of these values that best matched the combination of target niche geometry and block collapse date.

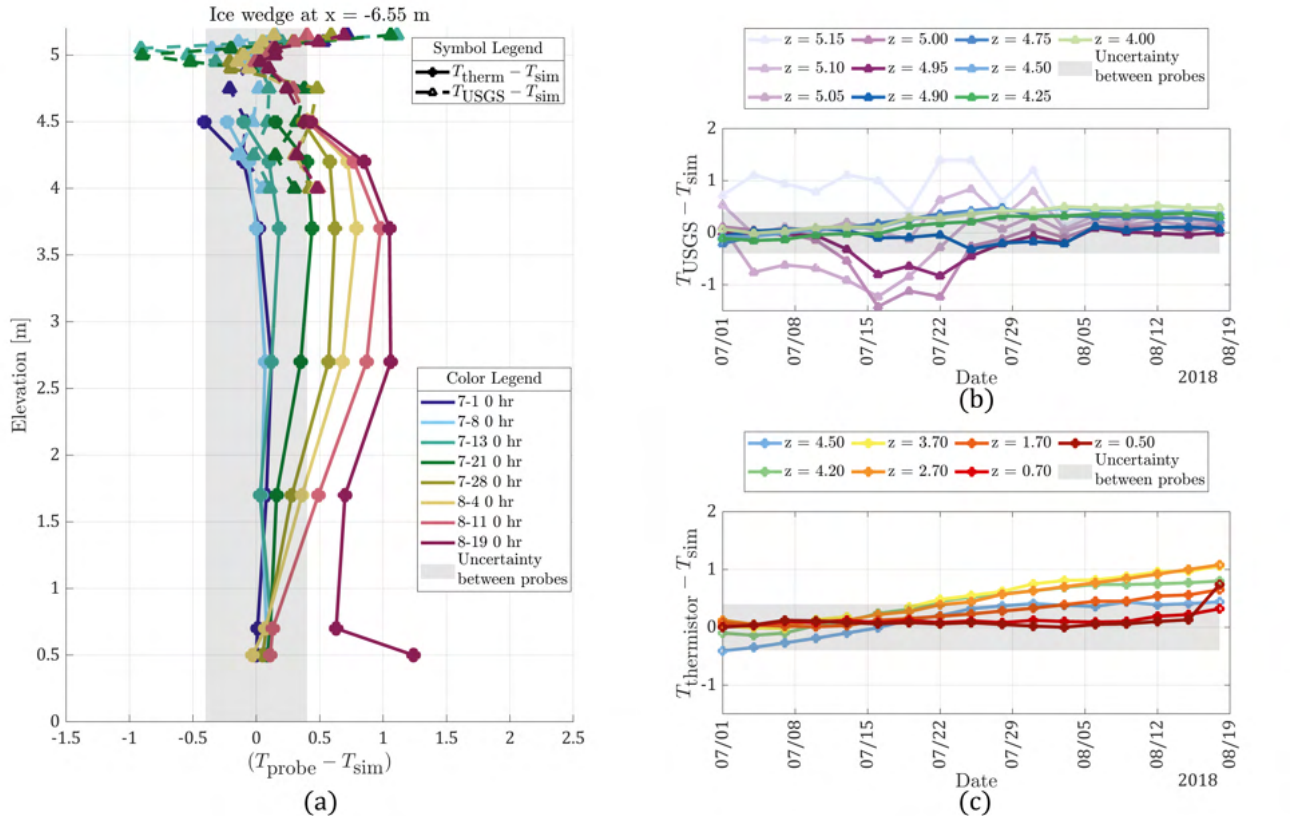

Figure S3. Comparison of temperature evolution of modeled ice wedge at $x = -6.55$ m in simulation domain with observed temperatures from USGS probe and vertical thermistor string. The difference between modeled and observed temperatures is shown: (a) varying with elevation for selected dates in color, with triangle markers denoting USGS comparison and circle markers denoting thermistor comparison, and (b-c) evolving in time for different elevations shown in color, comparing against (b) the USGS probe and (c) the vertical thermistor string. For all plots, the uncertainty between probes is established by taking the maximum difference between the thermistor string and USGS probe observations over the time period considered.

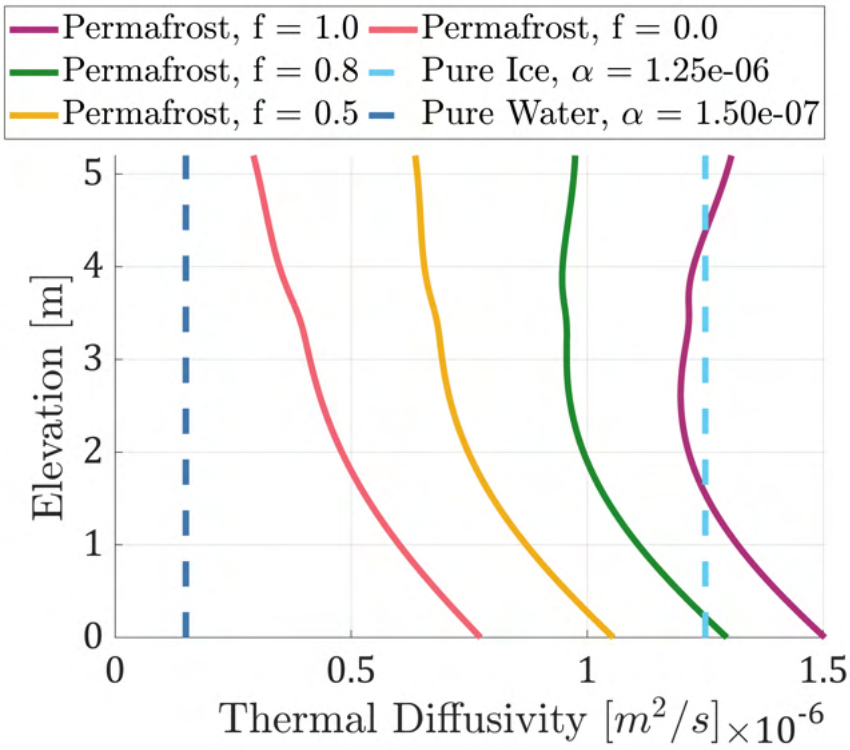

Figure S4. Thermal diffusivity with elevation of pure ice and pure water (dashed cyan and blue lines) compared with modeled ice-bonded sediment at varying ice saturation of $f = 1$(purple), $f = 0.8$ (green), $f = 0.5$ (yellow), and $f = 0.0$ (pink). For all but fully frozen ice-bonded sediment, ice is significantly more thermally diffusive.

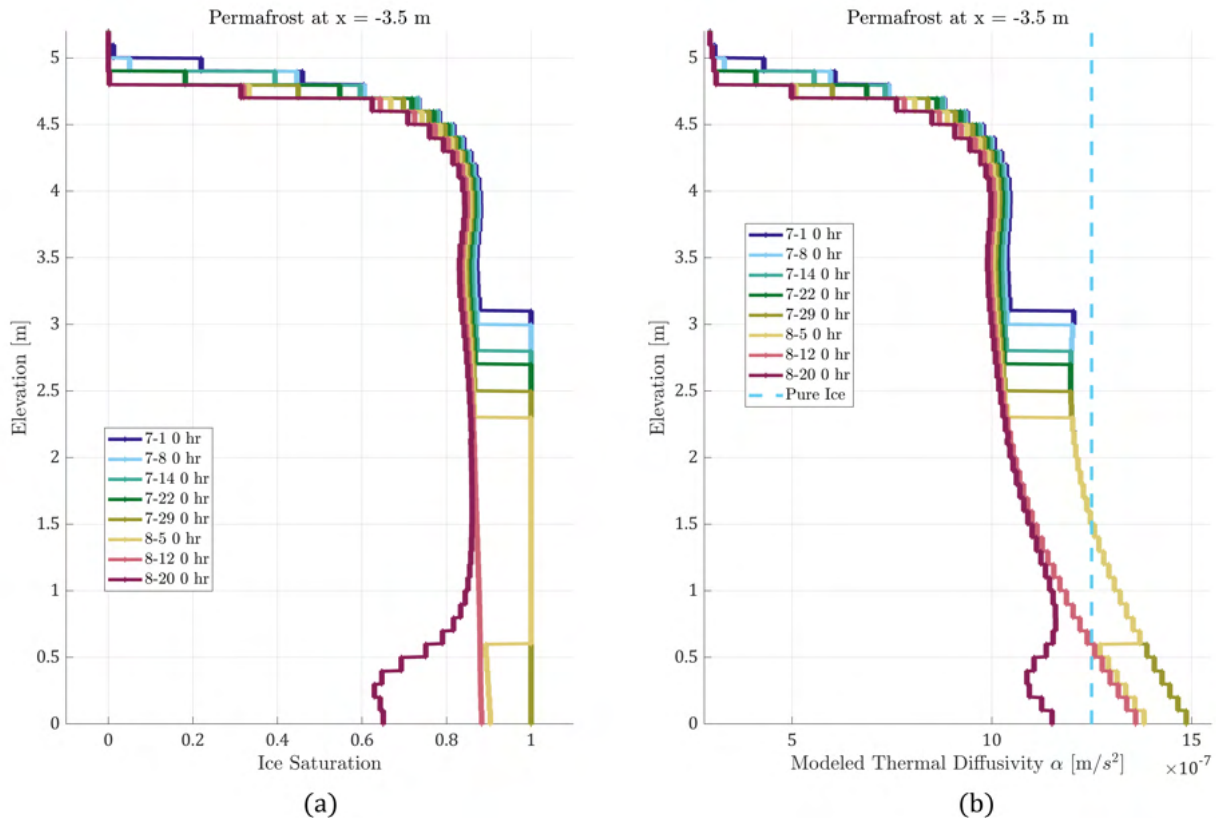

Figure S5. Simulated (a) ice saturation and (b) thermal diffusivity (α) for ice-bonded sediment at $x = -3.5$ m varying with elevation for select dates shown in color.